POWER LOSS AND HEATING IN COUPLINGS AND GEARS

A Dissertation

by

AHMAD IBRAHIM AHMAD DAWAHDEH

Submitted to the Office of Graduate and Professional Studies of
Texas A&M University
in partial fulfillment of the requirements for the degree of

DOCTOR OF PHILOSOPHY

Chair of Committee,	Alan Palazzolo
Committee Members,	Won-Jong Kim
	Dion Antao
	Hamn-Ching Chen
Head of Department,	Andreas A. Polycarpou

December 2020

Major Subject: Mechanical Engineering

ABSTRACT

Transmitting power devices are widely used in the industry. These devices like couplings and gears are used to transmit the power from the source to the load. Power loss and heating represent one of the most important problems in these devices. Simulating and predicting these problems besides finding some solutions will be very helpful for the industry in terms of the safety of the workers and money-saving.

For the coupling part, the concentration was on the coupling guard. The coupling guard is a piece of equipment that encloses the coupling to protect industrial workers from the rotating coupling. Overheating of coupling guards characterizes a major safety and machine stop problem. Coupling guards may reach a very high temperature due to the windage power loss caused by the high rotating speed of the coupling. Based on the last version of API 671, the peak temperature for the coupling guard should not exceed 60℃.

This research proposes a machine learning model and an empirical formula to predict the maximum guard temperature and power loss. Machine learning models used a database from simulated CFD cases for different coupling guards under various conditions. Also, this research provides validation for the CFD models with experimental tests for different cases. ANSYS CFX has been used to build the CFD model.

The suggested machine learning model uses eight different input parameters to predict temperature and power loss. The model shows an accurate prediction for a varied number of CFD cases. The performance of the generated model has been verified with the experimental results.

Also, an empirical formula has been created using the same database from CFD results. The results show that the ML model has a better prediction than the empirical formula for predicting the peak temperature and power loss for all cases.

For the gear part, the research covers several topics. The first topic is building a Finite Element (FE) model using the Thermo-Elastohydrodynamic Lubrication (TEHL) method to simulate the sliding power loss between the teeth of the gear. The finite element model can calculate the minimum film thickness, sliding power loss, hydrodynamic pressure between the gears teeth, and the efficiency of the gear system. This Finite element model has been validated with several published experimental cases.

The Finite element model has been used to build a training data set using ten parameters. This training data set has been utilized to train the machine learning model. This model able to predict the sliding power loss and the peak temperature of the gear tooth. Also, the training data set used to generate an empirical formula to predict the sliding power loss in addition to the peak temperature of the gear tooth.

PDE solver in MATLAB has been used to simulate the thermal stress and thermal deformation in the gears due to the uneven heating. This uneven heating occurs because of the sliding power loss between the teeth.

The results of the prediction models for both couplings and gears shows very good accuracy with $R^2 = 0.96$ and $R^2 = 0.98$ for coupling and gear machine learning models, respectively.

DEDICATION

The dissertation is dedicated to my parents first, and family including my wife, son, brothers, and sisters, who helped me and gave me the spirit, courage, curiosity, and optimism to finish my Ph.D. career.

ACKNOWLEDGEMENTS

I would like to thank Prof. Palazzolo for his help and guidance since I joined the Vibration Control and Electromechanical Laboratory of Texas A&M University. His professionalism and wisdom in solving the problems and his wide knowledge in several areas helped me a lot in my work. It was an honor to have such a professor as my advisor.

Also, I would like to thank my committee members, Dr. Kim, Dr. Antao, and Dr. Chen for their guidance and comments to improve my research.

Finally, I want to thank my mother and father for their support and motivation. I want also to thank my family especially my elder brother “Mohammad Noor” for their help. Finally, I want to thank my wife and my son for their love and support.

CONTRIBUTORS AND FUNDING SOURCES

Contributors

The work was supervised by a dissertation committee consisting of Professors Alan Palazzolo, Won-Jong Kim, and Dion Antao of the Department of Mechanical Engineering and Professor Hamn-Ching Chen of the Department of Civil and Environmental Engineering.

The experimental part of chapter 2 in section 2.2.7. done by John Crane company.

The experimental data in chapter 3 in section 3.3.6. was cited from a published paper in 2019 in Journal of the Brazilian Society of Mechanical Sciences and Engineering,

All other work conducted for the dissertation was completed by the student under the supervision of professor Palazzolo.

Funding Sources

The dissertation research was supported by the TRC (Turbomachinery Research Consortium) of Texas A&M University.

NOMENCLATURE

a	Constant to calculate fatigue life
A_i	Area of the asperities
b	Gear face width
b_0	Constant to calculate fatigue life
C	Correlation constant
cl	Radial clearance
C_p	The specific heat
C_{p0}	The reference specific heat capacity
D	The distance between surfaces
DBFF	Distance Between Flange Faces
d_i	Pitch diameter of the gear
D_{max}	Maximum coupling diameter
d_{shaft}	Diameter of the shaft
E'	Equivalent modulus of elasticity
E_1	Modulus of elasticity of the pinion
E_2	Modulus of elasticity of the gear
F	Correction factor
$F_{\frac{3}{2}}$	Statistical function
F_i	Force held by asperities

g	Gravitational acceleration
G	Modulus of rigidity
h	Thickness of lubricating film
h_i	Convection heat transfer coefficient
K	Modified Bessel function
k	Thermal conductivity
k_0	The reference thermal conductivity of the fluid
k_i	Correction factor
L	Length of the gear
m	Mean function
m_h	Factor to calculate the convection coefficient
N_{as}	Number of asperities
$N_{failure}$	Number of cycles before failure
n_g	Number of teeth of gear
NOB	Number of bolts on coupling flanges
n_p	Number of teeth of pinion
Nu	Nusselt number
OAR	Oil to air ratio
P	Power loss
p	Pressure
p_{asp}	Asperities pressure

p_{hyd}	Hydrodynamic pressure
pr	Constant to update the viscosity
Pr	Prandtl number
q_f	Heat flux transferred to the fluid
q_g	Generated energy per unit volume
q_g	Heat flux transferred to the gear
q_{gen}	Generated heat flux from sliding power loss
q_p	Heat flux transferred to the pinion
R	Equivalent radius of curvature
r	Radius of the gear or coupling
R_o	Rayleigh's output value
R_a	Average roughness
r_b	Base radius of the gear
Re	Reynolds number
$R_{g,2}$	Radius of curvature of gear
R_i	DOE input parameters
$R_{p,1}$	Radius of curvature of pinion
r_ζ	Radius of the contact point
s	Unit distance for the covariance function
S'_e	Endurance limit
s_0	Viscosity-temperature index

S_e	Corrected endurance limit
S_{ut}	Ultimate strength
T	Temperature
t	Time, Gear thickness
T_0	The reference temperature of the fluid
U	Velocity in X direction
U_b	Bending energy
U_c	Compression energy
U_p	Potential energy
u_r	Rolling velocity
u_{rg}	Rolling velocity gear
u_{rp}	Rolling velocity of pinion
U_s	Shear energy
u_s	Sliding velocity
V	Velocity in Y direction
w	Equivalent normal load at the line of contact
W_i	Weight function
Z	Viscosity-pressure index, Z axes
z_i	Asperity height

Greek letters

σ_b	Bending stress
α_c	Angle of the load
β	Asperity diameter
ζ	Auxiliary parameter
v	Coefficient of volume expansion
μ_∞	Constant to update the viscosity
$\boldsymbol{\kappa}$	Covariance function
ρ	Density
Γ	Gamma function
β	Heat flux density distribution coefficient
γ	Heat flux factor, Pressure factor
θ	Involute rotation angle
α_ρ	Lubricant dependent constant
ν	Non-negative parameter
v_2	Poisson's ratio for the gear
v_1	Poisson's ratio for the pinion
λ	Ratio of the Film thickness to the average roughness
ω	Rotating speed
τ	Shear stress
σ	Standard deviation

α_{cp}	Temperature coefficient of specific heat
ρ_0	Reference density
μ_0	Reference viscosity
μ	Viscosity of the fluid
ϵ^{th}	Thermal deformation
α	Thermal deformation coefficient
σ_{th}	Thermal stress
ε_α	Transverse contact ratio
$\boldsymbol{\phi}$	Viscous dissipation rate

TABLE OF CONTENTS

Page

LIST OF FIGURES

Page

LIST OF TABLES

Page

1. INTRODUCTION

Transmit a mechanical power from a source to a load is one of the major processes in mechanical engineering. Transmitting mechanical power could be done using coupling if the rotating velocity from the source and the load are the same. Gear could be used if the desired rotating speed different from the source. The gear is one of the most important turbomachinery equipment. Although gear mechanics considered an old classical mechanics; it is still a hot topic area. Several types of research have been done in this area until these days.

1.1 Coupling

Couplings are a mechanical device that is used to transmit power (a function of torque and speed) between the rotating shafts of the driver and driven machine, while also allowing for some misalignment between the shafts. The torque is transmitted between the hubs through a series of thin discs assembled in a pack [1, 2, 3]. Figure 1-1 shows the types of misalignment between shafts [4]. The first type is Axial misalignments where there is a small clearance between the two shafts. The other type of misalignments is radial misalignments. This type of misalignments occurs when the centers of two shafts are not in the same line but the angle between the centerlines of the shafts is zero. The final type of misalignment is angular misalignments that happened when there is an angle between the centerlines of the shafts. The coupling represents a solution for all these types of misalignments.

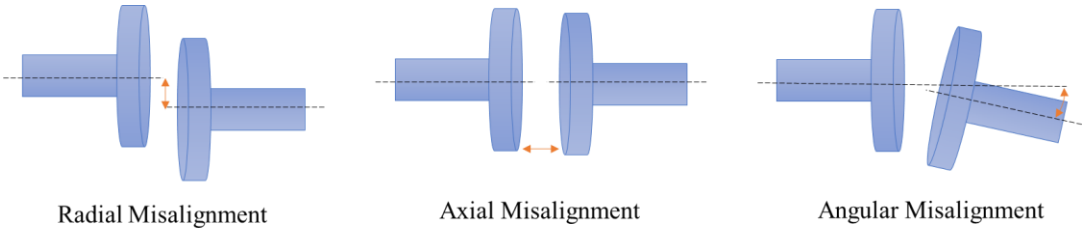

Figure 1-1 Misalignment types

There are several designs for the couplings. Each design of the couplings has a specific application. Figure 1-2 shows the most common types of couplings.

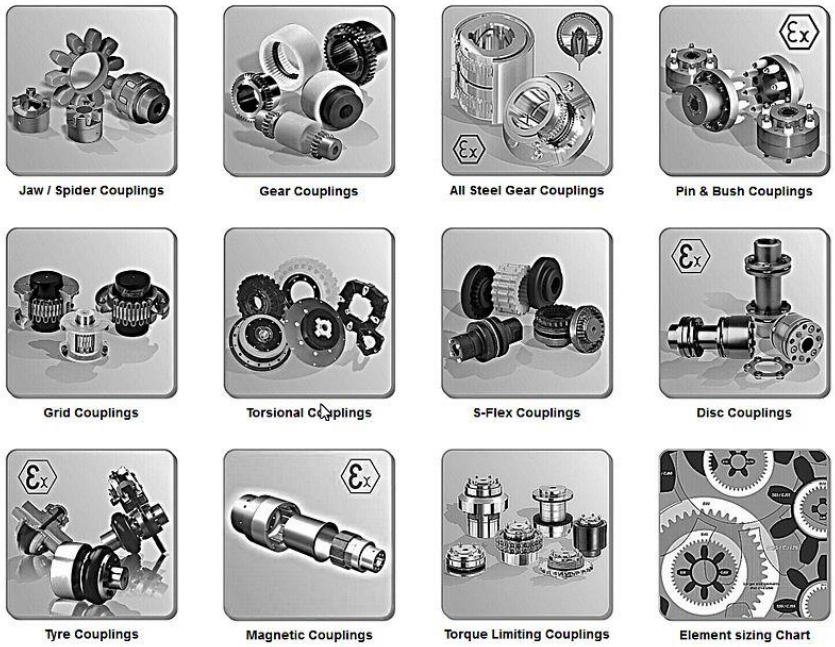

Figure 1-2 Types of couplings [2]

For safety purposes, coupling guards could be used to cover couplings. Using the coupling guard may cause some problems like oil leakage inside the guard. The leaked oil will lead to losing some power from the transmitted power by the shaft. Also, overheating

of the guard may lead to a serious injury for the workers. Figure 1-3 shows the coupling not covered and coupling covered by the guard.

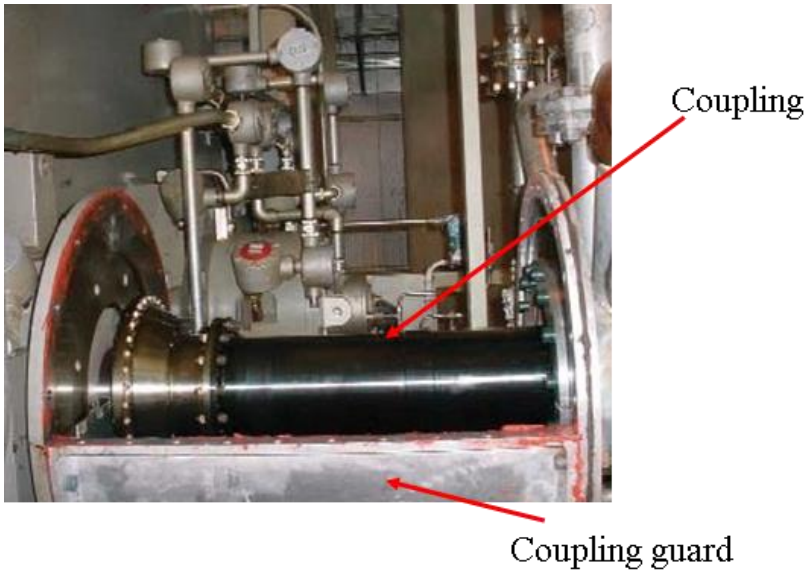

Figure 1-3 Coupling and coupling guard

To solve the oil leakage problem inside the guard, baffles can be added to the guard to collect the leaked lubricant oil [5]. Also, the baffles can be used for cooling purposes to reduce the guard temperature. The temperature and power loss distribution within coupling guards are closely associated with windage effects [6]. The forthcoming fifth edition of API 671 is expected to reduce the maximum allowable guard temperature to 140˚F (60℃) [7]. API standards specify the limit of the temperature of the coupling guard to avoid the thermal expansion in the guard, where the thermal expansion will lead to increase thermal stress in the geometries of coupling and coupling guard. The thermal stress in the geometry will reduce the life of the coupling and increase the opportunity of the coupling failure.

The investigation of coupling guard heating is therefore of practical significance for industrial application to avoid any injuries for workers and to limit the amount of power loss.

The power loss and overheating for the coupling relates to windage phenomena. Windage power loss is caused by the viscous dissipation for moving fluid and the friction between fluid particles. The major factors affecting the viscous dissipation are fluid viscosity and speed. High rotating speed increases the energy dissipation [8, 9]. This windage power loss has a major effect in rotodynamic machines like couplings and gears because it leads to losing some of the transmitted power in addition to a rise in temperature of the equipment [6, 10].

The windage in couplings has been tested by some researchers. Different studies have been done in this field. Jiang has suggested three approaches to solve the windage problem. The first approach is by adding a windage defect device (WDD). WDD is a hollow channel attached to the end of the coupling. The air enters WDD channels to reduce the coupling temperature and makes equivalent pressure. The difference between Jian's approaches is just the path of air inside the channels [11].

Research work for the effect of coupling guard design on the peak temperature of the guard has been established by M. Calistrat, who mentioned in his research the temperature of the guard can reach 350˚F [12]. M.Calistrat suggested a prediction formula for the temperature of the coupling; this formula has been built based on a limited number of experimental data. The formula can predict the temperature of the guard using some parameters like coupling temperature, ambient temperature, and other constants, which can

be calculated from the geometry of the coupling. D. Carter et al. have recommended a formula to predict the temperature of the guard. Carter's formula depends on the relation between the windage power loss and the peak temperature of the guard [13].

Very few researches done in coupling guard heating as mentioned in the introduction. The available research in the coupling field is summarized in Table 1-1. This table shows the gapes in the research in this field.

Table 1-1 Research done in the coupling guard field

Research	**Methodology**	**Available research**
Coupling guard temperature (Effect of parameters)	Experimental	Yes [2], [6]
	CFD	Yes [6]
Empirical formula prediction (Temperature)	Experimental based	Yes [2], [14]
	CFD based	No
Empirical formula prediction (Power loss)	Experimental based	Yes [14]
	CFD based	No
ML prediction (Temperature)	Experimental based	No
	CFD based	No
ML prediction (Power loss)	Experimental based	No
	CFD based	No

1.2 Gear

Power loss in gear could be classified for two types as shown in Figure 1-4. The first type is no load power loss. This type of power loss is independent of the magnitude of the input torque in the gear [15]. Windage and churning power loss are examples of no-load power loss [14], [16]. The other type of power loss is load-dependent power loss. Load dependent power loss varies depending on the input torque. Increase the input torque will increase the power loss for load-dependent power losses in gears. Sliding power loss in gear is the major load-dependent power loss in the gear system [17].

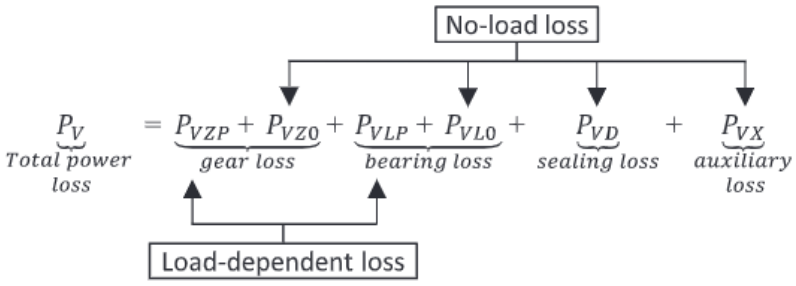

Figure 1-4 Power loss types in the gear system

2D CFD model of windage power loss for spur gear in the air has been proposed by K Al-Shibl et al. [18]. This study was limited for air without considering the effect of the oil. The result of this study shows that the profile of the gear tooth has a major influence on windage power loss. The research recommended adding fillets or chamfers at the corners of the teeth to reduce the windage effect [19].

Y.Marchesse et al. made a 3D CFD model for spur gear to simulate the effect of windage power loss in the air [20]. This research as previous on is limited to the windage effect due to air only without considering the effect of the lubricant oil. The authors found

that the 3D CFD model has a more accurate prediction for the windage power loss since it is simulating a more complex situation.

The second type of no-load power loss is churning power loss. Some papers called it spin power loss. Churning occurs due to the squeeze of the lubricant oil between the gaps of the gears. Churning power loss could be studied experimentally by rotating both gears at the same speed at the same time. This experiment has been done by Polly et al. to evaluate the churning power loss [21]. The results of the research show that the temperature of the lubricant has a significant effect on power loss, especially at the high rotating speed. The reason for the temperature effect is the change of the oil viscosity with the temperature. The increase in the oil temperature will reduce the churning power loss because the viscosity of the oil will decrease by temperature.

Load dependent power loss changes with the load on the gear. Sliding power loss considered as the major source for the load-dependent power loss. Sliding power loss happens when gears teeth contacts. Friction occurs at the contact from the shear stress in the fluid film [22]. For heavy-duty gears or low oil viscosity, the film thickness will be very thin, so a mixed lubricant should be considered for these cases [23].

It is very hard to measure the sliding power loss separately using experimental methods. Numerical and analytical methods are the most used way for this purpose. The numerical methods are using the elastohydrodynamic lubrication (EHL) analysis [23]. This analysis analyzing the contact region between the gears' teeth using the Reynolds equation. EHL method has been used to evaluate the sliding power loss by calculating the shear stress in the lubricant layer [23]. Wu et al. proposed a numerical model for power loss using the

EHL method [24]. The results of the EHL analysis show that the sliding power loss and minimum film thickness changes along the line of action. The change of the sliding power loss and film thickness is a result of the changes in the load and sliding velocity along the line of action. The EHL method has been used for different gear types like spur gear [25], bevel gear [26], and helical gear [27].

heating may bend the rotor and cause thermally induced instability (Morton effect) under cert

Recently Thermal Elastohydrodynamic Lubrication (TEHL) model has been improved for simulating sliding power loss in gears. This model is more accurate than the EHL model because it is considering the effect of oil temperature while solving the Reynolds equation. The results of this method proposed by Khonsari et al. [28]. The results of the TEHL model has a more accurate prediction because it considers the effect of temperature on the lubricant viscosity. The problem of simulating the THEL model is the challenges to program this complex model for the gear problem [29].

Mixed lubrication assumptions should be considered for very thin film thickness with high input torque. Lai et al. have used a numerical analysis for bevel gear using mixed lubricate assumption. The simulation also includes a temperature behavior for the gear tooth under mixed lubrication condition [30].

The TEHL model has been used to simulate the effect of lubricant type on the sliding power loss, friction, and minimum film thickness. The results of TEHL analysis for the effect of oil show that the properties of the oil have a major effect on the temperature of the gear [31].

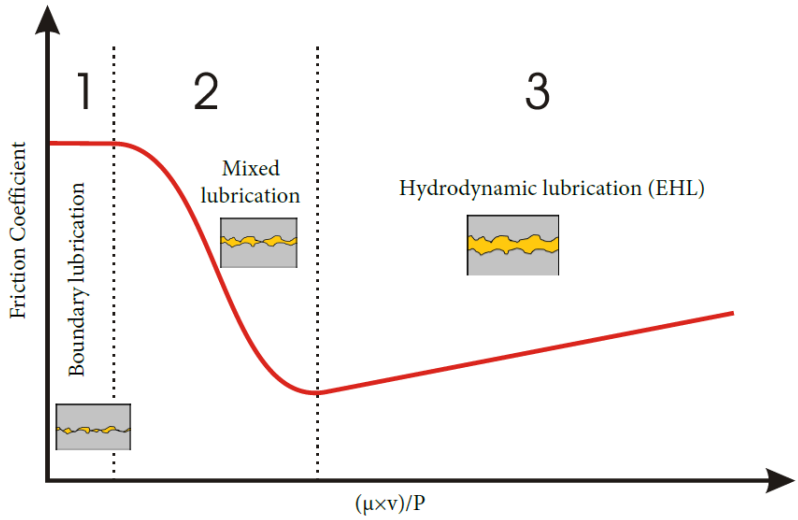

Figure 1-5 Stribeck curve

Stribeck curve Figure 1-5 shows the borders between Boundary lubrication, mixed lubrication, and hydrodynamic lubrication. The hydrodynamic lubrication model developed to be elastohydrodynamic lubrication with considering the deflection in the solid. The deflection in the solid will result in a change in the film thickness. The curve shows the friction coefficient which is the main source of the sliding power loss effected by three factors. These factors are the viscosity of the lubricant (μ), the velocity of the surface (v), and the pressure made by the surface on the fluid (P). This remarks on the importance of studying the effect of these factors to know the type of lubrication for each case of study. The effect of speed and temperature has been proposed by Lu et al. [32]. The results of the research show the friction coefficient is proportional to the velocity. This result is matching with Stribeck curve. The other finding is the friction coefficient is inversely proportional to lubricant temperature. This finding is not directly described in the curve. The source of this finding is the relation between the viscosity and temperature. The

pressure also has a direct effect on the friction coefficient in addition to an effect on viscosity.

The results of Lu's research justify the importance of considering the non-constant viscosity fluid in the simulation. The advantage of considering the non- constant viscosity fluid is studying the effect of pressure and temperature on the friction coefficient based on the effect of these two factors on the viscosity. The non-constant viscosity fluid assumption will help to choose the correct simulation model for the lubrication type based on the Stribeck curve.

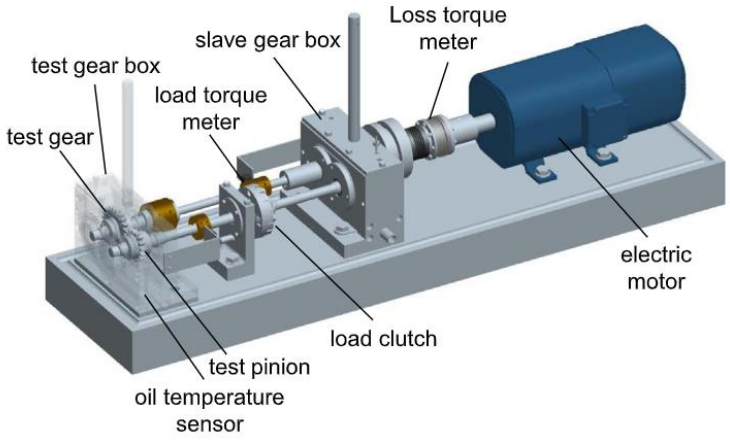

Figure 1-6 Experiment setup for measuring spur gear power loss.

Figure 1-6 shows the equipment and the set up for the experiment to measure the power loss for the gear system. This experiment could be used to measure the total loss for the gear system. In this experiment, the AC motor applies a known input torque to the shaft. The power is transmitted by the gear set. The output torque could be measured from the

split load (Usually coupling with torque meter). The difference between the input and output torque represents the power loss from the gear system.

This experiment measures the total power loss together. By using this experiment is hard to distinguish the magnitude of each kind of power loss. The difficulties of separate the experimental power loss's measurements for each kind of power loss make the simulation one of the favorite ways to predict the power loss for each type separately [33].

Based on the recent researches sliding power loss is more than 64% of the total power loss in the gear system Figure 1-7 [34].

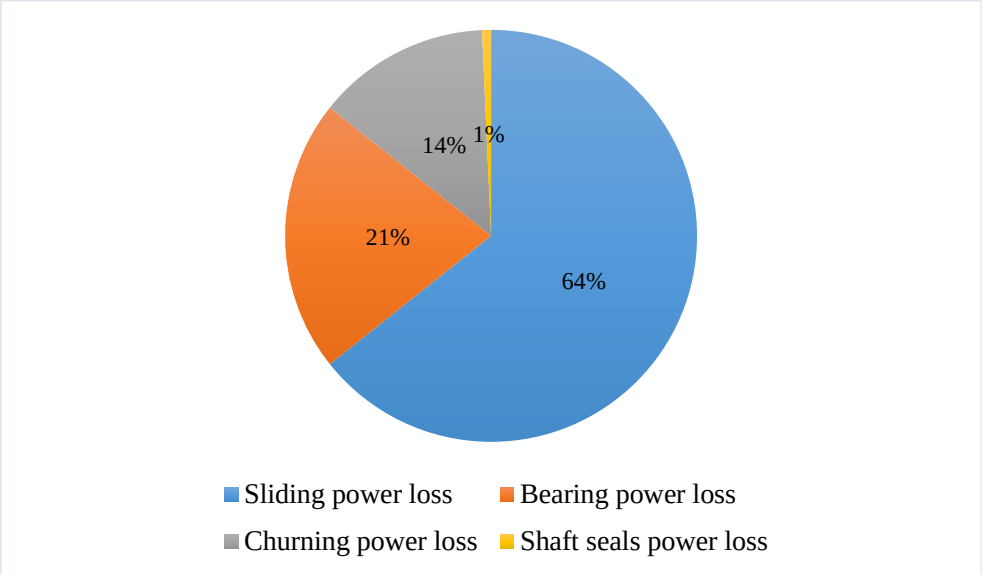

Figure 1-7 Types of power loss in gears

Gear systems could be classified based on different standards like the type of gears, tooth shape…etc. one of the most common classification methods is the contact ration in the gears. If the contact ratio is less than 2, the contact ratio system called Standard Contact Ratio (SCR). If the contact ratio between the gears is more than 2, the system named High

Contact Ratio. (HCR). The contact ratio could be specified based on the geometry of the pinion and the wheel gears. If the maximum number of teeth in contact at the same time between the pinion and the gear is 2, the contact ratio will be 2 or less. In the other case if the maximum number of teeth in contact is three the contact ratio will be more than 2. The design of the high contact ratio (HCR) is beneficial because it reduces the maximum Hertzian load on the tooth of the gear. This will elongate the lifetime of the gear [35].

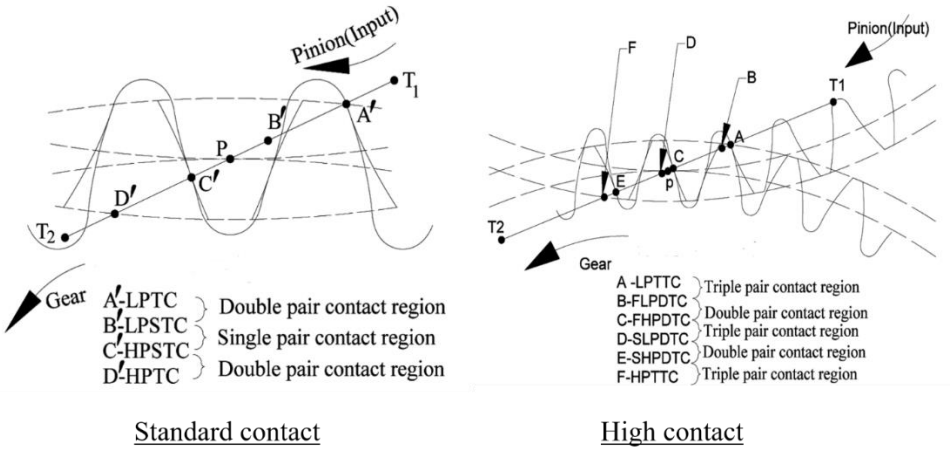

Figure 1-8 Comparison between standard contact and high contact gears

Figure 1-8 shows a comparison between the standard contact and high contact gear system. The figure also shows the number of contacted teeth along the line of action.

The research in the gears is very deep. Many publications have been published modeling and solving the problems in the gears. Finding a gap in gear research was challenging. The summery for different research that simulating the sliding power loss in addition to the thermal distribution is mentioned in Table 1-2. The table also includes some research that proposes the thermal stress and thermal deformations in the gears. The table

contains the methodologies that these authors have simulating the power loss and temperature distribution in the gears.

Table 1-2 Summary for research for sliding power loss in gears

Author	Normal force calculation	Sliding velocity calculation	Film thickness calculation	Film temperature calculation	Power loss calculation	Gear tooth temperature calculation	Friction coefficient calculation	Surface roughness	Thermal deformation	Thermal stress	Elastic deformation In tooth and gear body	Stress of Induced force in gear body	Contact type
Chang et al. [36]	----------	Gear analysis method	----------	----------	Analytical calculation for power loss	3D finite element method (using ANSYS)	Correlations for friction coefficient	----------	-------	------	----------	----------	Standard contact
Fernandes et al. [37]	----------	Gear analysis method	----------	----------	Analytical calculation for power loss	3D finite element method (using ANSYS)	Correlations for friction coefficient	----------	-------	------	----------	----------	Standard contact
Shi et al. [38]	Gear analysis method	Gear analysis method	----------	----------	Analytical calculation for power loss	3D finite element method (using ANSYS)	Assumed a constant friction factor with an assumed value	----------	-------	------	----------	----------	Standard contact
Liu et al. [39]	Gear analysis method	Gear analysis method	FEM for EHL	----------	FEM for power loss	----------	----------	----------	-------	------	Deformation at the contact point $\frac{1}{\pi}\int P(X).\ln\lvert X - X'\rvert$	----------	Standard contact

Table 1-2 (Continued) Summary for research for sliding power loss in gears

Author	Normal force calculation	Sliding velocity calculation	Film thickness calculation	Film temperature calculation	Power loss calculation	Gear tooth temperature calculation	Friction coefficient calculation	Surface roughness	Thermal deformation	Thermal stress	Elastic deformation In tooth and gear body	Stress of Induced force in gear body	Contact type
Liu et al. [40, 5]	Gear analysis method	Gear analysis method	FEM for EHL	FEM for film temperature	FEM for power loss	----------	FEM for the friction coefficient	----------	-------	------	Deformation at the contact point $\frac{1}{\pi}\int P(X).\ln\lvert X - X'\rvert$	----------	Standard contact
Liu et al. [40, 5]	Gear analysis method	Gear analysis method	FEM for EHL	FEM for film temperature	FEM for power loss	----------	FEM for the friction coefficient	----------	-------	------	Deformation at the contact point $\frac{1}{\pi}\int P(X).\ln\lvert X - X'\rvert$	----------	Standard contact
Sekar et al [41]	Gear analysis method and FEM (ANSYS)	Gear analysis method	Correlations for film thickness	----------	Analytical calculation for power loss	----------	Correlations for friction coefficient	----------	-------	------	----------	----------	Standard contact
Lohner et al [42]	Gear analysis method	Gear analysis method	FEM for EHL	FEM for film temperature (COMSOL)	FEM for power loss	FEM for film temperature (COMSOL)	FEM for the friction coefficient	----------	-------	------	Deformation at the contact point $\frac{1}{\pi}\int P(X).\ln\lvert X - X'\rvert$	----------	Standard contact

Table 1-2 (Continued) Summary for research for sliding power loss in gears

Author	Normal force calculation	Sliding velocity calculation	Film thickness calculation	Film temperature calculation	Power loss calculation	Gear tooth temperature calculation	Friction coefficient calculation	Surface roughness	Thermal deformation	Thermal stress	Elastic deformation In tooth and gear body	Stress of Induced force in gear body	Contact type
Akbarzadeh et al. [43]	Gear analysis method	Gear analysis method	Correlations for film thickness	Analytical solution for the energy equation	Analytical calculation for power loss	Analytical calculation for the temperature of tooth surface without the distribution for the temperature in the gear	Correlations for friction coefficient	Correlations for surface roughness on film thickness	-------	------	----------	----------	Standard contact
Wang et al. [44]	Gear analysis method	Gear analysis method	FEM for EHL	1D FEM for film temperature	----------	----------	FEM for the friction coefficient	----------	-------	------	Deformation at the contact point $\frac{1}{\pi}\int P(X).\ln\lvert X - X'\rvert$	----------	Standard contact
Bobach et al. [45]	Gear analysis method	Gear analysis method	FEM for EHL	FEM for film temperature	----------	----------	FEM for the friction coefficient	FEM for using surface roughness	-------	------	Deformation at the contact point $\frac{1}{\pi}\int P(X).\ln\lvert X - X'\rvert$	----------	Standard contact

Table 1-2 (Continued) Summary for research for sliding power loss in gears

Author	Normal force calculation	Sliding velocity calculation	Film thickness calculation	Film temperature calculation	Power loss calculation	Gear tooth temperature calculation	Friction coefficient calculation	Surface roughness	Thermal deformation	Thermal stress	Elastic deformation In tooth and gear body	Stress of Induced force in gear body	Contact type
Liu et al. [46]	Gear analysis method	Gear analysis method	FEM for EHL	FEM for EHL temperature	FEM for EHL	----------	FEM for the friction coefficient	----------	-------	------	Deformation at the contact point $\frac{1}{\pi}\int P(X).\ln\lvert X - X'\rvert$	----------	Standard contact
Li et al. [47]	Gear analysis method	Gear analysis method	Correlations for film thickness	----------	----------	----------	----------	----------	-------	------	----------	----------	Standard contact
Li et al. [48]	Gear analysis method	Gear analysis method	Correlations for film thickness	----------	Analytical calculation for power loss	----------	----------	----------	-------	------	----------	----------	Standard contact
Jie et al. [49]	----------	----------	----------	----------	----------	3D finite element method (using ANSYS)	Assumed a constant friction factor with an assumed value	----------	-------	------	----------	----------	Standard contact
Jie et al. [50]	Gear analysis method	Gear analysis method	----------	----------	Analytical calculation for power loss	3D finite element method	Correlations for friction coefficient	----------	-------	------	----------	----------	Standard contact

Table 1-2 (Continued) Summary for research for sliding power loss in gears

Author	Normal force calculation	Sliding velocity calculation	Film thickness calculation	Film temperature calculation	Power loss calculation	Gear tooth temperature calculation	Friction coefficient calculation	Surface roughness	Thermal deformation	Thermal stress	Elastic deformation In tooth and gear body	Stress of Induced force in gear body	Contact type
Xiang et al. [51]	Gear analysis method	Gear analysis method	----------	----------	Analytical calculation for power loss	3D finite element method (using ANSYS)	Correlations for friction coefficient	----------	-------	------	----------	----------	Standard contact
Wei et al. [52]	----------	Gear analysis method	----------	----------	Analytical calculation for power loss	3D finite element method (using ANSYS)	Assumed a constant friction factor with an assumed value	----------	-------	------	----------	----------	Standard contact
Anuradha et al. [53]	Gear analysis method	Gear analysis method	FEM for EHL	Analytical calculation for film temperature	Analytical calculation for power loss	----------	----------	----------	-------	------	Deformation at the contact point $\frac{1}{\pi}\int P(X).\ln\lvert X - X'\rvert$	----------	Standard contact
Li [54]	Gear analysis method	----------	----------	FEM for film temperature	Analytical calculation for power loss	----------	----------	Surface roughness profile	-------	------	----------	----------	Standard contact

Table 1-2 (Continued) Summary for research for sliding power loss in gears

Author	Normal force calculation	Sliding velocity calculation	Film thickness calculation	Film temperature calculation	Power loss calculation	Gear tooth temperature calculation	Friction coefficient calculation	Surface roughness	Thermal deformation	Thermal stress	Elastic deformation In tooth and gear body	Stress of Induced force in gear body	Contact type
Zhang et al. [55]	Gear analysis method	Gear analysis method	FEM for EHL	FEM for film temperature	----------	----------	FEM for the friction coefficient	Surface roughness profile	-------	------	Deformation at the contact point $\frac{1}{\pi}\int P(X).\ln\lvert X - X'\rvert$	----------	Standard contact
Mongkol et al. [56]	Gear analysis method	Gear analysis method	FEM for EHL	FEM for film temperature	----------	----------	FEM for the friction coefficient	----------	-------	------	Deformation at the contact point $\frac{1}{\pi}\int P(X).\ln\lvert X - X'\rvert$	----------	Standard contact
Luo et al. [57]	Gear analysis method	Gear analysis method	Correlations for film thickness	----------	Analytical calculation for power loss	3D finite element method (using ANSYS)	Correlations for friction coefficient	----------	-------	------	----------	----------	Standard contact
Patil et al. [58]	----------	----------	----------	----------	----------	----------	----------	----------	-------	------	----------	FEM for stress in gear body (ANSYS)	Standard contact

Table 1-2 (Continued) Summary for research for sliding power loss in gears

Author	Normal force calculation	Sliding velocity calculation	Film thickness calculation	Film temperature calculation	Power loss calculation	Gear tooth temperature calculation	Friction coefficient calculation	Surface roughness	Thermal deformation	Thermal stress	Elastic deformation In tooth and gear body	Stress of Induced force in gear body	Contact type
Budzik et al. [59]	----------	----------	----------	----------	----------	----------	----------	----------	-------	------	----------	FEM for stress in gear body (ABAQUS)	Standard contact
Wang et al. [60]	----------	----------	----------	----------	----------	----------	----------	----------	-------	------	----------	FEM for stress in gear body (C++)	Standard contact
Gupta et al. [61]	----------	----------	----------	----------	----------	----------	----------	----------	-------	------	----------	FEM for stress in gear body (ANSYS)	Standard contact
Ooi et al. [62]	----------	----------	----------	----------	----------	----------	----------	----------	-------	------	FEM for deformation in gear body (ANSYS)	FEM for stress in gear body (ANSYS)	Standard contact
Karaveer et al. [63]	----------	----------	----------	----------	----------	----------	----------	----------	-------	------	FEM for deformation in gear body (ANSYS)	FEM for stress in gear body (ANSYS)	Standard contact

Table 1-2 (Continued) Summary for research for sliding power loss in gears

Author	Normal force calculation	Sliding velocity calculation	Film thickness calculation	Film temperature calculation	Power loss calculation	Gear tooth temperature calculation	Friction coefficient calculation	Surface roughness	Thermal deformation	Thermal stress	Elastic deformation In tooth and gear body	Stress of Induced force in gear body	Contact type
Thirumurugan et al. [64]	----------	----------	Correlations for film thickness	----------	Analytical calculation for power loss	----------	Correlations for friction coefficient	----------	-------	------	----------	----------	High contact ratio
Karpat et al [65]	----------	----------	Correlations for film thickness	----------	Analytical calculation for power loss	----------	Correlations for friction coefficient	----------	-------	------	----------	----------	High contact ratio

As described in the literature, several methods have been used to calculate the power loss and the temperature in the gears. This research has a new direction to calculate the power loss and temperature of the gear. The idea of the current work builds a comprehensive code to simulate the power loss and temperature and stress for the gear tooth using the TEHL model. The simulation will be done for 2D and 3D analysis in addition to a comparison between the results for 2D and 3D models.

The unique idea of the work is studying the surface roughness and thermal deformation effect on the power loss in the gear. This study will be done for standard and high contact ratio gears. For the gear system, the film thickness between gears' teeth may become very thin (less than a micrometer). For very thin film thickness considering the surface roughness will be very important. Sometimes, the film thickness will be less than the surface roughness, so it may have a significant effect on power loss and film thickness calculation.

Mixed lubrication is called solid-liquid lubrication. This type of lubrication occurs during the contact between two surfaces. In mixed lubrication, a part of the contact will have a lubricant fluid (elastohydrodynamic). The other part of lubrication will have direct contact and interaction between asperities points. Make research for this point will be also very important for power loss and temperature simulation.

Considering the thermal deformation in the gear tooth is important also. The effect of thermal deformation may have a significant effect on film thickness. A 3D model will be used to measure the thermal deformation in the gear tooth and identify its influence on the film thickness.

The difference between this research and other publications in this field are

- Using a finite element method for all simulating sliding power loss and gear heating steps (sliding power loss, film thickness, gear deformation, tooth temperature, and film temperature). For previews publications like Khonsari et al. [63], they used some correlations to calculate the film thickness.

- Consider thermal deformation because the gear heating will be a new contribution. The previous research concentrates more on the gear temperature without considering the deformation of the gear.

- The sliding power loss will affect just on the contact surface of the tooth. The thermal stress will occur from the uneven heating for the gear tooth. Calculate the thermal stress for the gear will be an important area of research in this project. As mentioned in the previous point researchers are not considering this case in their publications.

- Generate a statistical prediction model for gear power loss and heating. By using the FEM, a large database can be simulated at a low cost.

- Produce a machine learning model to forecast the power loss and temperature of the gear.

- Analyze high contact ratio gears (Contact ratio > 2). The analysis will include normal force analysis, film thickness along the line of action, film, and gear temperature.

- Compare the peak temperature, the total power loss, the thermal stress, and thermal the deformation between standard contact ratio and high contact ratio systems.

- Make study for the lifetime (Fatigue life) for standard contact and high contact gear systems.

- Compare the lifetime between standard and high contact gear systems.

The significance of this research is making a prediction model and high accuracy FEM for simulation. RSM DOE will be chosen to make a training data set for generating a prediction model. Statistical analysis could be applied to generate a prediction model. Statistics will be the first choice to generate a formula using the training data set. Some users may prefer formula shape for prediction because it is easy to use. On the other hand, using advanced techniques like machine learning is very important. The machine learning model could be used for the prediction and optimization of the design. In this project, both techniques will be used for predictions. The project will include a comparison of the performance for each prediction method.

Reducing the power loss and heating is one of the priorities in the industry. The high-efficiency model may be achieved by testing different designs under different operation conditions. A high accuracy simulation model could be used by industrial workers to predict the performance of new designs under different conditions. The model also may be used to make optimization for the current designs.

2. COUPLINGS

2.1. Introduction

Simulating the power loss and heating in couplings will save a lot of many and effort. The idea of this research is to exploit the advantage of advanced CFD software to generate a large training data set. The generated database will be used to create a high accuracy prediction method for the peak temperature of the guard and power loss for the coupling. This research proposes a validated CFD model with experimental data to predict the peak temperature of the coupling guard. A large database has been collected from CFD simulation using Box-Behnken and the full factorial design of experiments. The collected data was used as a training dataset to generate a machine learning model for predicting the temperature of the guard and the power loss in the coupling. Also, an empirical formula using Rayleigh's method with high accuracy has been formulated to compare the performance for the two methods for predicting the coupling guard's temperature and coupling's power loss.

This research proposes how to use ANSYS CFX to simulate this problem. The rotating reference frame method has been used to include the effect of the bolts on the power loss. This research also includes some solutions for heating in the coupling guard. The first solution was using the Mailbox shape and the second solution was adding some ventilation ports to the guard. All the results will be presented later in this chapter.

2.2. Methodology

2.2.1. Mathematical model

Fluid problems are described by momentum, continuity, and energy equations. The proposed problem can be defined by the mentioned fluid equations. The methodology of this problem defines the fluid motion and energy for the interaction between the high-speed rotating coupling and trapped air between the coupling and the guard. The high speed of rotating coupling may reach more than 10000 rpm. The high speed for the coupling with the large diameter will lead to a considerable viscous dissipation of heating and windage power loss. Eq. 2-1 is the general continuity equation in the cylindrical coordinate. The continuity equation is applied for each element in the trapped air [16].

$$\frac{1}{r}\frac{\partial(ru_r)}{\partial r}+\frac{1}{r}\frac{\partial u_\theta}{\partial \theta}+\frac{\partial u_z}{\partial z}=0 \qquad \textbf{Eq. 2-1}$$

In this equation r, θ and z are the cylindrical coordinates of the system. The velocity for each coordinate has been presented by u.

Eq. 2-2, Eq. 2-3, and Eq. 2-4 show the general 3-D steady-state Navier-Stokes equations in the cylindrical coordinates that describe the conservation of momentum in the trapped air [16]. Navier-Stokes equations have been described in Eq. 2-2, Eq. 2-3, and for r, θ, and z coordinates respectively.

Navier-Stokes equations for r axes

$$\rho\left(u_r\frac{\partial u_r}{\partial r}+\frac{u_\theta}{r}\frac{\partial u_r}{\partial \theta}+u_z\frac{\partial u_r}{\partial z}-\frac{u_\theta^2}{r}\right)=\rho g_r-\frac{\partial p}{\partial r}+\mu\left[\frac{1}{r}\frac{\partial}{\partial r}\left(r\frac{\partial u_r}{\partial r}\right)+\right. \qquad \textbf{Eq. 2-2}$$

$$\left.\frac{1}{r^2}\frac{\partial^2 u_r}{\partial \theta^2}+\frac{\partial^2 u_r}{\partial z^2}-\frac{2}{r^2}\frac{\partial u_\theta}{\partial \theta}-\frac{u_r}{r^2}\right]$$

Navier-Stokes equations for θ axes

$$\rho\left(u_r\frac{\partial u_\theta}{\partial r}+\frac{u_\theta}{r}\frac{\partial u_\theta}{\partial \theta}+u_z\frac{\partial u_\theta}{\partial z}-\frac{u_r u_\theta}{r}\right)=\rho g_\theta-\frac{1}{r}\frac{\partial p}{\partial \theta}+ \quad \textbf{Eq. 2-3}$$

$$\mu\left[\frac{1}{r}\frac{\partial}{\partial r}\left(r\frac{\partial u_\theta}{\partial r}\right)+\frac{1}{r^2}\frac{\partial^2 u_\theta}{\partial \theta^2}+\frac{\partial^2 u_\theta}{\partial z^2}+\frac{2}{r^2}\frac{\partial u_r}{\partial \theta}-\frac{u_\theta}{r^2}\right]$$

Navier-Stokes equations for z axes

$$\rho\left(u_r\frac{\partial u_z}{\partial r}+\frac{u_\theta}{r}\frac{\partial u_z}{\partial \theta}+u_z\frac{\partial u_z}{\partial z}\right)=\rho g_z-\frac{\partial p}{\partial z}+\mu\left[\frac{1}{r}\frac{\partial}{\partial r}\left(r\frac{\partial u_z}{\partial r}\right)+\right. \quad \textbf{Eq. 2-4}$$

$$\left.\frac{1}{r^2}\frac{\partial^2 u_z}{\partial \theta^2}+\frac{\partial^2 u_z}{\partial z^2}\right]$$

In Eq. 2-2, Eq. 2-3, and Eq. 2-4 ρ is the fluid density, g_r is the gravitational acceleration in the radial direction, p is the pressure of the fluid, and μ is the fluid viscosity [16].

Since the problem describes the trapped air inside the guard, the energy equation should be satisfied with each element in the model. Eq. 2-5 shows the general steady-state energy equation for the cylindrical coordinates [16].

$$u_r\frac{\partial T}{\partial r}+\frac{u_\theta}{r}\frac{\partial T}{\partial \theta}+u_z\frac{\partial T}{\partial z}=\frac{q_g}{cp}+\alpha\left[\frac{1}{r}\frac{\partial}{\partial r}\left(r\frac{\partial T}{\partial r}\right)+\frac{1}{r^2}\frac{\partial^2 T}{\partial \theta^2}+\frac{\partial^2 T}{\partial z^2}\right]+\frac{\phi}{\rho c_p} \quad \textbf{Eq. 2-5}$$

where T is the temperature, q_g the generated energy per unit volume, c_p the specific heat of the air, α thermal diffusivity of the air, and ϕ is the viscous dissipation rate.

Viscous dissipation rate ϕ is an important term in this work since it is the main source of heat in the trapped air when the coupling is rotating at a very high speed. Eq. 2-6 shows the value of $\phi(Mun)$.

$$\phi = 2\mu\left[\left(\frac{\partial u_r}{\partial r}\right)^2 + \left(\frac{1}{r}\frac{\partial u_\theta}{\partial \theta} + \frac{u_r}{r}\right)^2 + \left(\frac{\partial u_z}{\partial z}\right)^2\right] + \mu\left[\left(\frac{1}{r}\frac{\partial u_r}{\partial \theta} + \frac{\partial u_\theta}{\partial r} - \frac{u_\theta}{r}\right)^2 + \left(\frac{\partial u_\theta}{\partial z} + \frac{1}{r}\frac{\partial u_z}{\partial \theta}\right)^2 + \left(\frac{\partial u_z}{\partial r} + \frac{\partial u_r}{\partial z}\right)^2\right] \quad \textbf{Eq. 2-6}$$

2.2.2. Finite element model and coupling geometry

Figure 2-1 (a) shows the coupling geometry used in the CFD tests. The tested coupling geometry is similar to the coupling used in the experimental part. The tested coupling geometry has many bolts as labeled in Figure 2-1 (a). The bolts will affect the turbulence and the viscous dissipation amount for the air. The multiple reference frame approach has been utilized based on the advantages of this model for simulating roto-dynamics machines with fluid-solid interaction [66]. In this model the simulation modeler can consider the effect of bolts on the trapped air inside the guard; also, this approach will reduce the computation time with high accuracy [67].

Figure 2-1 (b) represents the half-section for the coupling geometry. The half section has been used in the simulation with periodic boundary conditions in the section sides. The purpose of using periodic boundary conditions is the symmetrical shape of the coupling. Using half-section geometry in the simulation for symmetrical shapes helps to reduce both the number of elements and nodes in the generated mesh and computation time for the simulation.

Figure 2-1 (c) shows the projection of the half-section. The projection demonstrates the location of the used thermocouples to measure the temperature in both the experiment and the simulation. The validation section later will compare the measurements of the

temperature from the experiment and simulation for these thermocouples. These locations of thermocouples are called hotspots. Hotspot locations have the largest change in temperature.

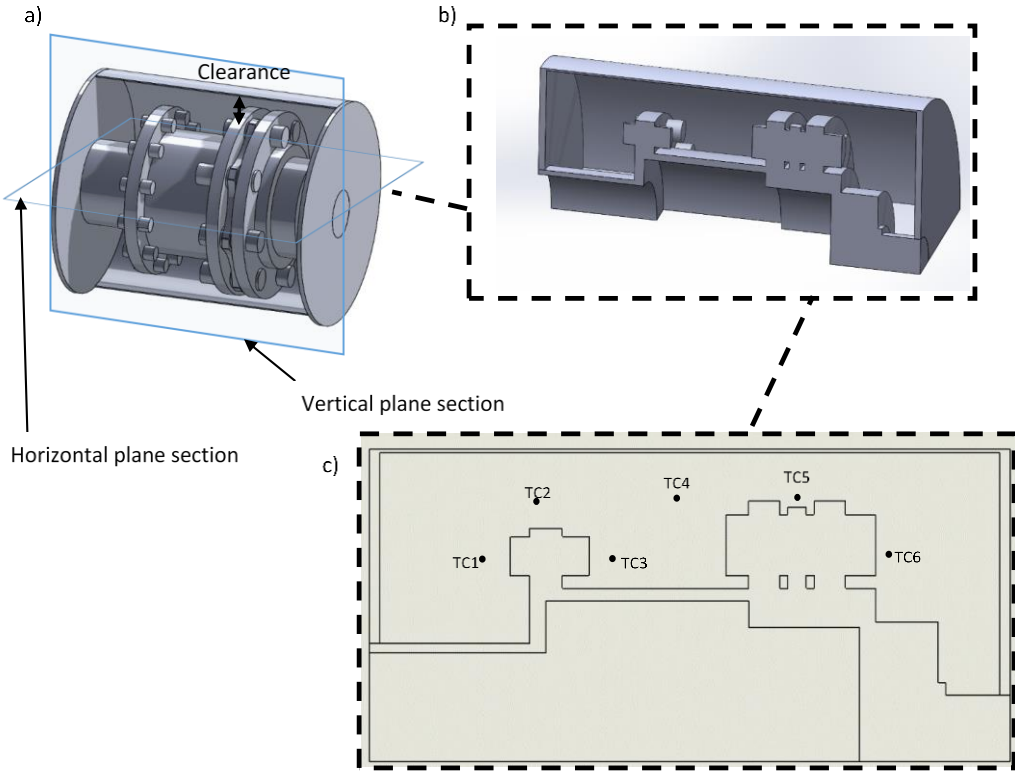

Figure 2-1 Coupling geometry a) Full size coupling geometry b) Quarter section for coupling and coupling guard c) Thermocouples locations

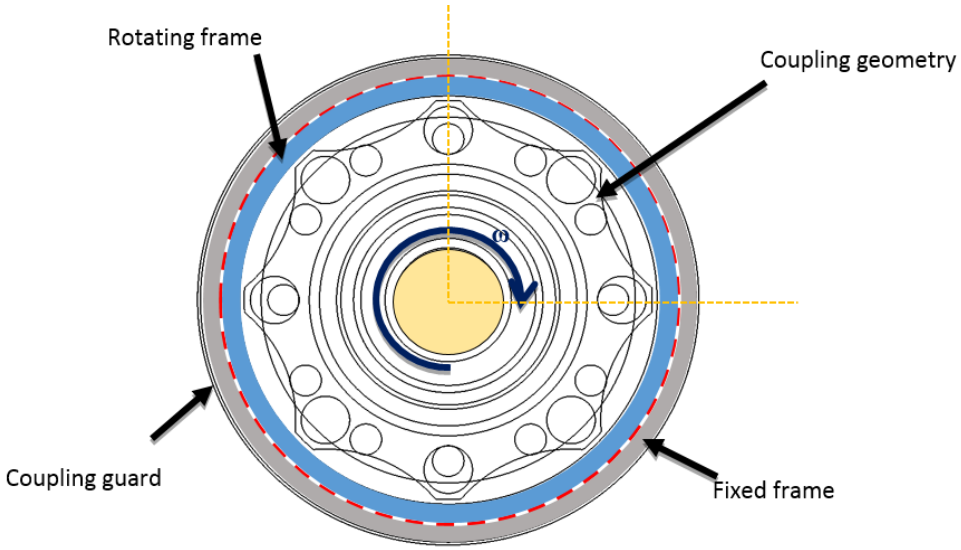

Figure 2-2 Rotating reference from model

Figure 2-2 displays a cross-section for the model with the assigned boundary conditions for the multiple reference frame.

2.2.3. Mesh of simulation

Different cases have been done for the coupling under several variant conditions. The coupling has been studied for three sizes of guards, small, medium and large guards with 20 mm, 40 mm, and 60 mm clearance respectively. These couplings have been tested at 7500 rpm. The medium guard model has been simulated for different rotating speeds (7200, 7000 and 4000 rpm). All the cases have been tested experimentally.

The mesh has been generated based on the geometries, where the model has been separated for four geometries. Fist on is the guard geometry in the orange color. The blue color is the mesh for the trapped air between the guard and the coupling. The mesh of the

geometry of the coupling and the inner fluid inside the coupling are represented by gray and green color respectively.

The surfaces of the interface between the fluid and the solid meshed carefully, where these regions must have very fin and small elements to achieve the accuracy in the simulation Figure 2-3. The accuracy can be checked by getting the necessary value and achieving the convergence in the simulation.

2.2.4. Simulation boundary conditions

A multiple reference frame method has been used to consider the effect of bolts and the complicated geometry of the coupling on the viscous dissipation. Figure 2-2 is a multiple reference frame for the model. The simulated model is the quarter of coupling geometry to reduce the time of the simulation as shown in Figure 2-1 (b). Periodic boundary conditions have been used at the cutting region (orange dashed lines). The coupling has been assigned to rotate with specific rotating speed, which characterizes the actual rotating of the coupling. The blue region of air has been assigned also to rotate by the same velocity of the coupling. The gray area is the stationary frame, which is an area region that has a zero velocity. The dashed line between the blue and gray areas is fluid to fluid interaction boundary conditions.

The fluid-solid interaction boundary condition has been imposed on two surfaces. The first one is the contacted surface between the air (blue region) and the coupling. The second location is the contacted surface between the air (gray region) and the guard.

To solve the energy equations the system must have thermal boundary conditions. The thermal boundary conditions are a constant shaft temperature of the coupling (The yellow circle) in Figure 2-2 Natural convection has been applied on all outer surfaces of the guard.

The heat transfer coefficient for the natural conviction calculated by Eq. 2-7 [6].

$$\bar{h} = 1.39(T_s - T_\infty)^{0.333} \quad \textbf{Eq. 2-7}$$

The radiation effect was also included in the simulation. The radiation was between the coupling and the guard and between the guard and the ambient. The radiation heat transfer coefficient was calculated by Eq. 2-8.

$$h_{rad} = \varepsilon\sigma[(T_s^2 + T_{surr}^2)(T_s + T_{surr})] \quad \textbf{Eq. 2-8}$$

Both the natural convection and the radiation coefficients are updated at each step based on the new average temperature of the guard (T_s).

2.2.5. Simulation solving

The simulated model for the quarter of geometry has more than 2.5M elements. ANSYS CFX 18. 0 has been utilized to solve the numerical model for Navier-Stokes and energy equations. The selection of the turbulence model in the simulation depends on the type of problem and the value of the Reynolds number.

The Reynolds number for the rotating cylinder is

$$Re = \frac{\rho\omega b^2}{\mu} \quad \textbf{Eq. 2-9}$$

where ρ is the density of the fluid, ω is the rotating speed, b is the radius of the cylinder, and μ is the viscosity of the fluid.

At 7200 rpm the value of the Re number is 1.8×10^7 at the outer diameter of the flange. But, at the shaft the value of the Re number is 2.2×10^6.

Shear stress transport turbulent model k-ω model with activation for energy solver with viscous dissipation has been selected. The k-ω model has been used for different problems due to its advantage in the roto-dynamics model with fluid-solid interaction problems [66]. The solver has been assigned to make 10000 iterations to reach the convergence.

The simulation was performed on 20 cores of TAMU Supercomputer. The computational time for each case was about 34 hours. Each time y^+ has been checked to achieve accurate results in non-isothermal fluid-solid interaction models [68]. In all simulated cases the value of y^+ was less than 80. While the value of $y^+ < 200$ this will be sufficient for good accuracy.

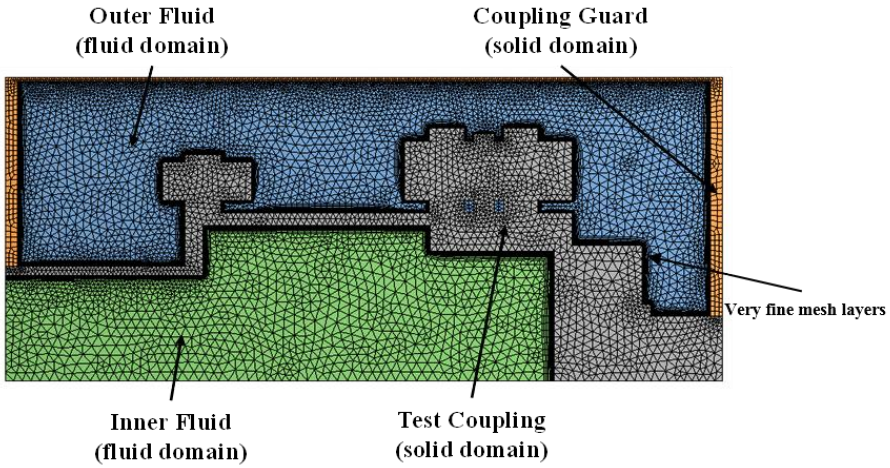

Figure 2-3 Mesh for the CFD model

2.2.5.1. $k-\omega$ model

The compact form of the $k-\omega$ model in the cartesian coordinate is shown below.

$$\frac{\partial k}{\partial t}+\frac{\partial u_j k}{\partial x_j}=\tau_{ij}^{*}\frac{\partial u_i}{\partial x_j}-\beta^{*}k\omega+\frac{\partial}{\partial x_j}\left[(v+\sigma_k v_t)\frac{\partial k}{\partial x_j}\right] \quad \textbf{Eq. 2-10}$$

$$\frac{\partial \omega}{\partial t}+\frac{\partial u_j \omega}{\partial x_j}=\hat{\gamma}_1\frac{\omega}{k}\tau_{ij}^{*}\frac{\partial u_i}{\partial x_j}-\beta_1\omega^2+\frac{\partial}{\partial x_j}\left[(v+\sigma_\omega v_t)\frac{\partial \omega}{\partial x_j}\right] \quad \textbf{Eq. 2-11}$$

The values of the coefficients of the model are

$$\beta_1=\frac{3}{40},\quad \beta^{*}=\frac{9}{100},\quad \sigma_{k1}=\frac{1}{2},\quad \sigma_{\omega 1}=\frac{1}{2},\qquad \hat{\gamma}_1=\frac{\beta_1}{\beta^{*}}-\sigma_{\omega 1}\frac{\kappa^2}{\sqrt{\beta^{*}}},\quad \kappa=0.41$$

The relations for the parameters in the model are

$$\epsilon=\beta^{*}k\omega,\qquad l=\frac{k^{1/2}}{\omega},\qquad v_t=\frac{k}{\omega}$$

The described problem in the research should use the cylindrical form for the equations of the $k-\omega$ model. The equations should be in a vector form to transfer them to the cylindrical coordinates.

$$\frac{\partial k}{\partial t} + \nabla.(Wk) = \left[v_t(\nabla W + \nabla W^T) - \frac{2}{3}kI\right] : \nabla W - \beta^* k\omega + \quad \textbf{Eq. 2-12}$$

$$\nabla.[(v + \sigma_k v_t)\nabla k]$$

$$\frac{\partial \omega}{\partial t} + \nabla.(W\omega) = \left[\gamma_1 \frac{\omega}{k}\left[v_t(\nabla W + \nabla W^T) - \frac{2}{3}kI\right]\right] : \nabla W - \beta_1 \omega^2 + \quad \textbf{Eq. 2-13}$$

$$\nabla.[(v + \sigma_\omega v_t)\nabla \omega]$$

$$\nabla W = \begin{bmatrix} \frac{\partial w_r}{\partial r} & \frac{1}{r}\left(\frac{\partial w_r}{\partial \theta} - w_\theta\right) & \frac{\partial w_r}{\partial z} \\ \frac{\partial w_\theta}{\partial r} & \frac{1}{r}\left(\frac{\partial w_\theta}{\partial \theta} - w_r\right) & \frac{\partial w_\theta}{\partial z} \\ \frac{\partial w_z}{\partial r} & \frac{1}{r}\frac{\partial w_z}{\partial \theta} & \frac{\partial w_z}{\partial z} \end{bmatrix} \quad \textbf{Eq. 2-14}$$

Using the strain and stress tensors the vector form of the equation will be

$$\tau_{ij}^* = 2v_t\bar{S}_{ij} - \frac{2}{3}k\delta_{ij} = v_t(\nabla W + \nabla W^T) - \frac{2}{3}kI =$$

$$\begin{bmatrix} 2\frac{\partial w_r}{\partial r} - \frac{2}{3}\omega & \frac{1}{r}\left(\frac{\partial w_r}{\partial \theta} - w_\theta\right) & \frac{\partial w_r}{\partial z} + \frac{\partial w_z}{\partial r} \\ \frac{1}{r}\left(\frac{\partial w_r}{\partial \theta} - w_\theta\right) + \frac{\partial w_\theta}{\partial r} & \frac{2}{r}\left(\frac{\partial w_\theta}{\partial \theta} + w_r\right) - \frac{2}{3}\omega & \frac{\partial w_\theta}{\partial z} + \frac{1}{r}\frac{\partial w_z}{\partial \theta} \\ \frac{\partial w_z}{\partial r} + \frac{\partial w_z}{\partial r} & \frac{\partial w_\theta}{\partial z} + \frac{1}{r}\frac{\partial w_z}{\partial \theta} & 2\frac{\partial w_z}{\partial z} - \frac{2}{3}\omega \end{bmatrix} \quad \textbf{Eq. 2-15}$$

The applied convection terms in the vector form of the equation are

$$\nabla.(Wk) = \frac{\partial(w_r k)}{\partial r} + \frac{w_r k}{r} + \frac{1}{r}\frac{\partial(w_\theta k)}{\partial \theta} + \frac{\partial(w_z k)}{\partial z} \quad \textbf{Eq. 2-16}$$

$$\nabla.(W\omega) = \frac{\partial(w_r \omega)}{\partial r} + \frac{w_r \omega}{r} + \frac{1}{r}\frac{\partial(w_\theta \omega)}{\partial \theta} + \frac{\partial(w_z \omega)}{\partial z} \quad \textbf{Eq. 2-17}$$

The final form of the gradient of k and ω are

$$\nabla k = \frac{\partial k}{\partial r}\hat{e}_r + \frac{1}{2}\frac{\partial k}{\partial \theta}\hat{e}_\theta + \frac{\partial k}{\partial z}\hat{e}_z \quad \textbf{Eq. 2-18}$$

$$\nabla \omega = \frac{\partial \omega}{\partial r}\hat{e}_r + \frac{1}{2}\frac{\partial \omega}{\partial \theta}\hat{e}_\theta + \frac{\partial \omega}{\partial z}\hat{e}_z \quad \textbf{Eq. 2-19}$$

The $k - \omega$ model in the cylindrical coordinate will be as shown below

Turbulence specific kinetic energy

$$\frac{\partial k}{\partial t}+\frac{\partial(w_r k)}{\partial r}+\frac{w_r k}{r}+\frac{1}{r}\frac{\partial(w_\theta k)}{\partial \theta}+\frac{\partial(w_z k)}{\partial z}=P_k-\beta^* k\omega+\frac{\partial \tau_{kr}}{\partial r}+\frac{\tau_{kr}}{r}+\frac{1}{r}\frac{\partial \tau_{k\theta}}{\partial \theta}+\frac{\partial \tau_{kz}}{\partial z} \quad \textbf{Eq. 2-20}$$

Turbulence specific dissipation rate

$$\frac{\partial \omega}{\partial t}+\frac{\partial(w_r \omega)}{\partial r}+\frac{w_r \omega}{r}+\frac{1}{r}\frac{\partial(w_\theta \omega)}{\partial \theta}+\frac{\partial(w_z \omega)}{\partial z}=\gamma_1 P_\omega-\beta\omega^2+\frac{\partial \tau_{\omega r}}{\partial r}+\frac{\tau_{\omega r}}{r}+\frac{1}{r}\frac{\partial \tau_{\omega\theta}}{\partial \theta}+\frac{\partial \tau_{\omega z}}{\partial z} \quad \textbf{Eq. 2-21}$$

where the turbulence production terms are

$$P_\omega=\frac{\omega}{k}P_k \quad \textbf{Eq. 2-22}$$

$$P_k=v_t\left\{2\left[\left(\frac{\partial w_r}{\partial r}\right)^2+\left(\frac{1}{r}\left(\frac{\partial w_\theta}{\partial \theta}+w_r\right)\right)^2+\left(\frac{\partial w_z}{\partial z}\right)^2\right]+\left(\frac{\partial w_\theta}{\partial r}-\frac{w_\theta}{r}+\frac{1}{r}\frac{\partial w_r}{\partial \theta}\right)^2+\left(\frac{\partial w_r}{\partial z}+\frac{\partial w_z}{\partial r}\right)^2\right\} \quad \textbf{Eq. 2-23}$$

and diffusion turbulence terms are

$$\tau_{kr}=(v+\sigma_k v_t)\frac{\partial k}{\partial r} \quad \textbf{Eq. 2-24}$$

$$\tau_{k\theta}=\frac{1}{r}(v+\sigma_k v_t)\frac{\partial k}{\partial \theta} \quad \textbf{Eq. 2-25}$$

$$\tau_{kz}=(v+\sigma_k v_t)\frac{\partial k}{\partial z} \quad \textbf{Eq. 2-26}$$

$$\tau_{\omega r}=(v+\sigma_\omega v_t)\frac{\partial \omega}{\partial r} \quad \textbf{Eq. 2-27}$$

$$\tau_{\omega\theta}=\frac{1}{r}(v+\sigma_\omega v_t)\frac{\partial \omega}{\partial \theta} \quad \textbf{Eq. 2-28}$$

$$\tau_{\omega z}=(v+\sigma_\omega v_t)\frac{\partial \omega}{\partial z} \quad \textbf{Eq. 2-29}$$

2.2.6. Input parameters

Table 2-1 Dimensions and operating parameters for CFD simulation

Guard and coupling geometry and operation conditions		
Dimension or parameter	Value	Unit
Distance between flanges	20.2	cm
Rotating speed	7000	rpm
Maximum diameter	43	cm
Guard clearance	4	cm
Shaft temperature	50	℃
Ambient temperature	27	℃
Surrounding temperature	27	℃
Guard thickness	0.7	cm
Solid material properties		
Property	Value	Unit
Material	Steel	----------
Specific heat	0.502	$J/kg \cdot K$
Density	7850	kg/m^3
Thermal conductivity	15	$W/m \cdot K$
Air properties at the reference temperature		
Property	Value	Unit
Material	Air	----------
Viscosity	1.849×10^{-5}	$kg/m \cdot s$
Specific heat	1007	$J/kg \cdot K$
Density	1.184	kg/m^3
Thermal conductivity	0.02551	$W/m \cdot K$

The purpose of this section is to validate the modeling approach by benchmarking it with experimental results. Once validated, the next section demonstrates the effects of varying parameter values and features on lowering coupling guard peak temperature and power loss. The dimensions, parameters, and operating conditions for the CFD simulation are tabulated in Table 2-1.

ANSYS CFX has a database for the properties. The properties are automatically updated based on the updated results during the simulation. The input data for the fluid was at the reference temperature (25℃) and pressure (1 atm).

The simulation was assigned to stop by solver controller when it achieves residual of 1×10^{-5} for the momentum and energy equation. During the simulation, the minimum achieved residual was 0.2×10^{-3} for the momentum equation and 7×10^{-6} for the energy equation.

2.2.7. Simulation results

Figure 2-4 is the temperature contours for the second test. The black arrows represent the air movement inside the coupling guard. The region close to the large bolts has a relatively higher temperature than the region near the small bolts, the difference in temperature mainly because the speed of the air near the large bolt region has a higher velocity than small bolts. The difference in speeds leads to a difference in the viscous dissipation phenomena. This effect is modeled by the viscous dissipation equation, in which the speed of the air is the main parameter. The natural convection on the guard is the reason behind the low temperature near the guard surface.

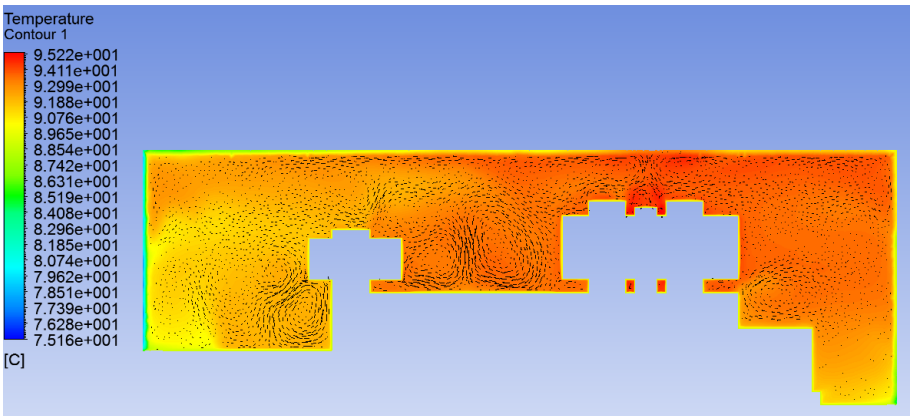

Figure 2-4 Temperature contours of the trapped air inside the guard

Figure 2-5 displays the viscous dissipation energy for the same test. The viscous dissipation is higher near the fluid at the coupling surface because it has the highest speed comparing to the other regions. The viscous dissipation is quadratic proportional to the fluid speed as modeled by the general energy equation. Near the bolts, the air will have the same velocity as the bolts, where this leads to a large dissipated heat in this region.

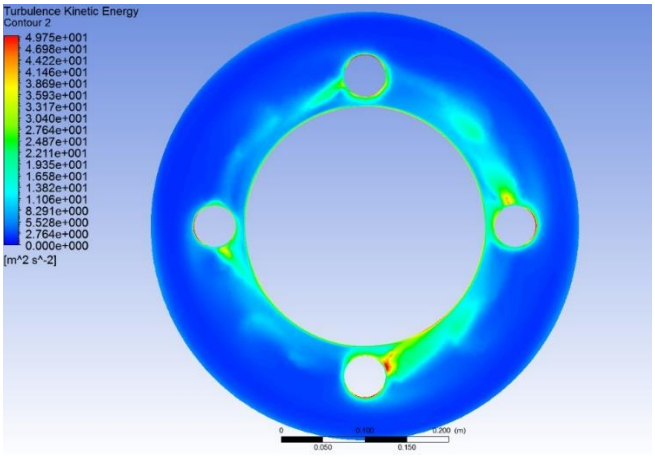

Figure 2-5 Viscous dissipation energy due to coupling rotation

2.2.7.1. Effect of mesh size

The accuracy of the simulation solution depends on the orthogonality quality of the mesh. Reduce the size of the elements in the mesh can produce the necessary improvement in the orthogonality. However, this will increase the number of elements in the model and increase the computational time. Table 2-2 shows 4 cases to study the effect of the number of elements in the model on the orthogonality quality, value of Y^+, peak temperature, and the computational time to make 10000 iterations. The results show that increasing the number of elements will increase the orthogonality quality and reduce the value of Y^+ to get more accurate results. The difference in temperature results was minor where the maximum difference in temperature did not go above 0.5%. At the same time, the results of the power loss show some variability. Excluding the coarsest mesh, the power loss values were all within 8.7%. The third mesh in Table 2-2 was used to simulate the validation cases, and to build the training dataset of the prediction models.

Table 2-2 The effect of mesh size on the convergence of the CFD results

Test number	Number of elements	Min. orthogonality quality	Number of elements with min. orthogonality	Max. Y^+	Peak temperature [^oC]	Power loss [W]	Number of iterations	Supercomputer used cores	Computational time
1	151972	0.266	264	739.4	97.6	2436.4	10000	20	11 hr. 9 min.
2	512157	0.289	9	275.6	95.8	1734.6	10000	20	14 hr. 54 min.
3	2534494	0.366	568	78.6	94.9	1653.1	10000	20	32 hr. 36 min.
4	4654852	0.541	1230	37.13	94.6	1634.6	10000	20	52 hr. 41 min.
5	11993642	0.578	1390	2.024	94.1	1595.8	10000	20	139 h. 43 min.

2.2.8. Experimental validation

In the experiment, a coupling geometry has been used for validating the simulation results. Figure 2-8 shows the geometry of the tested coupling. This experiment has been done by John Crane Inc. This coupling has a diameter of 43 cm with a maximum rotating speed of 7500 rpm. The guard has been removed for view purposes.

The tests have been separated into two groups. The first group of tests aims to determine the effect of the clearance between the coupling and the guard on the thermocouples reading. The goal of the second group of tests is to investigate the effect of rotating speed on the reading of thermocouples for the same guard size. Table **2-3** shows the tests that have been done for this coupling. Thermocouples have been installed at the location as described in Figure 2-1 (c). This coupling has been tested for about 8 hours for each case. The tests were run until a steady-state in temperature was achieved. The steady-state occurs when the temperature change was for more than an hour of operation.

Table 2-3 Experimental tests

Test group	Test number	Guard clearance [mm]	Rotating speed [rpm]
1	1	20	7000
	2	40	7000
	3	60	7000
2	4	40	4000
	5	40	7000
	6	40	7500

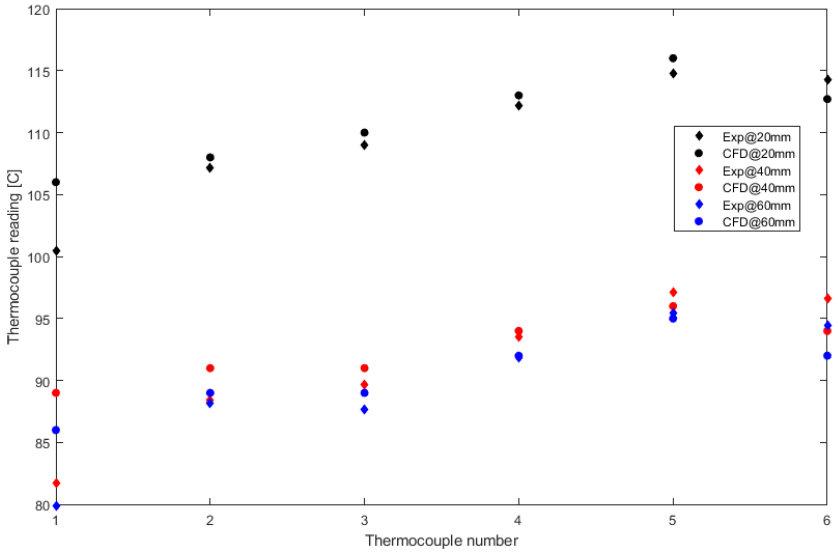

Figure 2-6 Comparison between experimental and CFD results for different guard sizes

Figure 2-6 shows the validation results for the first group of tests to evaluate the effect of the guard clearance on the temperature of the trapped air at 7000 rpm. The results show that every time the clearance between the guard and the coupling increases the reading of the thermocouples for temperature decreases. The reason for the decrease in temperature is the change of trapped air mass inside the coupling. The mass of the trapped air increases with the same amount of energy produced from the viscous. The increase in trapped air mass leads to a decrease in the air temperature as described in the general energy equation as described in Eq. 5.

For the first three cases of validation, Figure 2-7 shows a good agreement between the experiment and CFD results for all guard sizes. The largest error between the experimental and CFD results was 5.5% at thermocouple 1 for 20mm clearance.

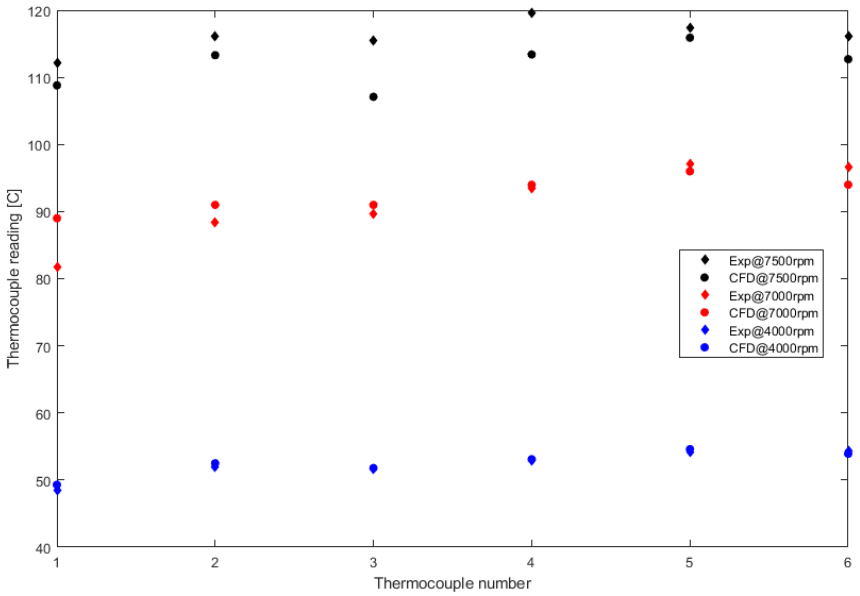

Figure 2-7 Comparison between experimental and CFD results for different rotating speed

The second group of test results shows the effect of the rotating speed of the coupling for a 40 mm guard. For the second group of tests, the rotating speed has the main effect on the amount of heat generated from the viscous dissipation of the trapped air as shown in Eq.5 and Eq.6. Figure 2-7shows how the read temperature from the thermocouples increases while the speed increases. At 7500 rpm, the reading of the thermocouples has the highest temperature for all locations. The lowest reading for the thermocouples occurred at 4000. Also, the figure shows a comparison between CFD values and the experimental values. The best accuracy achieved at 4000 rpm. At 4000 rpm the maximum error was 1.7% for all readings.

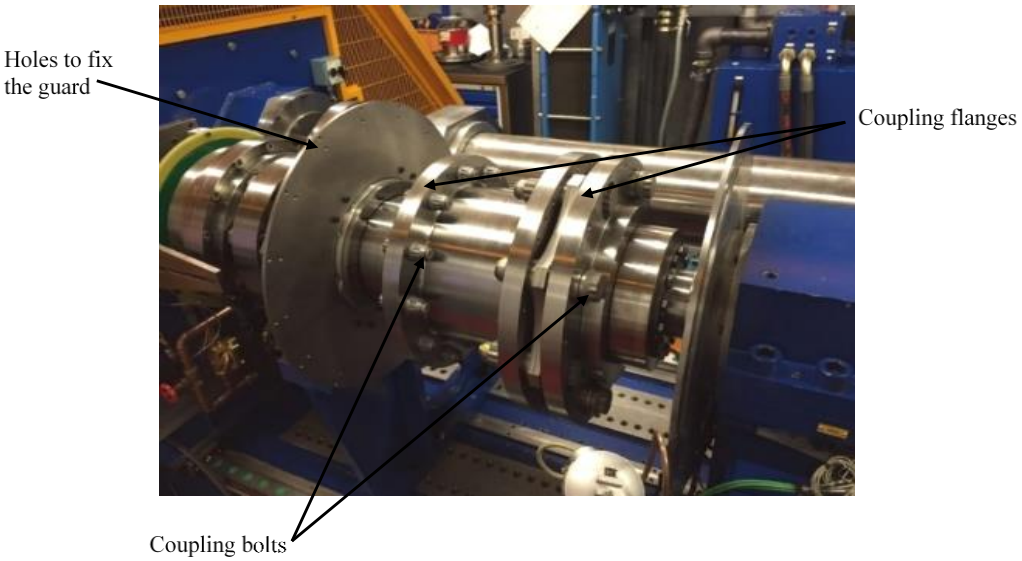

Figure 2-8 Coupling test rig (Done by John Crane Inc.)

2.2.9. The effect of different parameters

Several parameters may affect the peak temperature of the guard for the same coupling geometry, for this purpose several conditions have been tested to evaluate the effect of these parameters.

2.2.9.1. Guard shape

The first test was evaluating the effect of the guard shape on the peak temperature of the guard. Two conventional shapes have been tested first one is the cylindrical guard and the other is the mailbox guard. Figure 2-9 (a) and (b) show the effect of the guard shape for similar coupling geometry. Mailbox guard has a lower temperature than cylindrical guard at all speeds Figure 2-10. The reason for the lower temperature for the mailbox guard is a larger amount of trapped air for the same heat generation amount from viscous

dissipation. Larger guards with similar coupling designs will have a lower temperature because the larger guard contains a larger amount of trapped air mass. Based on the first law of thermodynamics as the mass increases the temperature decreases if the heat source is the same.

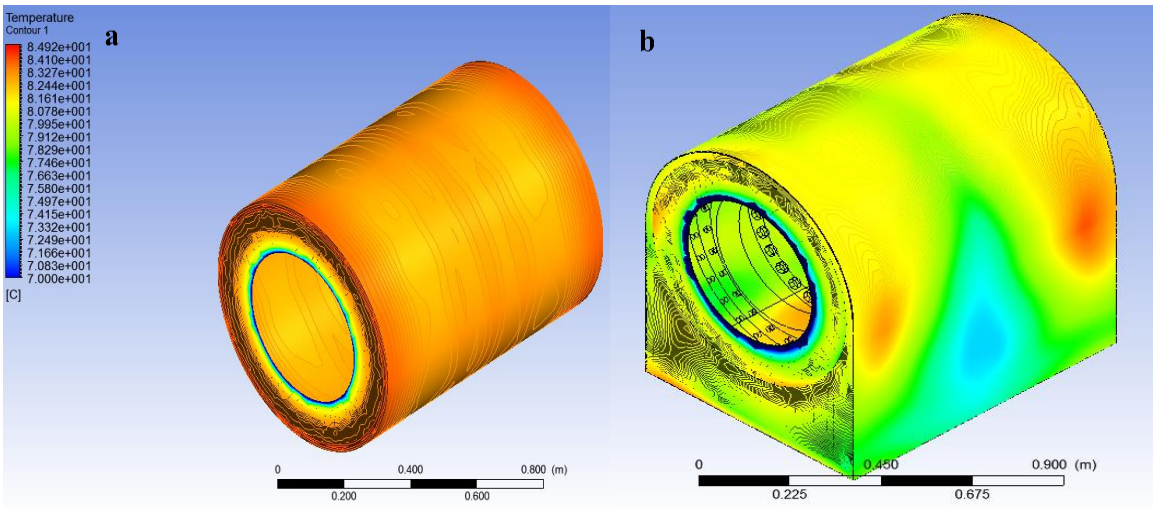

Figure 2-9 a) Temperature contours of the cylindrical guard b) Temperature contours of the mailbox guard

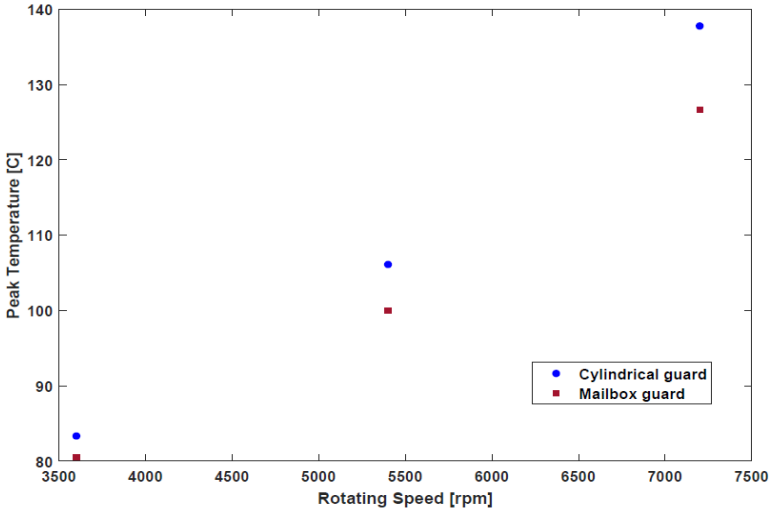

Figure 2-10 The effect of guard's shape on the peak temperature of the guard

2.2.9.2. Guard emissivity

Radiation heat transfer has a significant impact in cases with the high-temperature difference between objects. So, radiation may play a strong role in the coupling guard's temperature if the difference in temperature between the coupling and the guard is high. Four different emissivities at three different speeds have been simulated to evaluate the effect of emissivity on the peak temperature of the guard. Figure 2-11 shows the results of four identical geometries with different emissivity at each speed. The tests have been simulated at 3600, 5400 and 7200 rpm. The figure shows the emissivity of the guard has a minor effect on the peak temperature of the guard but increasing the emissivity of the guard has a minor increase in the peak temperature of the guard.

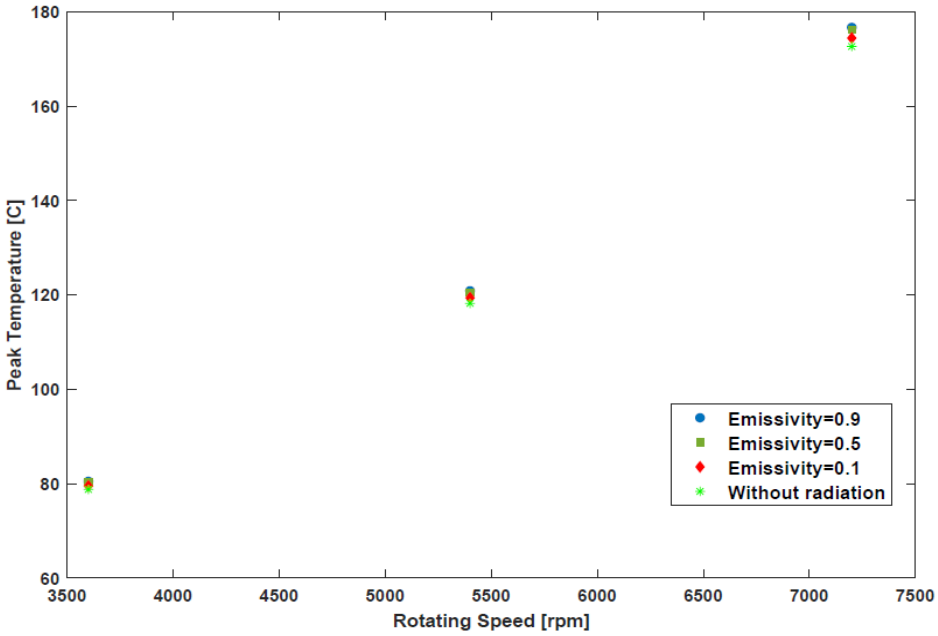

Figure 2-11 The effect of guard's material emissivity on the guard's peak temperature

2.2.9.3. Oil to air ratio

One of the conventional problems in rotodynamic machines is the leaking of the lubricant oil [69]. Sometimes a leak of the lubricant oil will enter the coupling guard. The leaked oil will change the properties of the trapped air in the guard. The change of the air properties like viscosity, density, thermal conductivity, and the specific heat will influence the solution of the equations.

The influence of the leaking oil on the peak temperature is shown in Figure 2-12. The validated models of the small, medium, and large guards have been used to evaluate the leaking effect. The figure shows an increase in the guard peak temperature while the oil to air ratio increases. This behavior caused a change in the value of air properties. Based on the effective medium theory for mixture properties the amount of leaked oil controls the amount of change in the air properties [70]. The formulas to calculate the effective

viscosity, thermal conductivity, density, and specific heat are listed in 9, 10, 11, and 12 respectively.

Effective viscosity

$$\mu_{eff} = \mu_f + 2.5\phi\mu_f \quad \textbf{Eq. 2-30}$$

where μ_{eff} is the effective viscosity for the medium of the air with oil, μ_f is the viscosity of the air, and ϕ is the oil to air ratio.

Effective thermal conductivity

$$\frac{k_{eff}}{k_f} = \frac{(1-\phi)(k_p+2k_f)+3\phi k_p}{(1-\phi)(k_p+2k_f)+3\phi k_p} \quad \textbf{Eq. 2-31}$$

In Eq. 10, k_{eff} is the effective thermal conductivity for the medium of the air with oil, k_f is the thermal conductivity of the air, and k_p is the thermal conductivity of the oil. In the effective density equation (Eq.11), ρ_{eff} represents the effective density, ρ_p is the density of the oil, and ρ_f is the density of the air

Effective density

$$\rho_{eff} = \phi\rho_p + (1-\phi)\rho_f \quad \textbf{Eq. 2-32}$$

Eq. 12 has been used to calculate the effective specific heat. Where cp_{eff}, cp_p, and cp_f are the effective specific heat, the specific heat of the oil, and the specific heat of the air respectively.

Effective specific heat

$$cp_{eff} = \phi cp_p + (1-\phi)cp_f \qquad \textbf{Eq. 2-33}$$

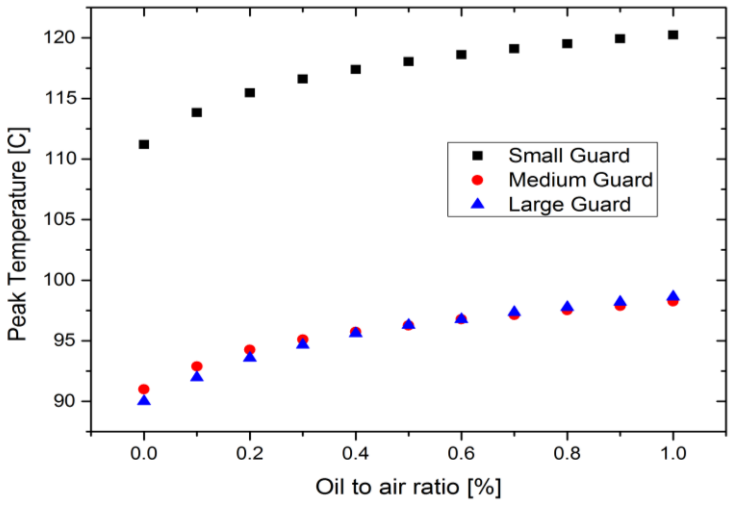

Figure 2-12 The effect of oil to air ratio inside the guard on the guard's peak temperature

The results show that increasing oil to air ratio will increase the peak temperature of the guard. This phenomenon can be justified by studying the effect of oil to air ratio on the magnitude of the Prandtl number (Pr), where the Pr number represents the ratio between the momentum diffusivity to the thermal diffusivity.

$$Pr = \frac{Momentum\ diffusivity}{Thermal\ diffusivity} = \frac{v}{\alpha} = \frac{\mu c_p}{k} \qquad \textbf{Eq. 2-34}$$

Figure 2-13 shows an increase in the Pr number with increasing the oil to air ratio at different temperatures; this means that the ratio of the momentum diffusivity to the thermal diffusivity increases when the oil to air ratio increases.

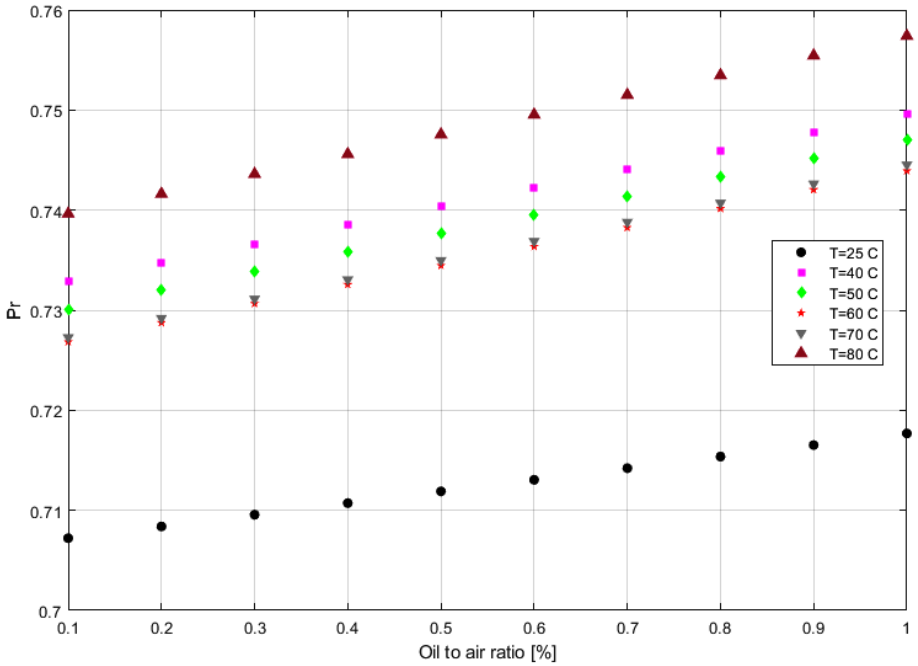

Figure 2-13 The effect of oil to air ratio on the *Pr* number

2.2.9.4. Coupling guard ventilation

Finding a solution for the high guard temperature and reducing the effect of oil leakage should be considered [71]. M. Calistrat recommends adding ventilation pipes with a baffle. The purpose of this baffle is to make a pressure difference at the inlet pipes [13]. Pressure difference at the inlet pipes will allow for air circulation from the inlet to the exit without external sources to drive the air Figure 2-14. The second reason for adding the baffle is to capture the leaking oil inside the guard.

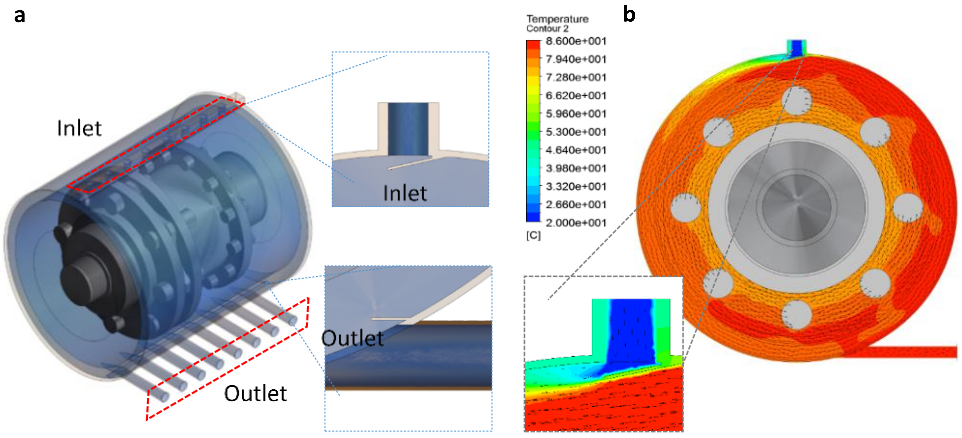

Figure 2-14 a) Coupling guard with ports b) Temperature contours for air inside the guard

The effect of the number of inlet and outlet ports and the port diameter have been tested as shown in Table 2-4. The results in Table 2-4 show that as the number of inlet or outlet ports increases this will reduce the peak temperature of the guard due to the increase in mass flow rate inside the guard. The diameter of the ports is important since an increase in the diameter corresponds with an increase in the mass flow inside the guard, and this will reduce the peak temperature of the guard.

2.2.9.5. The airflow direction in the ports

For the ports of the coupling guard, the boundary conditions were assigned as opening at all ports. The flow direction of the air depends only on the direction of rotation. The upper ports will be the inlets and the down ports are the exit if the coupling rotates counterclockwise. On the other hand, the down ports will be the inlets and the upper ports

will be the exit if the coupling rotates clockwise. Figure 2-15 and Figure 2-16 are the temperature contours for coupling rotates at 7200 rpm clockwise and counterclockwise respectively.

Table 2-4 The effect of the number of ports and size on the guard's peak temperature

Inlets	Outlets	Pipe Diameter [cm]	mass flow [kg/s]	Peak temperature [^{o}C]
1	1	3.81	0.044	67.1
3	3	3.81	0.169	58.24
5	5	3.81	0.257	54.18
7	7	3.81	0.361	54.06
9	9	3.81	0.446	48.50
5	3	3.81	0.199	54.12
7	3	3.81	0.199	56.73
7	5	3.81	0.285	53.54
9	3	3.81	0.208	56.18
9	5	3.81	0.285	53.36
9	7	3.81	0.396	50.13
5	5	2.54	0.123	62.58
5	5	5.08	0.425	48.50

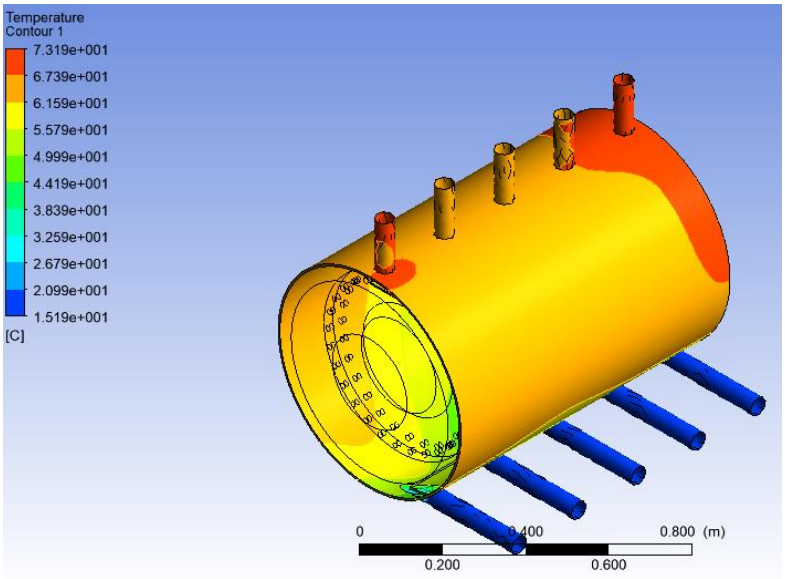

Figure 2-15 Temperature contours for the coupling guard with ports while the coupling rotates clockwise

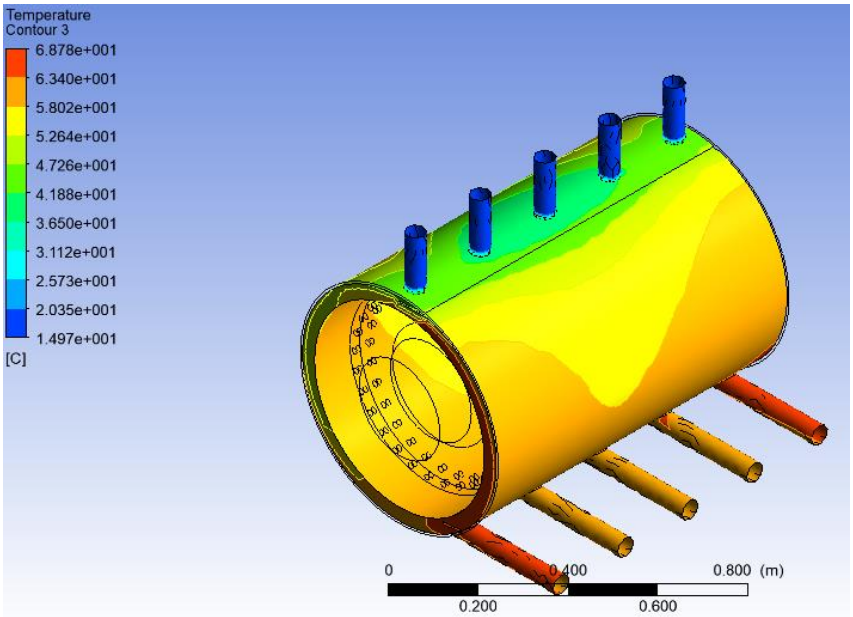

Figure 2-16 Temperature contours for the coupling guard with ports while the coupling rotates counterclockwise

The figures show that the temperature of the guards affected by the direction of the airflow direction. The peak temperature was 73.2℃ if the air enters from the lower ports. On the other hand, the peak temperature of the guard was 68.8℃ if the air enters from the upper ports. Figure 2-17 shows the effect of the airflow direction on the peak temperature of the guard. The figure shows the guard has the air that enters from the lower ports has a higher peak temperature than the guard with air that enters from the higher ports.

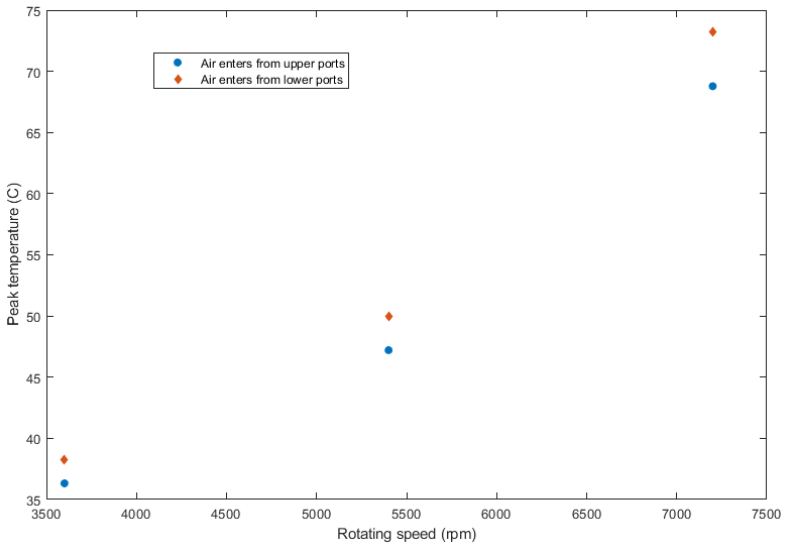

Figure 2-17 The effect of airflow direction in the guard's port on the peak temperature of the couplings

2.2.10. Prediction model

A prediction model has been built after validating the simulation model with the experimental results. The prediction model will be able to predict the peak temperature of the guard in addition to the power loss caused by the windage effect. The power loss was calculated by multiplying the drag torque by the angular rotating speed as described in the equation below.

$$Power\ loss = T_{drag} \times \omega$$ **Eq. 2-35**

The most important step is selecting the effective parameters on the peak temperature of the guard. The parameters have been chosen based on the coupling geometry, the thermal operating conditions, and the properties of the trapped air in the guard.

2.2.10.1. Prediction parameters

Figure 2-18 shows the geometry for diaphragm coupling. Diaphragm coupling geometry was used to build the prediction model. For the temperature model the, input parameters are as follows:

1) Rotating speed (RPM): 3600 – 7200rpm

The initial simulation shows that the speed of rotation has a profound influence on heat generation within the enclosure. This effect intensifies quadratically as the speed of rotation increases. This is because with a larger velocity gradient, friction will increase, and it is a major source of heat generation.

2) Maximum coupling diameter (Dmax): 18 – 24 inches (45.7-60.9 cm)

The maximum coupling diameter is regarded as a characteristic parameter of the coupling. The highest surface speed on the coupling occurs at the maximum diameter. This is where the highest temperature on the coupling is expected, making it an important parameter linked to heat generation.

3) Distance Between Flange Faces (DBFF): 20 -30 inch (50.8 -76.2 cm)

DBFF is another characteristic parameter of the coupling, which determines the relative location of the flanges within the enclosure. This value has the potential to alter air circulation within the enclosure and therefore can affect the guard temperature.

4) Radial clearance (Cl): 1-2 inch (2.54 -5.08 cm)

The radial clearance between the maximum diameter of the coupling and the inner surface of the enclosures is required to be at least 1 inch (25.4mm). The clearance influences on the Windage inside the coupling guard. The windage is a significant source of generating the heat inside the coupling guard. The most common values for the clearance are between 1 and 2 inches (25.4mm and 50.8mm).

5) Shaft temperature (Tsh): 100 – 160˚F (37-71˚C)

The heat transfer through the shaft is an important path to dissipate heat and therefore will affect the enclosure temperature. Calistart suggested that shaft temperature can be estimated using the temperature of bearing oil.

6) Ambient temperature (Tab): 60-100˚F (15 – 37˚C)

The ambient temperature will affect the natural heat transfer coefficient on the guard. It is dependent on whether the facility is indoor or outdoor, and therefore an estimated range of ambient temperatures are given.

7) Number of bolts on coupling flanges (NOB): 12-36

The bolt heads are evenly distributed across the flange. As the heads of the bolts rotate in the trapped air, they will churn the air, which will cause friction, one of the major sources of heat generation.

8) Oil to air ratio (OAR): 0-10×10-3

Leak oil inside the guard will affect the properties of the trapped air like viscosity, density, thermal conductivity, and the specific heat. Including this parameter is important because these properties have a significant effect on the generated heat as shown in the above study.

But for the power model, the results show there is no effect for the shaft temperature and ambient temperature on the windage power loss. For the power model, the input parameters are (Rotating speed, Maximum coupling diameter, Distance between flanges, Radial clearance, Number of bolts, and Oil to air ratio).

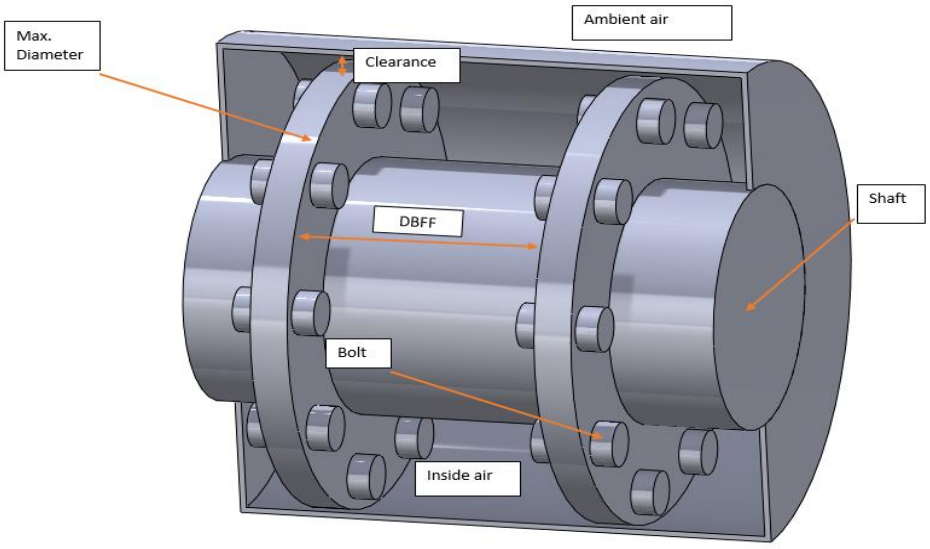

Figure 2-18 DOE diaphragm coupling geometry

2.2.10.2. Design of experiment (DOE)

A design of experiment (DOE) method has been utilized to make the tests needed to generate the prediction model. The Box-Behnken design, one of the Response Surface Methodology (RSM), was used in creating the design of experiment [72]. In this method, each parameter must have at minimum three levels, and the difference between all levels must be the same. This method used if the experiments have a physics behind it. The advantage of this method is reducing the number of needed tests with acceptable accuracy in most cases [73].

Based on the Box-Behnken experimental Design, 113 tests are needed for eight parameters. Using Box-Behnken Design, tests have been simulated with the same accuracy as the previous simulation using the supercomputer.

For the power model, a Full Factorial (FF) model has been utilized to generate the DOE test set. In the FF method, the DOE gives all the possible choices for the tests. Using the FF method, 729 cases have been simulated to generate the power model for prediction, and the results of the DOE have been used in the temperature model to improve the model accuracy

Using the results of simulated cases, machine learning models, and a mathematical correlation have been generated for temperature and power loss prediction. Box-Behnken DOE and FF results have been used and combined to generate the prediction models.

2.2.10.3. Mathematical model

For the mathematical model, Rayleigh's method has been chosen for this correlation. Rayleigh's method is a widely used method to generate correlations for different applications in physics and engineering applications [74]. The general formula of this method is shown in Equation 7.

$$R_o = CR_1^a R_2^b R_3^c \dots R_n^m \quad \textbf{Eq. 2-36}$$

where R_o is the output value; C is the correlation constant and was found based on the DOE results; $R_1, R_2 \dots R_n$ are DOE parameters; and $a, b \dots m$ are the powers of the DOE parameters.

For peak temperature and power loss, numerical models are given in the general equations Eq. 2-37 and Eq. 2-38 respectively.

$$T = C \cdot DBFF^a \cdot RPM^b \cdot Dmax^c \cdot cl^d \cdot Tsh^e \cdot Tab^f \cdot NOB^g \cdot (OAR + 1)^h \quad \textbf{Eq. 2-37}$$

$$P = C \cdot DBFF^a \cdot RPM^b \cdot Dmax^c \cdot cl^d \cdot NOB^g \cdot (OAR + 1)^h \quad \textbf{Eq. 2-38}$$

2.2.10.4. Machine learning model

For machine learning models, more than 17 models have been tested to make the prediction model. Gaussian Process (GP) with Matérn 5/2 covariance function $\kappa(\cdot,\cdot)$ has been chosen to generate the model where it has the best prediction and easiest analysis and operation of the model [75].

$$\kappa(S) = \frac{2^{1-\nu}}{\Gamma(S)}\left(\frac{\sqrt{2\nu}S}{l}\right)^{\nu} K_{\nu}\left(\frac{\sqrt{2\nu}S}{l}\right) \quad \textbf{Eq. 2-39}$$

Eq. 2-39 shows the formula of the covariance function for Matérn 5/2, where $\Gamma(r)$ and K_ν are gamma function and modified Bessel function respectively [76, 77], ν is assigned to be 5/2, l is a non-negative parameter and the unit distance is symbolled by S.

In the GP method, the data are assumed to have a distribution function f, where this function is used to estimate the value of the next points. The function value can be described as $f(\cdot) \sim GP\big(m(\cdot), \kappa(\cdot,\cdot)\big)$ (Men), where $m(\cdot)$ is the mean function. The mean function is usually assigned to be zero. The zero value for mean function gives the flexibility for conditional mean to be determined by covariance function.

The methodologies of building the Design of Experiment (DOE) and train the Machine Learning model (ML) are explained in the flow diagram below Figure 2-19. The flow diagram also shows the method and needed parameters to make the predictions for the peak temperature and power loss.

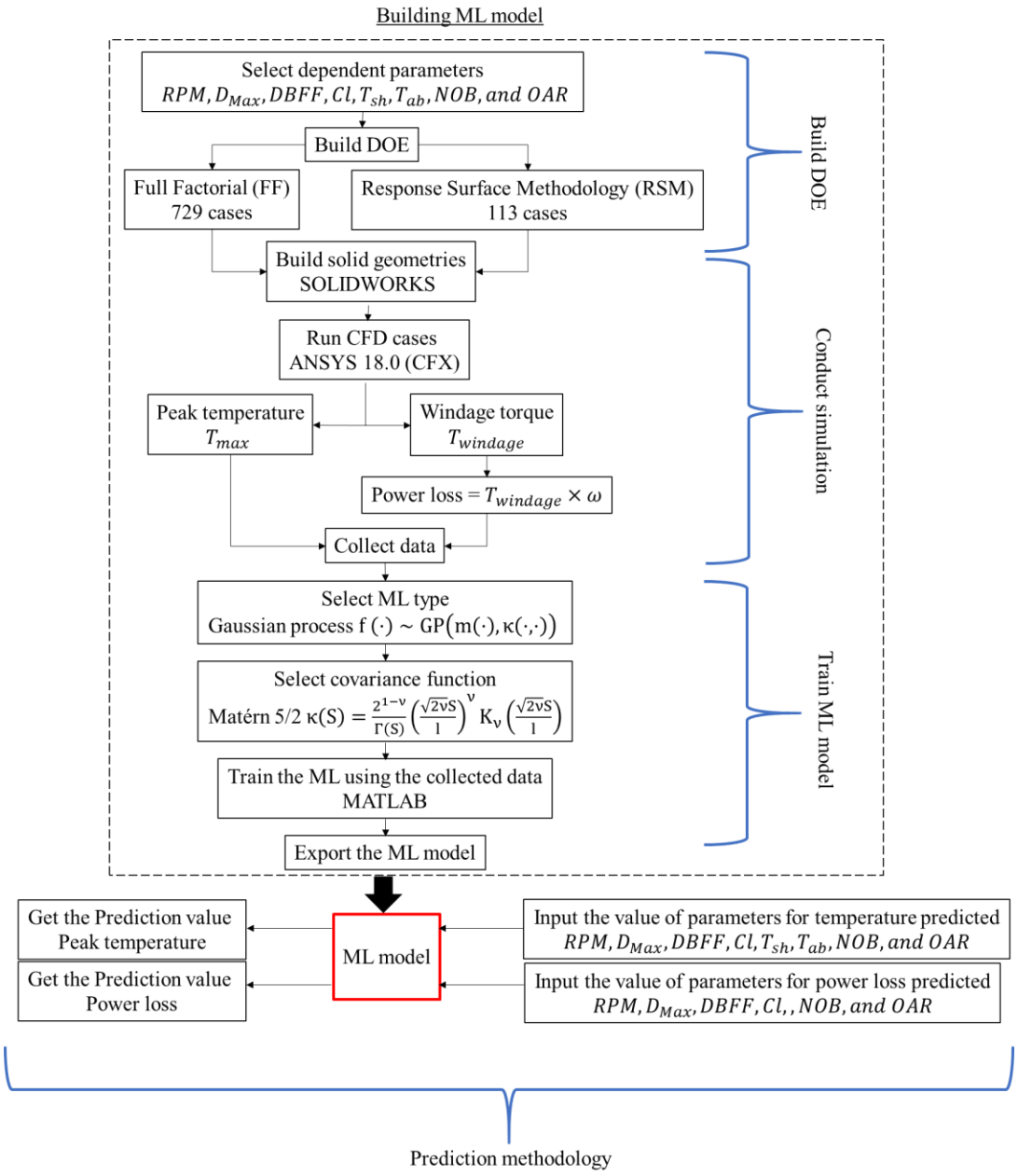

Figure 2-19 Flow diagram for building and using the ML model

2.2.10.5. Prediction model results

The performance of temperature machine learning (ML) prediction models with two types of validation are shown in Figure 2-20, Figure 2-21, and Figure 2-22. Figure 2-20 shows the prediction performance of the machine learning (ML) temperature model trained by RSM dataset for predicting RSM dataset with validation cases.

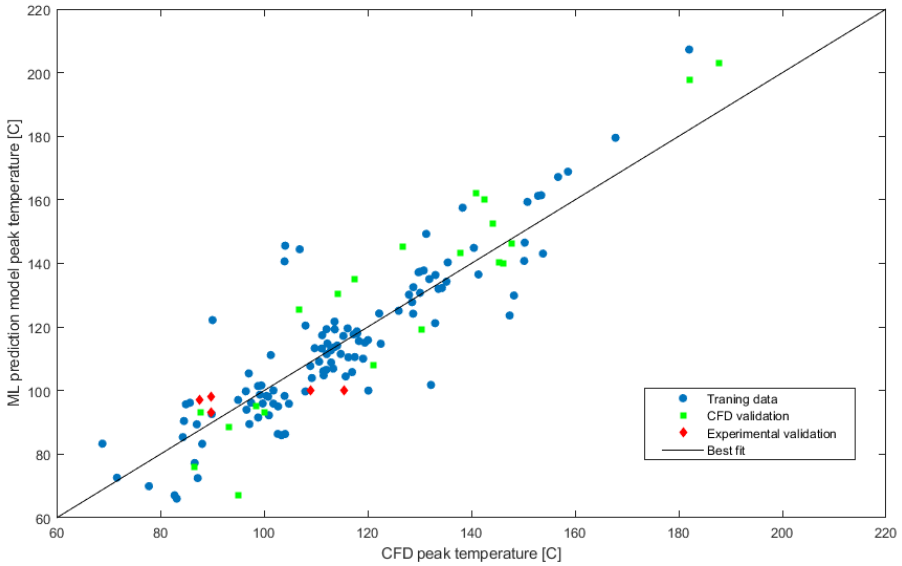

Figure 2-20 Prediction of GP ML temperature model trained by RSM dataset for RSM dataset

The forecast of the machine learning (ML) temperature model trained by the RSM dataset and the machine learning (ML) temperature model trained by the FF dataset for the FF dataset in addition to the validation cases are presented in Figure 2-21 and Figure 2-22 respectively. The green points represent validation cases for the model outside the range of the parameters. Several cases have been tested out of the DOE parameters range to test the accuracy of the model for this situation. The red points are the second validation of the

prediction model. The red points are an experimental result compared with the prediction model.

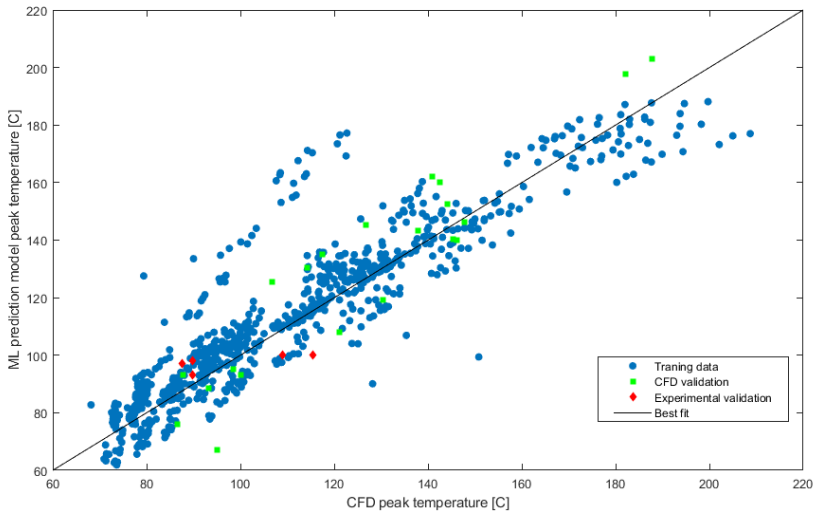

Figure 2-21 Prediction of GP ML temperature model trained by RSM dataset for FF dataset

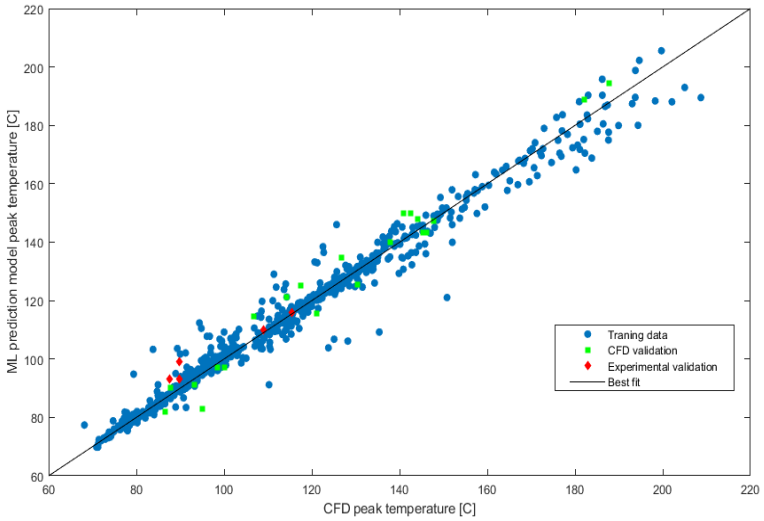

Figure 2-22 Prediction of GP ML temperature model trained by FF dataset for FF dataset

The results show that the machine learning (ML) temperature model trained by the FF dataset has much better predicting performance than the machine learning (ML) temperature model trained by the RSM dataset because the number of the training dataset is much larger in the FF than the RSM.

Figure 2-23, Figure 2-24, and Figure 2-25 are the forecasts for the power loss, in addition to the out of range CFD validation cases. Figure 2-23 and Figure 2-24 are the predictions of the machine learning (ML) power loss model trained by the RSM dataset for the RSM and the FF dataset, respectively. Figure 2-25 shows the prediction of the machine learning (ML) power loss model trained by the FF dataset for the FF dataset.

As noticed in the temperature models, the machine learning (ML) power loss model trained by the FF dataset has more reliable results than the machine learning (ML) power loss model trained by the RSM dataset for both training data and validation cases. The number of cases in the training dataset of the machine learning (ML) power loss model trained by FF dataset is more than 10 times the training dataset in the machine learning (ML) power loss model trained by RSM dataset, where this improved the accuracy of the prediction model significantly.

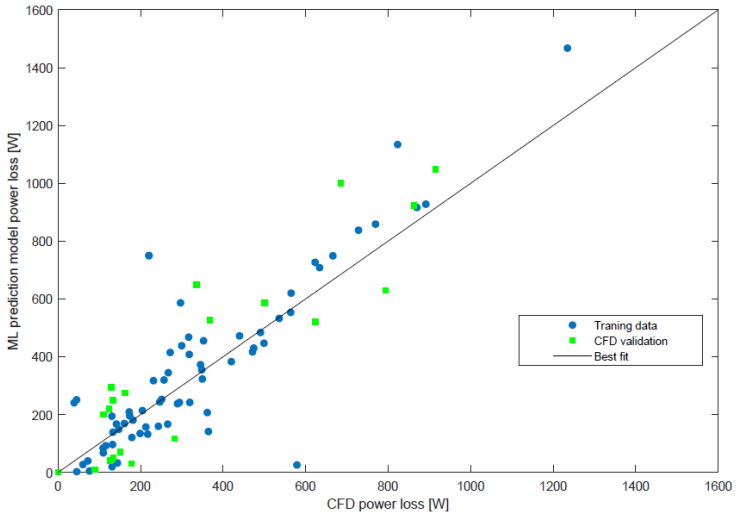

Figure 2-23 Prediction of GP ML power loss model trained by RSM dataset for RSM dataset

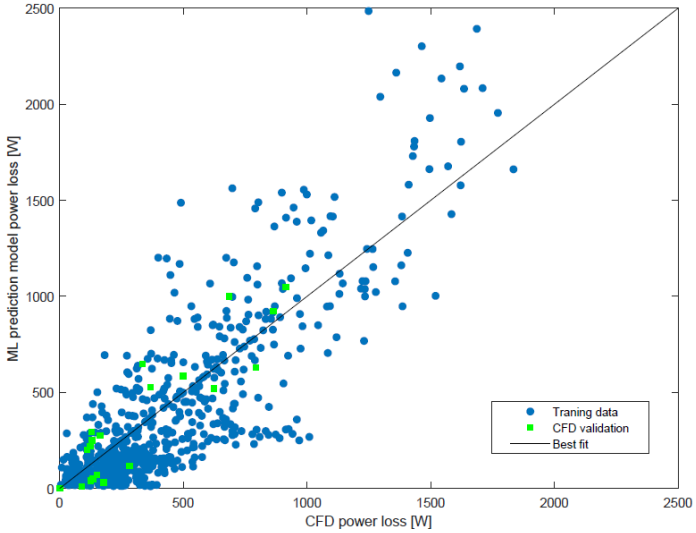

Figure 2-24 Prediction of GP ML power loss model trained by RSM dataset for FF dataset

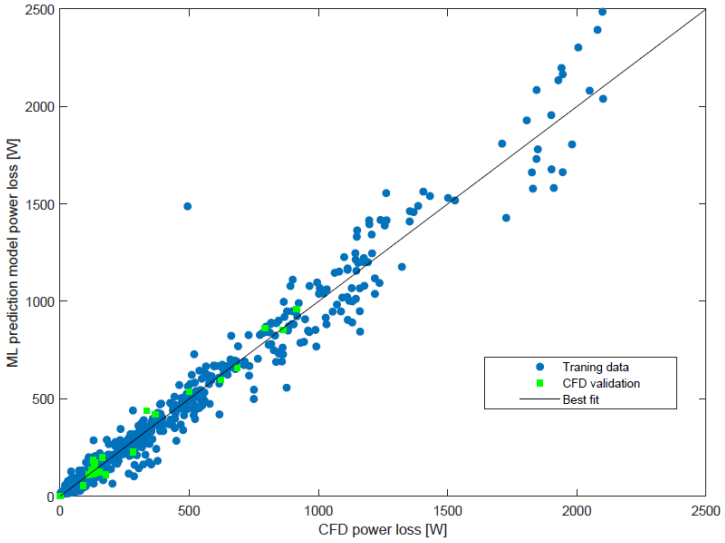

Figure 2-25 Prediction of GP ML power loss model trained by FF dataset for FF dataset

2.2.10.6. Improving the accuracy of the machine learning model

The performance of the prediction models could be improved by making some data transformation. The goal of transforming the data is to reduce the range of the target parameter (dependent variable). This reduction in the range may improve the prediction significantly [78]. Log transformation is a very common data transformation method [79, 80]. The Log transformation is chosen for the system because the standard deviation is proportional to the mean of the data [81]. The log transformation applied by taking the Log for the target parameter value. Use the transferred data to train the machine learning model. The trained model predicting the Log of the target parameter, so take the exponential for the predicted number to get the correct value of the parameter [81]. This method has been applied to improve the prediction of the RSM machine learning model. The results of the updated model represented in Figures Figure 2-26Figure 2-27, 22, Figure 2-.

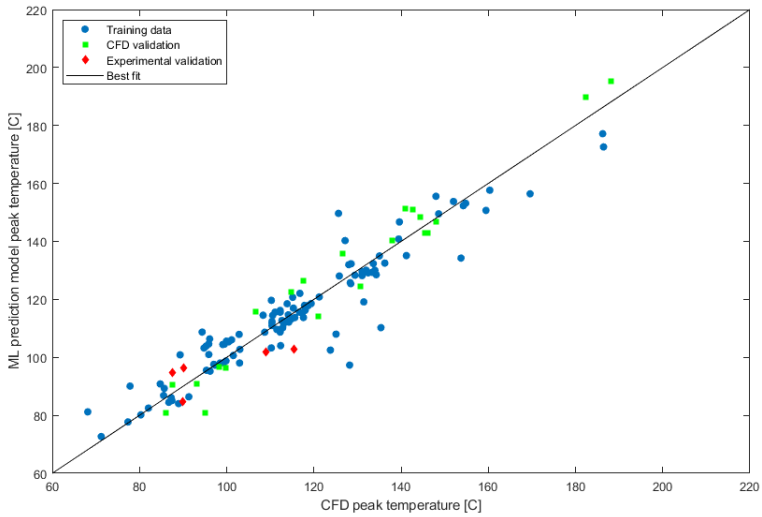

Figure 2-26 Prediction of GP ML temperature model trained by Log transformed RSM dataset for RSM dataset

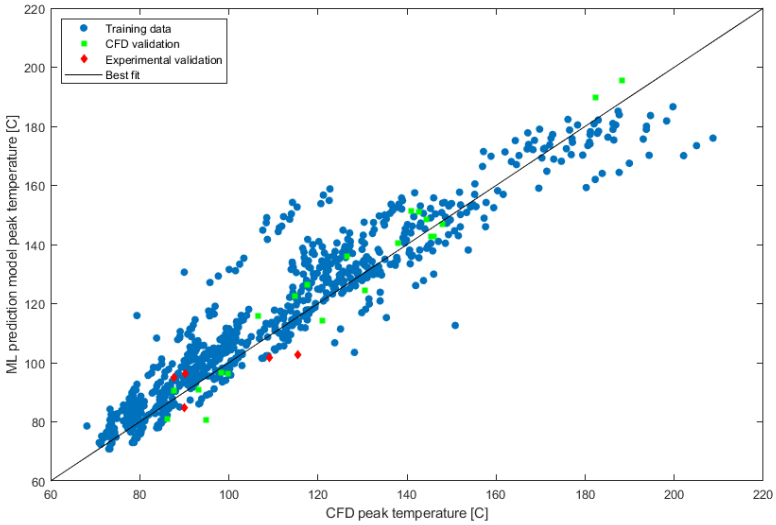

Figure 2-27 Prediction of GP ML temperature model trained by Log transformed RSM dataset for FF dataset

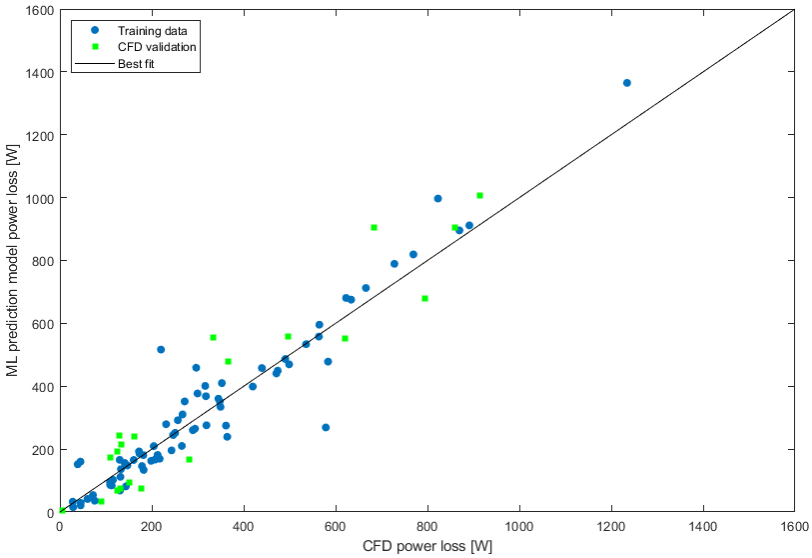

Figure 2-28 Prediction of GP ML power loss model trained by Log transformed RSM dataset for RSM dataset

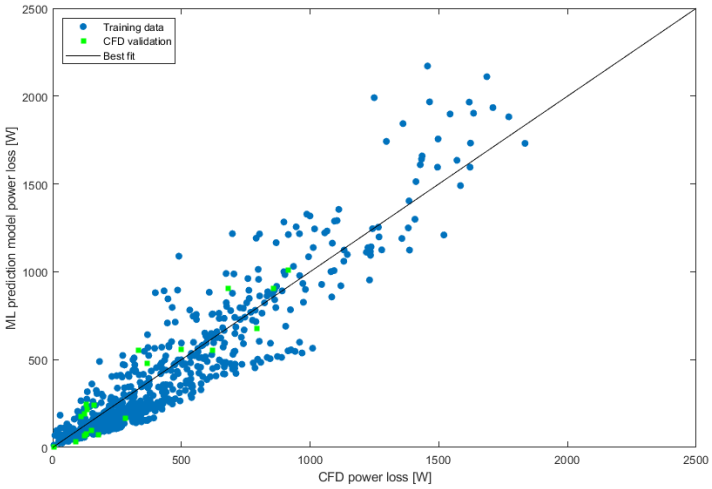

Figure 2- Prediction of GP ML power loss model trained by Log transformed RSM dataset for FF dataset

The result of the trained model using Log transformed data shows an improvement in the prediction for machine learning (ML) power loss model trained by the RSM dataset. Table 2-5 below shows a comparison in the R2 and the standard deviation between the machine learning (ML) power loss model trained by RSM dataset used the original data and the machine learning (ML) power loss model trained by RSM dataset used the transferred data.

Table 2-5 Comparison between the RSM model trained by original data and RSM model trained by Log transformed data

The results of the model	**R^2 for RSM (Original data)**	**R^2 for RSM (Log transferred data)**
GP ML temperature model trained RSM dataset for predicting RSM dataset	$\mathbf{R^2}$=0.786 $\boldsymbol{\sigma}$ = 24.47	$\mathbf{R^2}$= 0.887 $\boldsymbol{\sigma}$ = 20.37
GP ML temperature model trained RSM dataset for predicting FF dataset	$\mathbf{R^2}$= 0.838 $\boldsymbol{\sigma}$ = 29.53	$\mathbf{R^2}$= 0.893 $\boldsymbol{\sigma}$ = 28.41
GP ML power loss model trained RSM dataset for predicting RSM dataset	$\mathbf{R^2}$= 0.757 $\boldsymbol{\sigma}$ = 293.16	$\mathbf{R^2}$= 0.903 $\boldsymbol{\sigma}$ = 260.75
GP ML power loss model trained RSM dataset for predicting FF dataset	$\mathbf{R^2}$= 0.710 $\boldsymbol{\sigma}$ = 4501.68	$\mathbf{R^2}$ = 0.858 $\boldsymbol{\sigma}$ = 3967.7

A numerical formula has been generated for power loss and peak temperature prediction for the coupling and coupling guard, respectively.

The collected data has been used to evaluate the coefficients of parameters of the formula in Eq. 2-37 and Eq. 2-38. The final formula for peak temperature and power loss shown below in equations Eq. 2-40 and Eq. 2-41 respectively.

$$T = 0.00076\mathrm{DBFF}^{-0.03455}\mathrm{RPM}^{0.765}\mathrm{Dmax}^{0.735}\mathrm{cl}^{-0.0895}\mathrm{Tsh}^{0.6793}\mathrm{Tab}^{0.005} \times \mathrm{NOB}^{-0.0801}(\mathrm{OAR}+1)^{0.0444} \quad \textbf{Eq. 2-40}$$

$$P = 1.535 \times 10^{-12}\mathrm{DBFF}^{0.20837}\mathrm{RPM}^{2.832}\mathrm{Dmax}^{2.8792}\mathrm{cl}^{0.1365}\mathrm{NOB}^{-0.6785} \times (\mathrm{OAR}+1)^{0.78036} \quad \textbf{Eq. 2-41}$$

Figure 2-29 and Figure 2-30 present the accuracy of the numerical formula for peak temperature and power loss respectively.

The figures show a low accuracy for the numerical model for high power loss and peak temperature. On the other hand, the model has great performance at low power loss and peak temperature.

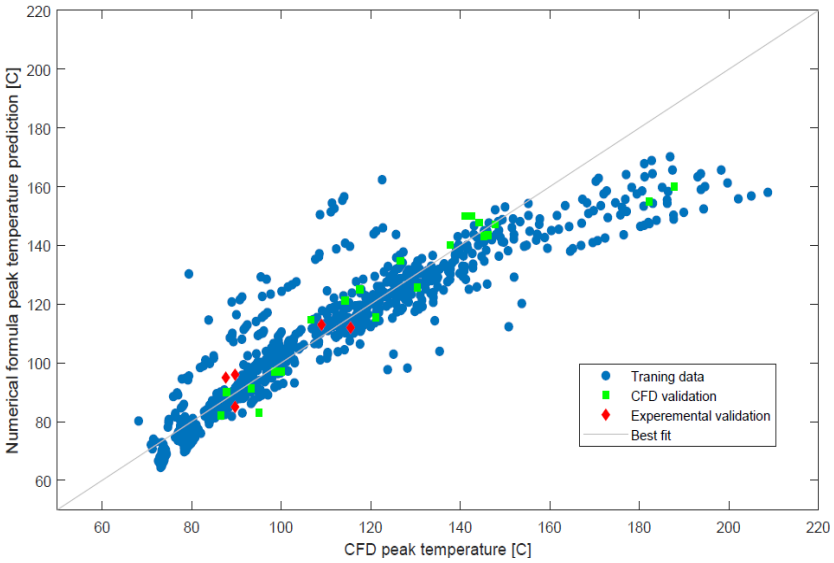

Figure 2-29 Empirical formula prediction for temperature using the FF design of experiment training data

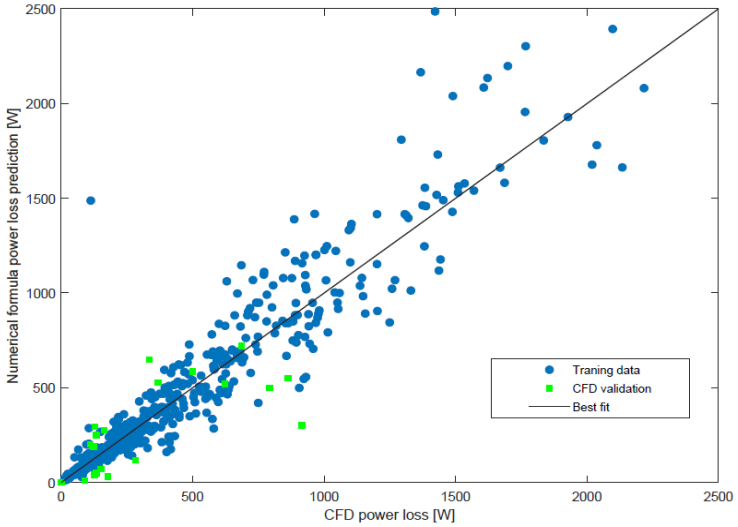

Figure 2-30 Empirical formula prediction for power loss using FF design of experiment training data

2.2.11. Case study

A case study has been done for more explanation for the parameters required to use the ML model. Table 2-6 shows the values of the parameters of the case study. The result of the ML prediction model was compared with the CFD, experimental, and empirical formula results. This comparison is shown in Table 2-7.

Table 2-6 Case study for ML model and empirical formula prediction

Parameter	Value of the parameter
Rotating speed (RPM)	7000 rpm
Maximum diameter (D_{max})	43 cm
Distance between flanges (DBFF)	20.2 cm
Clearance (Cl)	4 cm
Shaft temperature (T_{sh})	50 ℃
Ambient temperature (T_{ab})	27℃
Number of bolts (NOB)	20
Oil to air ratio (OAR)	0

Table 2-7 ML and empirical formula prediction comparing with CFD and experiment results.

Method	Experimental	CFD simulation	Machine learning	Empirical formula
Peak Temperature	95.4 ℃	94.9 ℃	93.7 ℃	92.3℃

3. GEARS

3.1. Introduction

Analyzing the power loss in the gears is very complicated. Simulating the sliding power loss considered the most complicated simulation due to the very thin layer of lubrication. Using commercial software is very limited for this type of simulation. Making the simulation for the fluid film layer using commercial software will realize many problems. The first problem is the high number of elements that will lead to out of memory for the computer. The second problem is the very long time and high memory to make this transient simulation. The third problem the convergence problem for the simulation because the mesh will break because the lubricating film layer is very small. All these problems I have faced when I tried to simulate using the commercial software. The second method of simulation is the manual mesh for the gear surface and build our code to make the simulation. The second method was followed to make this simulation. Several studies have been proposed the Thermo-Elastohydrodynamic Lubrication (TEHL) simulation for the lubricating fluid between the teeth of the gears [82].

Figure **3-1** shows the contact steps between the teeth of gears (Beginning of contact to the end of contact). The figure also shows the simulating region for the lubricating fluid film. The meshes that have been used in the simulation are included in the figure. The chapter will include a full description of the TEHL simulation for the lubricating fluid film

with a 3D simulation for the tooth material. The results will include the thermal distribution in gears and lubricating fluid film, thermal stress, and thermal deformation in the tooth. The simulation includes analysis for the Standard Contact Ratio (SCR) [83] and High Contact Ratio (HCR) gears [84]. The results have a comparison between the standard and high contact gears. The chapter also includes a prediction model for the sliding power loss in the tooth.

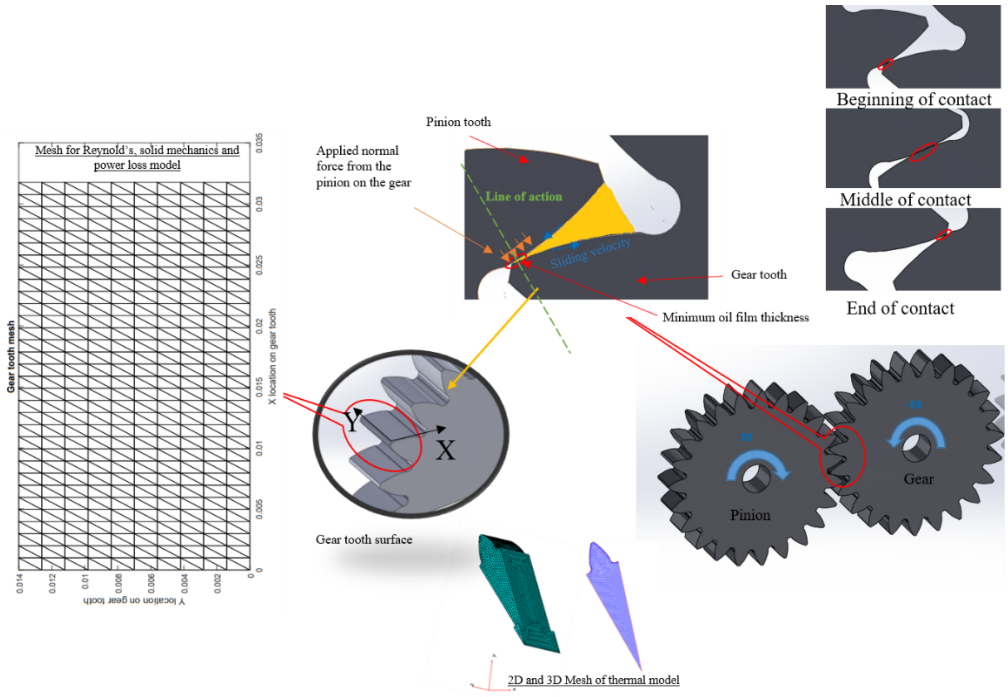

Figure 3-1 Description for the sliding power loss problem in gears

3.2. Methodology

3.2.1. Sliding velocity between teeth

During the contact between the teeth, there is sliding is happening. Determining the velocity of this sliding between the teeth is important. The importance of sliding velocity is using the sliding velocity as a boundary velocity for solving the Reynolds equation.

The sliding velocity is varying along the line of action. The description for calculating the sliding velocity between the teeth shown in Eq. 3-1 [85].

$$u_s = u_{rp} - u_{rg} \quad \textbf{Eq. 3-1}$$

Where u_s is the sliding velocity. u_{rp} and u_{rg} are the rolling velocity for the pinion and the gear, respectively.

The rolling velocities for the pinion and the gear are shown in Eq. 3-2 and Eq. 3-3 [85].

$$u_{rp} = \frac{2\pi R_p}{60} n_p \quad \textbf{Eq. 3-2}$$

$$u_{rg} = \frac{2\pi R_g}{60} n_g \quad \textbf{Eq. 3-3}$$

The symbols ρ_p and ρ_G are the radius of curvature for the pinion and the gear, respectively. n_p and n_G are the number of teeth for the pinion and the gear, respectively.

3.2.2. Thermo-Elastohydrodynamic (Mathematical model)

3.2.2.1. Energy equation

The properties of the lubricant oil depend on temperature and pressure. To investigate the thermal effect on the fluid film the energy equation should be solved. Eq. 3-4 Eq the general transient form of the energy equation. The equation describes the terms of the energy equation that applied to the fluid film. The equation contains four main terms which are compression, viscous dissipation, convection, and conduction terms.

$$\underbrace{v \cdot T \cdot \left(U \underbrace{\frac{\partial p}{\partial x}} + V \underbrace{\frac{\partial p}{\partial y}}\right)}_{Compression} + \underbrace{\mu \cdot \left[\left(\frac{\partial U}{\partial z}\right)^2 + \left(\frac{\partial V}{\partial z}\right)^2\right]}_{\text{Viscous dissipation}} =$$

$$\underbrace{\rho \cdot c_p \cdot \left[\frac{\partial T}{\partial t} + U \underbrace{\frac{\partial T}{\partial x}} + V \underbrace{\frac{\partial T}{\partial y}}\right]}_{Heat\ convection} - \underbrace{k \cdot \left[\frac{\partial^2 T}{\partial x^2} + \frac{\partial^2 T}{\partial y^2} + \frac{\partial^2 T}{\partial z^2}\right]}_{Heat\ conduction} \quad \textbf{Eq. 3-4}$$

3.2.2.2. Energy equation assumptions

To solve the energy equation a few assumptions have been used to simplify the energy equation. The compression term usually neglected because the pressure gradient in the x and y direction is neglected at the point of contact by assuming a flat contact line at the point of contact [43].

$$\frac{\partial p}{\partial x} = \frac{\partial p}{\partial y} = 0 \quad \textbf{Eq. 3-5}$$

For the viscous dissipation term, the fluid velocity in the y-direction is neglected.

$$\frac{\partial V}{\partial z} = 0 \quad \textbf{Eq. 3-6}$$

To simplify the convection term, the temperature gradient in the Y-direction is neglected.

$$\frac{\partial T}{\partial y} = 0 \quad \textbf{Eq. 3-7}$$

In the convection term, the temperature gradient in the Y-direction is neglected.

$$\frac{\partial^2 T}{\partial y^2} = 0 \quad \textbf{Eq. 3-8}$$

The energy equation has been solved using the slicing technique as shown in Figure 3-2 [86]. This method is a block moving in the X-direction. In each time step, the block

moves one step. While the block is moving, the new boundary conditions and assumptions are applied.

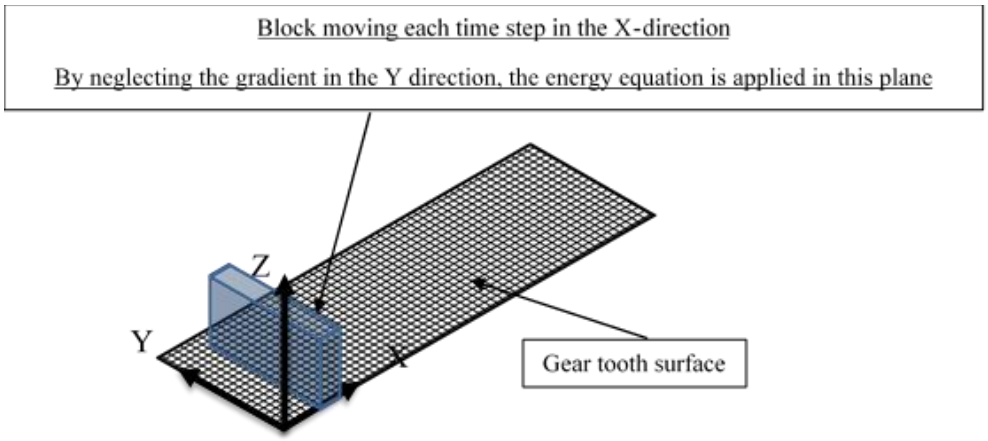

Figure 3-2 slicing technique to solve for the sliding power loss

The final form of the energy equation after simplification is shown in Eq. 3-9.

$$\mu \underbrace{\cdot\left[\left(\frac{\partial U}{\partial z}\right)^2\right]}_{\text{Viscous dissipation}} = \underbrace{\rho \cdot c_p \cdot \left[\frac{\partial T}{\partial t} + U\frac{\partial T}{\partial x}\right]}_{Heat\ convection} - \underbrace{k \cdot \left[\frac{\partial^2 T}{\partial x^2} + \frac{\partial^2 T}{\partial z^2}\right]}_{Heat\ conduction} \qquad \textbf{Eq. 3-9}$$

The viscose dissipation term is the source of the heat in the lubricant fluid film. The convection is the heat transfer in the moving fluid. The conduction term is the heat transfer in the stationary layers of the fluid.

including the transient term in the solution is important because the contact between the gears happened very fast. The convection term will cause an oscillation in the numerical solution [87]. This problem could be solved by various methods. In this work, the Up-Wind scheme method will be used to solve the oscillation problem as will presented later [87].

3.2.2.3. Reynolds equation

Reynolds equation used to evaluate the pressure for the fluid film between the contacted teeth. The general form of the Reynolds equation presented in Eq. 3-10. The equation will be simplified to a one-dimensional form. The equation will be solved in the X coordinate since the pressure gradient in the Y direction neglected.

$$\frac{\partial}{\partial x}\left(\frac{\rho h^3}{\mu}\frac{\partial p}{\partial x}\right)+\frac{\partial}{\partial y}\left(\frac{\rho h^3}{\mu}\frac{\partial p}{\partial y}\right)=6v+\frac{\partial(\rho h)}{\partial x}+\underbrace{6\rho h\frac{\partial U}{\partial x}}_{Stretch}+\underbrace{12\frac{\partial(\rho h)}{\partial t}}_{Squeezs} \qquad \textbf{Eq. 3-10}$$

3.2.2.4. Reynolds equation assumptions

The sliding velocity for the surface of the first tooth and the velocity of the surface of the second tooth have the same magnitude but opposite direction $U_1 = -U_2$ Figure 3-3. Also, the change of pressure along the Y-axes in neglected for the line contact. Since the change in the film thickness is very fast during the rotation the transient term (Squeeze term) should be considered. The simplified form for the Reynolds equation to describe the pressure of the fluid film can be written as shown in Eq. 3-11 [88].

$$\frac{\partial}{\partial x}\left(\frac{\rho h^3}{\mu}\frac{\partial p}{\partial x}\right)=12u_s\frac{\partial(\rho h)}{\partial x}+12\frac{\partial(\rho h)}{\partial t} \qquad \textbf{Eq. 3-11}$$

where u_s is the sliding velocity. The negative pressure of the nodes was assumed to be zero to avoid the cavitation of the negative values.

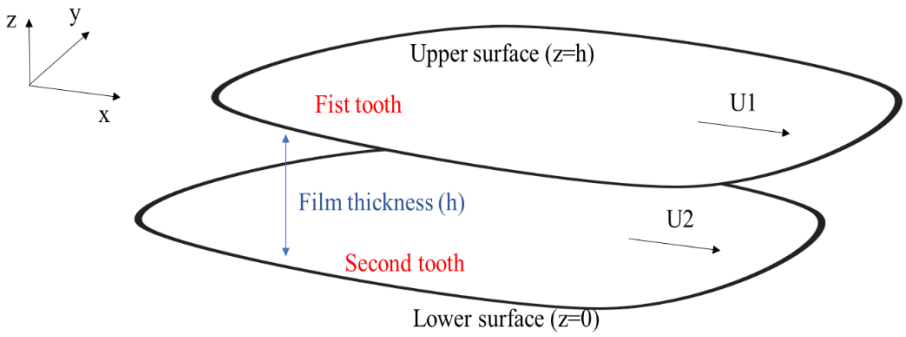

Figure 3-3 Velocity of the surfaces and film thickness

3.2.2.5. Mesh of the gear tooth surface

The finite element method has been used to solve the Reynolds equation. For this purpose, a mesh has been generated manually. This mesh generated by specifying the size of the element and the distance between the nods. Each element has a triangular shape with 3 nodes. Figure 3-4 shows the mesh that has been used to solve the energy equation. The figure of the 2D mesh below contains 320 elements. All the elements have a triangular shape as clear in the figure below.

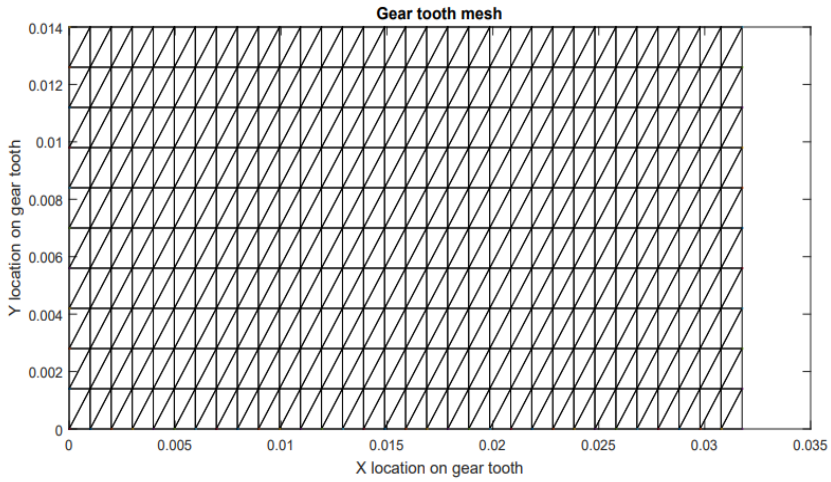

Figure 3-4 2D mesh for the surface of the gear tooth

This mesh also has been used to calculate the elastic deflection in the tooth, the film thickness along the line of action, and the sliding power loss along the line of action.

3.2.2.6. Film thickness

The film thickness equation has three terms as shown in Eq. 3-12. The first term is h_o which is the film thickness for rigid contact. The second term is the deflection from elastic contact. This term used after calculating the rigid contact to update the film thickness.

$$h(x) = h_o + \frac{x^2}{2R} + d(x) \qquad \textbf{Eq. 3-12}$$

To update the film thickness and calculate the elastic deformation the equivalent radius of curvature should be calculated. Eq. 3-13 is the equivalent radius of curvature for the gear tooth.

$$\frac{1}{R} = \frac{1}{R_1} + \frac{1}{R_2} \qquad \textbf{Eq. 3-13}$$

3.2.2.7. Elastic deflection

The elastic deformation along the line of action can be calculated by Eq. 3-14 [89].

$$d(x) = -\frac{4}{\pi E'} \int_{-\infty}^{\infty} ln \left| \frac{x-x'}{x_o} \right| p(x')dx' \qquad \textbf{Eq. 3-14}$$

The term is E' the equivalent modulus of elasticity for the gear tooth. The value of E' calculated by Eq. 3-15 [89].

$$\frac{2}{E\prime} = \frac{1-v_1^2}{E_1} + \frac{1-v_2^2}{E_2}$$ **Eq. 3-15**

3.2.2.8. Load balance

The load of the contact is carried by the fluid for pure hydraulic lubrication [89]. The normal pressure in the fluid calculated by Reynolds equation multiplies the area of the elements that must be equal to the normal force on the tooth from carrying the input torque at the point of contact shown in Eq. 3-16.

$$w = \iint_{\Omega} p(x,y)dxdy$$ **Eq. 3-16**

where w is the normal force at the point of contact from the input torque. The $p(x,y)$ is the hydraulic lubrication carried by the lubricant at the point of contact as calculated by the Reynolds equation. The analysis of the normal force will be described late.

3.2.2.9. Contact area

Hertzian contact theory has been used to calculate the contact area. The area of contact based on this theory is

$$a = \sqrt{\frac{8F_N R}{\pi b E\prime}}$$ **Eq. 3-17**

where F_N is the normal force on the contact region, b is the thickness of the gear tooth.

3.2.2.10. Newton's law of viscosity

Newton's law has been utilized to calculate the finite shear stress at each element. This finite shear stress will be used later to calculate the sliding power loss. As shown in

Eq. 3-18 the finite shear stress is equal to the negative value of the viscosity multiplied by the velocity gradient along with the fluid film. The velocity profile has been assumed as a linear profile because the thickness of the fluid film is very small [90].

$$\tau = -\mu \frac{du_s}{dz} \quad \textbf{Eq. 3-18}$$

3.2.2.11. Sliding power loss

The main purpose of the analysis to calculate the sliding power loss between the contacted teeth. The sliding power loss has been calculated by making the integration for the finite shear stress and sliding velocity for each element area as shown in Eq. 3-19.

$$P_s = \iint_{\Omega} \tau \cdot u_s dxdy \quad \textbf{Eq. 3-19}$$

3.2.2.12. Lubricant properties

In the gear system, the temperature becomes very high due to the sliding power loss and the windage with the fluid. The pressure also is very high at the contact point between gears. These two factors have been taken into consideration to update the properties of the lubricant. Eq. 3-20, Eq. 3-21, Eq. 3-22, and Eq. 3-23 show the formulas to update the thermal conductivity, viscosity, specific heat, and viscosity of the lubricant respectively [91, 92, 93].

$$k = k_0(0.75 + 0.25\sqrt{1 + p \cdot 2 \times 10^{-8}} \quad \textbf{Eq. 3-20}$$

$$\rho = \rho_0 \left(1 - \alpha_\rho (T - T_0)\right)\left(1 + \frac{0.34615p}{0.59263\times10^9 + p}\right) \quad \textbf{Eq. 3-21}$$

$$C_p = C_{p0}\left(1 + \alpha_{cp}(T - T_0)\right) \quad \textbf{Eq. 3-22}$$

$$\mu = \mu_\infty \left(\frac{\mu_{f0}}{\mu_{f\infty}}\right)^{\left(1+\frac{p}{pr}\right)^z \cdot \left(\frac{T_0+135}{T+135}\right)^{S0}} \quad \textbf{Eq. 3-23}$$

The formulas used to update the properties of the lubricant show a different dependency on temperature and pressure for each property. The meaning and values of the constants in the above equations are listed below.

- k: Thermal conductivity of the fluid $\left[\frac{W}{m.K}\right]$
- k_0: The reference thermal conductivity of the fluid $\left[\frac{W}{m.K}\right]$
- p: The pressure of the fluid [Pa]
- ρ: The density of the fluid $[kg/m^3]$
- ρ_0: The reference density $[kg/m^3]$
- α_ρ: Lubricant dependent constant (0.00079) $[1/^oC]$
- T: The temperature of the fluid [K]
- T_0: The reference temperature of the fluid [K]
- C_p: The specific heat capacity of the fluid $\left[\frac{J}{kg.K}\right]$
- C_{p0}: The reference specific heat capacity of the fluid $\left[\frac{J}{kg.K}\right]$
- α_{cp}: Temperature coefficient of specific heat (4.1) $\left[\frac{J}{kg.K}\right]$
- μ: The viscosity of the fluid [Pa.s]

- μ_∞: Constant (6.31×10^{-5}) [Pa.s]
- μ_0: The reference viscosity [Pa.s]
- pr: Constant ($196..2 \times 10^{6}$) [Pa]
- Z: Viscosity-pressure index (0.87)
- s_0: Viscosity-temperature index (1.2)

The reference values of the properties are listed in table **Table 3-3**.

3.2.2.13. Solving the energy equation for the lubricant

Solving the energy equation for the fluid film was the most challenging part. The reason for that is the high number of steps required to find the solution Figure 3-5. Besides that, the solution needs to make an interpolation between two types of meshes and combine two solving methods (Finite Element Method (FEM) and Finite Difference Method (FDM)) to solve the problem.

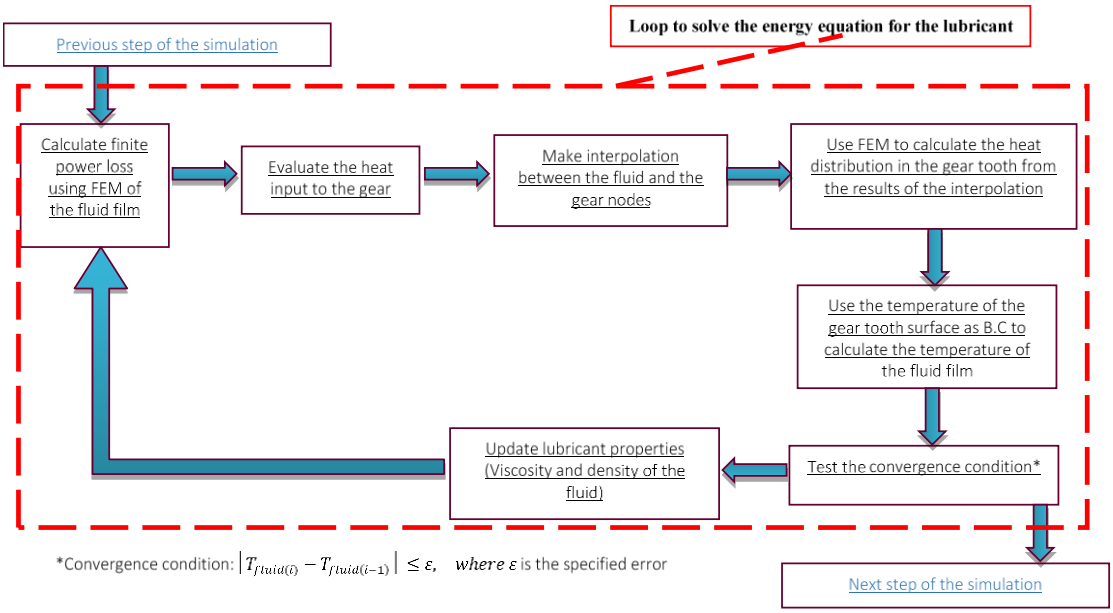

Figure 3-5 Flow steps to solve the energy equation of the lubricating fluid

The solution of the energy equation will be utilized to update the properties of the fluid. The finite difference method has been used to solve the transient energy equation [94]. The energy equation will be solved each time step. For the energy equation, the Z coordinate is varying from 0 at the first surface to calculated h on the second surface. The coordinate X is changing from 0 which is the beginning of contact to X_0 at the end of the contact. The term $\frac{\partial T}{\partial x}$ has been solved by three-point backward difference formula. The central difference formula used for $\frac{\partial^2 T}{\partial z^2}$ term.

The subscripts $i\ and\ j$ are for X and Z coordinate respectively as shown in Eq. 3-24.

$$x = x_i,\ z = z_j$$ **Eq. 3-24**

The transient term should be considered in solving the energy equation. The importance of considering the transient term is because the contact and the change in temperature in the lubrication layer occur very fast. k is the time step for the energy equation. The solution has been divided into 32-timesteps from the beginning of contact to the end of the contact.

$$t^k = t$$ **Eq. 3-25**

The first two time steps are neglected to apply a three-point backward difference as shown in Eq. 3-26.

$$\frac{\partial T_{i,j}^k}{\partial x} = \frac{3T_{i,j}^k - 4T_{i-1,j}^k + 2T_{i-2,j}^k}{2\Delta x}$$ **Eq. 3-26**

The last time step also was neglected to use the central difference formula as appearing in Eq. 3-27.

$$\frac{\partial^2 T_{i,j}^k}{\partial z^2} = \frac{T_{i,j+1}^k - 2T_{i,j}^k + T_{i,j-1}^k}{\Delta z^2}$$ **Eq. 3-27**

The problem in solving the energy equation is the convection term $\frac{\partial T}{\partial x}$. Including the convection term in the solution will lead to an oscillation in the solution [87]. The upwind scheme method has been used to solve this problem. The compact form of the upwind scheme presented in Eq. 3-28.

$$u_i^{n+1} = u_i^n - \Delta t[a^+ u_x^- + a^- u_x^+]$$ **Eq. 3-28**

The explanation for the terms of the compact form is shown in Eq. 3-29 and Eq. 3-30.

$$u_x^- = \frac{u_i^n - u_{i-1}^n}{\Delta x}$$ **Eq. 3-29**

$$u_x^+ = \frac{u_{i+1}^n - u_i^n}{\Delta x}$$ **Eq. 3-30**

a^+=max(a,0) **Eq. 3-31**

a^-=min(a,0) **Eq. 3-32**

The final form of the upwind scheme is viewed in the Eq. 3-33 and Eq. 3-34.

$$\frac{u_i^{n+1} - u_i^n}{\Delta t} + a\frac{u_i^n - u_{i-1}^n}{\Delta x} = 0 \; for \; a > 0$$ **Eq. 3-33**

$$\frac{u_i^{n+1} - u_i^n}{\Delta t} + a\frac{u_{i+1}^n - u_i^n}{\Delta x} = 0 \; for \; a < 0$$ **Eq. 3-34**

The energy equation has been solved using the upwind scheme. A numerical code has been developed using MATLAB to solve the equation.

3.2.2.14. Boundary conditions of the energy equation

Figure 3-6 shows the coordinate and the location of boundary conditions for the lubricant's energy equation.

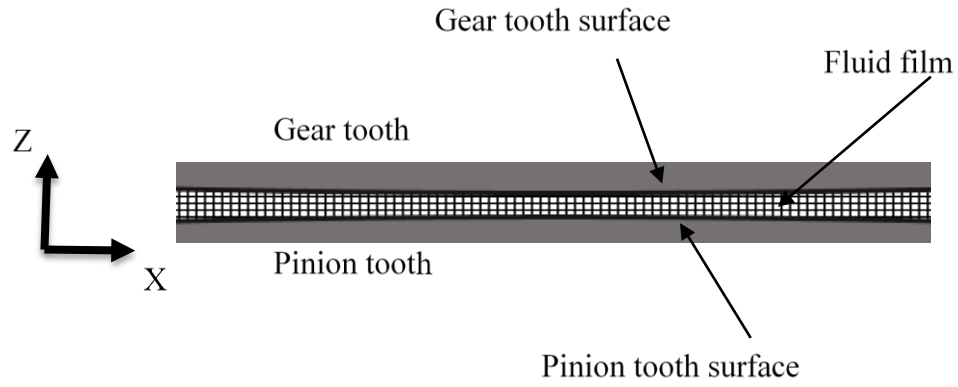

Figure 3-6 Fluid film between the gears teeth

The boundary and initial conditions for the energy equation are shown below. The first boundary conduction is at the surface of the first tooth.

$$T|_{z=0} = T_{Tooth1}$$

The second initial conduction is at the surface of the second tooth.

$$T|_{z=h} = T_{Tooth2}$$

The boundary condition at the inlet and the exit of the oil are

$$T|_{Xin} = T|_{Xout} = 50℃$$

The initial condition is

$$T|_{t=0} = 50℃$$

Other conditions should be applied to ensure an accurate solution. The first condition is the continuity of the temperature at the contact margin between the lubricant and the gear surface. The second condition is the continuity in heat flux at the boundaries as shown in Eq. 3-35, Eq. 3-36, and Eq. 3-37.

$$k_f \frac{\partial T}{\partial Z} = k \frac{\partial T}{\partial Z} \quad \textbf{Eq. 3-35}$$

$$T|_{z=0} = T_{Tooth1} \quad \textbf{Eq. 3-36}$$

$$T|_{z=h} = T_{Tooth2} \quad \textbf{Eq. 3-37}$$

Figure 3-7 shows the FDM grid and boundary conditions. The distance between every two nodes is $\Delta X = \frac{a}{10 \cdot b}$ mm in the X-axes direction, where a is the area of the contact region and b is the thickness of gear tooth. The distance between any 2 nodes in the Y-axes

direction is $\frac{h_{min}}{10}$. The velocity of the fluid had linear profile between the teeth. The sliding velocity used to evaluate the equation of the velocity profile.

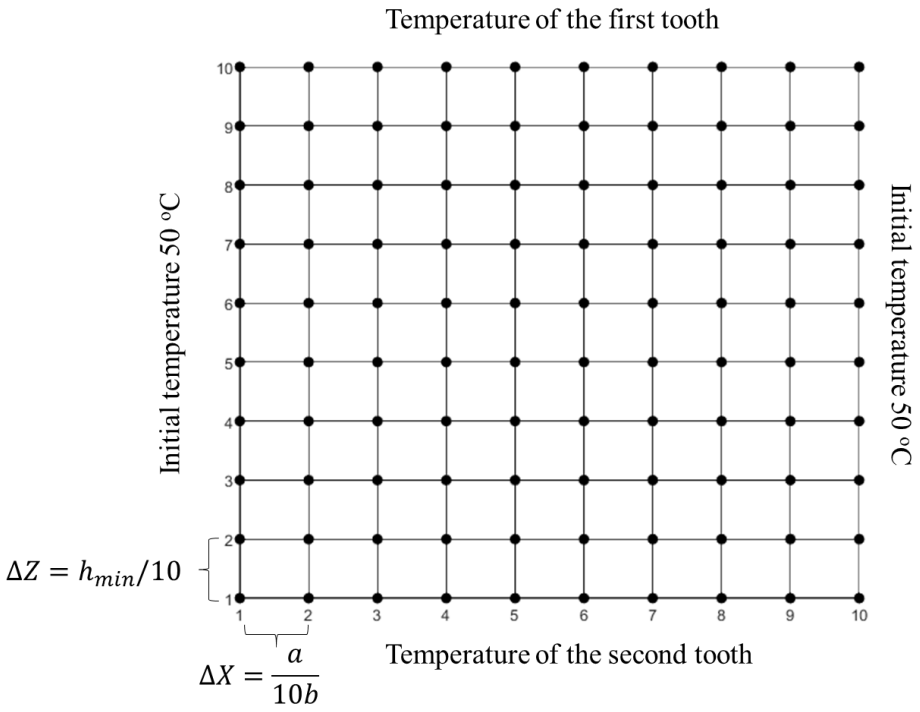

Figure 3-7 Finite Difference Method (FDM) grid and boundary conditions

3.2.3. Gear analysis

The thermal analysis for the gear tooth is important because the temperatures of the teeth will be used as boundary conditions for the lubricant's energy equation. Eq. 3-38 is a general three-dimensional heat conduction equation in a transient form [95]. This equation should be solved each time step. The solution of the transient conduction equation keeps updated until the system reaches a steady state.

$$\underbrace{\rho_s c_{ps} \frac{\partial T_s}{\partial t}}_{\substack{Rate\ of \\ heat\ change}} = \underbrace{k_s \left[\frac{\partial^2 T_s}{\partial x^2} + \frac{\partial^2 T_s}{\partial y^2} + \frac{\partial^2 T_s}{\partial z^2}\right]}_{Heat\ conduction} \quad \textbf{Eq. 3-38}$$

where $\rho_s, c_{ps}\ and\ k_s$ are the gear material density, thermal capacity, and thermal conductivity, respectively.

3.2.3.1. Gear tooth temperature

Based on the conservation of energy, the generated heat from the sliding between gears will transfer to (1- Lubricant fluid 2- Gear tooth 3- pinion tooth) as in Eq. 3-39.

$$q_{gen} = q_f + q_g + q_p \quad \textbf{Eq. 3-39}$$

The factor γ in the equations Eq. 3-40 and Eq. 3-41 is controlling the ration of heat that will transfer to the solids and the part of the heat will transfer to the lubricant fluid. The typical value for γ is 0.9- 0.95 [95].

$$q_f = (1 - \gamma) \cdot q_{gen} \quad \textbf{Eq. 3-40}$$

$$q_g + q_p = \gamma \cdot q_{gen} \quad \textbf{Eq. 3-41}$$

Where

q_{gen}: The generated heat from the sliding power loss

q_f: The part of the heat stays in the fluid

q_g: The part of the heat transferred to the gear

q_p: The part of the heat transferred to the pinion

$$\beta_i = \frac{\sqrt{\mu_i \rho_i c_i V_i}}{\sqrt{\mu_1 \rho_1 c_1 V_1} + \sqrt{\mu_2 \rho_2 c_2 V_2}} \quad \textbf{Eq. 3-42}$$

where β: is the heat flux density distribution coefficient Eq. 3-42 [95]. The value of heat transferred to the gear and the heat transferred to the fluid could be calculated by Eq. 3-43and Eq. 3-44 respectively

$$q_g = \beta_1 \cdot \gamma \cdot q_{gen} \quad \textbf{Eq. 3-43}$$

$$q_p = \beta_2 \cdot \gamma \cdot q_{gen} \quad \textbf{Eq. 3-44}$$

3.2.3.2. Mesh of the gear tooth geometry

This has been utilized to simulate the hear distribution in the gear material. This mesh also used to evaluate the thermal stress and thermal deformation in the tooth of the gear. The mesh has been generated automatically using a PDE solver in MATLAB. Since 2D and 3D simulation have been done, the 2D and the 3D mesh has been generated based on the required simulation. Figure 3-8 shows the 3D and 2D mesh that has used in the simulation.

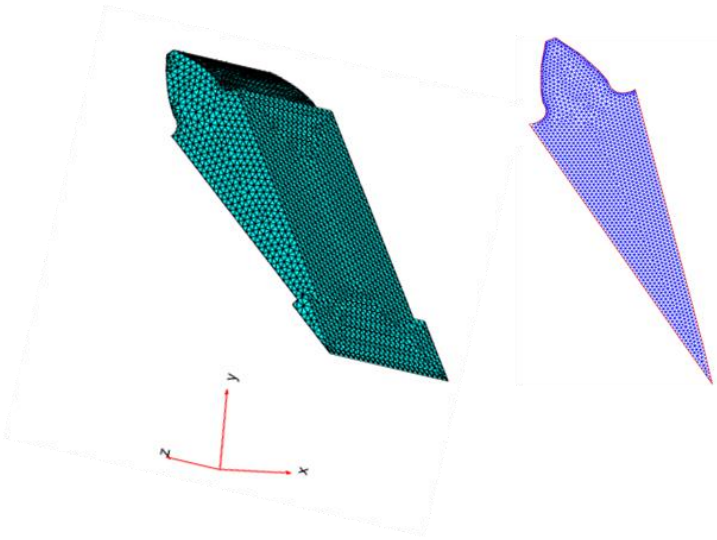

Figure 3-8 3D and 2D mesh for the tooth of the gear

3.2.3.3. Boundary conditions for gear tooth

After determining the amount of heat flux that will enter the gear material, the other boundary conditions should be determined to make the simulation. 2D and 3D simulation have been done for the gear tooth. The boundary conditions for the 2D simulation are shown in the simulation Table.

3.2.3.4. 2D boundary conditions

Each surface of the gear tooth has boundary conditions Figure 3-9 shows the numbers of surfaces on the gear tooth. PDE solver in MATLAB has been used to make the simulation.

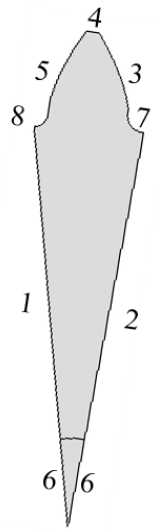

Figure 3-9 Geometry and boundary conditions for 2D gear tooth simulation

Table 3-1 Boundary conditions for the 2D simulation

Edge number	Boundary condition	Formula
1	symmetrical boundary conditions (Zero heat flux is crossing the boundary).	$\frac{\partial T}{\partial n}\|_1 = 0$
2	symmetrical boundary conditions (Zero heat flux is crossing the boundary).	$\frac{\partial T}{\partial n}\|_2 = 0$
3	Forced convection	$-k\frac{\partial T}{\partial n}\|_3 = h_3(T - T_\infty)$
4	Forced convection	$-k\frac{\partial T}{\partial n}\|_4 = h_4(T - T_\infty)$
5	Input heat from the interpolation result	$q = -k\frac{\partial T}{\partial n}\|_5$
6	Constant shaft temperature	$T\|_6 = T_0$
7	Forced convection	$-k\frac{\partial T}{\partial n}\|_7 = h_7(T - T_\infty)$
8	Forced convection	$-k\frac{\partial T}{\partial n}\|_8 = h_8(T - T_\infty)$

3.2.3.5. 3D boundary conditions

The list of boundary conditions for the 3D model is presented in Table 3-2

Table 3-2 Boundary conditions for the 3D simulation

Surface number	Boundary condition	Formula
1	Forced convection	$-k\frac{\partial T}{\partial n}\|_1 = h_1(T - T_\infty)$
2	symmetrical boundary conditions (Zero heat flux is crossing the boundary).	$\frac{\partial T}{\partial n}\|_2 = 0$
3	symmetrical boundary conditions (Zero heat flux is crossing the boundary).	$\frac{\partial T}{\partial n}\|_3 = 0$
4	Forced convection	$-k\frac{\partial T}{\partial n}\|_4 = h_4(T - T_\infty)$
5	Forced convection	$-k\frac{\partial T}{\partial n}\|_5 = h_5(T - T_\infty)$
6	Input heat from the interpolation result	$q = -k\frac{\partial T}{\partial n}\|_6$
7	Constant shaft temperature	$T\|_7 = T_0$
8	Forced convection	$-k\frac{\partial T}{\partial n}\|_8 = h_8(T - T_\infty)$
9	Forced convection	$-k\frac{\partial T}{\partial n}\|_9 = h_9(T - T_\infty)$
10	Forced convection	$-k\frac{\partial T}{\partial n}\|_{10} = h_{10}(T - T_\infty)$
11	Constant shaft temperature	$T\|_{11} = T_0$
12	Forced convection	$-k\frac{\partial T}{\partial n}\|_{12} = h_{12}(T - T_\infty)$
13	Forced convection	$-k\frac{\partial T}{\partial n}\|_{13} = h_{13}(T - T_\infty)$

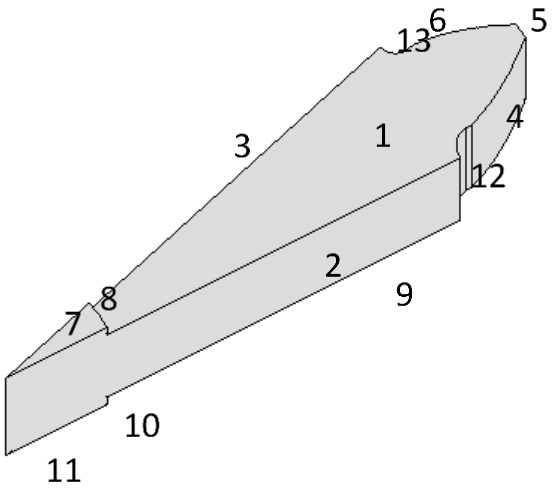

Figure 3-10 Geometry and boundary conditions for 3D gear tooth simulation

3.2.3.6. Values of parameters

The values of temperatures of surfaces, ambient temperature, and the convection heat transfer coefficients are listed below.

The temperature of surfaces number 7 and 10 which is representing the temperature of the shaft is Eq. 3-45.

$$T_7 = T_{11} = 50^{o}C \quad \textbf{Eq. 3-45}$$

The temperature of the surrounding for the gear tooth is $T_\infty = 50^{o}C$. the general formula for the convection coefficient at surface number 1 is in Eq. 3-46 [95].

$$h_1 = Nu \cdot k_{mix}\sqrt{\frac{\omega}{v_{mix}}} \quad \textbf{Eq. 3-46}$$

The convection heat transfer coefficient at surfaces 1 and 9 is shown in Eq. 3-47 if $Re < 2 \times 10^5$ [95].

$$h_1 = h_9 = 0.308 \cdot k_{mix} \cdot (m_h + 2)^{0.5} \cdot Pr_{mix}^{0.5} \cdot \left(\frac{\omega}{v_{mix}}\right)^{0.5} \quad \textbf{Eq. 3-47}$$

If $2 \times 10^5 < Re < 2.5 \times 10\text{^}5$ the convection heat transfer coefficient at surfaces 1 and 9 can be calculated by Eq. 3-48 [95].

$$h_1 = h_9 = 10 \times 10^{-20} \cdot k_{mix} \cdot \left(\frac{\omega}{v_{mix}}\right)^4 \cdot r^7 \quad \textbf{Eq. 3-48}$$

Eq. 3-49 is the convection heat transfer coefficient at surface number 4. Re and Pr are the Reynolds and Prandtl's numbers respectively.

$$h_4 = 0.228 \cdot Re^{0.731} \cdot Pr^{\frac{1}{3}} \cdot \frac{k}{d_i} \quad \textbf{Eq. 3-49}$$

The convection coefficient at surface number 5 is equal to the maximum values for the calculated convection coefficient at surface number 1 as shown in Eq. 3-50 [95].

$$\mathrm{h_5} = \max(\mathrm{h_1}) \quad \textbf{Eq. 3-50}$$

Surface number 8 and surface number 10 have the same formula for the convection coefficient as in Eq. 3-51 [95].

$$h_8{=}h_{10} = 0.0163 \cdot \frac{k_{mix}}{d_{shaft}} \cdot Re^{0.8} \quad \textbf{Eq. 3-51}$$

where k_{mix} is the thermal conductivity for the mixed air with oil and d_{shaft} is the diameter of the shaft.

The heat transfer coefficient for the surfaces 12 and 13 is presented in Eq. 3-52 [95].

$$h_{12}=h_{13} \rightarrow \frac{h_1}{3} \leq h_{12} \leq \frac{h_1}{2}$$ **Eq. 3-52**

3.2.4. Interpolation Methodology

3.2.4.1. 2D interpolation

Interpolation between the results of the fluid film and the mesh of the gear (2D). The finite sliding power loss at each node is calculated by Eq. 3-19. To interpolate the value of sliding power loss to the 2D mesh of the gear the location of the node should be determined first. Figure 3-11 shows the counter of the mesh and the 2D interpolation methodology. This counter gives each node a number based on its location in the X and Y coordinates. Where n is the counter in the X direction, and m is the counter in Y direction. Since the length of the line of action for gear tooth is known, and the gear width is also known, The location of the node could be calculated by Eq. 3-53and Eq. 3-54.

$$\gamma = X \times n$$ **Eq. 3-53**

$$\eta = Y \times m$$ **Eq. 3-54**

where γ and η are the X and Y location for the node respectively. X and Y are the distance between nodes in the X and Y direction respectively.

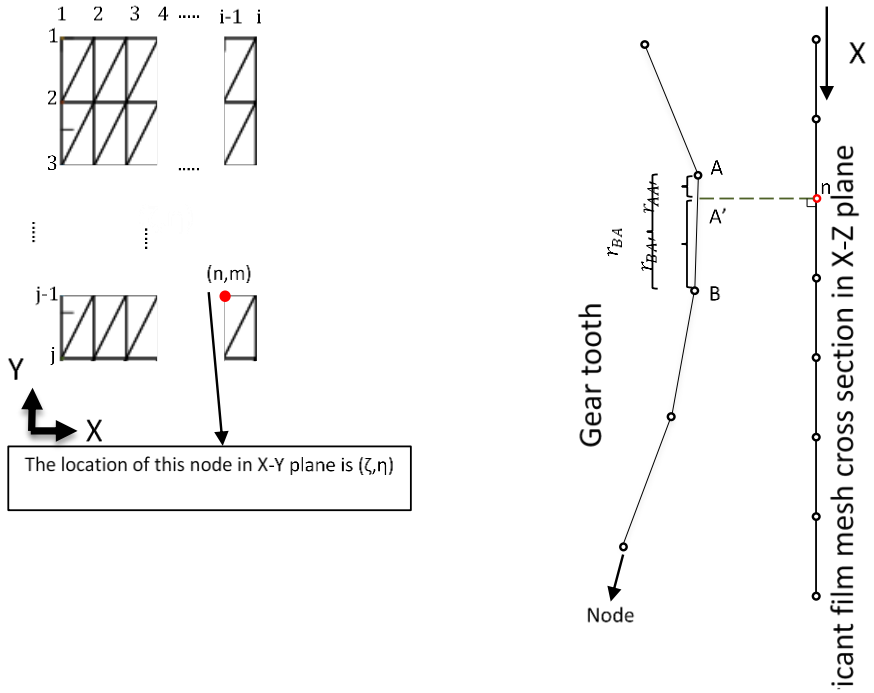

Figure 3-11 2D mesh interpolation

The value of heat inserted for each node of the surface of the gear could be evaluated by the weight function. The weight value for node A and node B could be calculated by Eq. 3-55 and Eq. 3-56 respectively [96].

$$W_A = \frac{(r_{AB} - r_{AA'})}{r_{AB}} \quad \textbf{Eq. 3-55}$$

$$W_B = \frac{(r_{AB} - r_{BA'})}{r_{AB}} \quad \textbf{Eq. 3-56}$$

Based on the value of the wight value the amount of heat for node A and node B evaluated using the formula in Eq. 3-57 and Eq. 3-58 respectively.

$$q_A = W_1 \cdot q_{g|n} \quad \textbf{Eq. 3-57}$$

$$q_B = W_2 \cdot q_{g|n} \quad \textbf{Eq. 3-58}$$

3.2.4.2. 3D interpolation

3D interpolation is more complicated than the 2D interpolation. The reason for that is the complicated projection of the node of the fluid lubricant mesh to the mesh of the surface of the gear in 3D. The methodology of the projection is presented in Figure 3-12. $e_1\ and\ e_2$ are the elements from the mesh of the fluid lubricant. $e_3\ and\ e_4$ are the elements of the mesh of the surface of the gear tooth. Node (n,m) is projected to the point P. The value of the projected point will be distributed to the nodes of the element ($B1, B2$ and $B3$). The value of the heat flux at each node has been calculated using the Barycentric Coordinates method with the wight function [97]. The location of the points $B1, B2$ and $B3$ are assumed to be $(X1, Y1)$, $(X2, Y2)$ and $(X3, Y3)$. The location of the projected point P is $(X4, Y4)$. Based on Barycentric method some constrained should be applied. These constraints are clarified in Eq. 3-59-Eq. 3-62.

$$p_x = \sum_i W_i X_i \quad \textbf{Eq. 3-59}$$

$$p_y = \sum_i W_i Y_i \quad \textbf{Eq. 3-60}$$

$$W_i = \frac{\mathrm{A}_i}{\mathrm{A}} \quad \textbf{Eq. 3-61}$$

$$\sum_i W_i = 1 \quad \textbf{Eq. 3-62}$$

The constraints of the weight function method are formulated in Eq. 3-63-Eq. 3-64Eq. 3-65.

$$X4 = W1 \cdot X1 + W2 \cdot X2 + W3 \cdot X3 \quad \textbf{Eq. 3-63}$$

$$Y4 = W1 \cdot Y1 + W2 \cdot Y2 + W3 \cdot Y3 \quad \textbf{Eq. 3-64}$$

$$W1 + W2 + W3 = 1 \quad \textbf{Eq. 3-65}$$

The three constrained in the above equations from the wight function could be solved for $W1, W2\ and\ W3$ since the locations of all points are known. Evaluating the values of the weight functions for the nodes $B1, B2$, and $B3$ will be used to determine the value of input heat for each node as described in Eq. 3-66, Eq. 3-67 and Eq. 3-68.

$$q_{B1} = W_1 \cdot q_{g|n} \quad \textbf{Eq. 3-66}$$

$$q_{B2} = W_2 \cdot q_{g|n} \quad \textbf{Eq. 3-67}$$

$$q_{B3} = W_3 \cdot q_{g|n} \quad \textbf{Eq. 3-68}$$

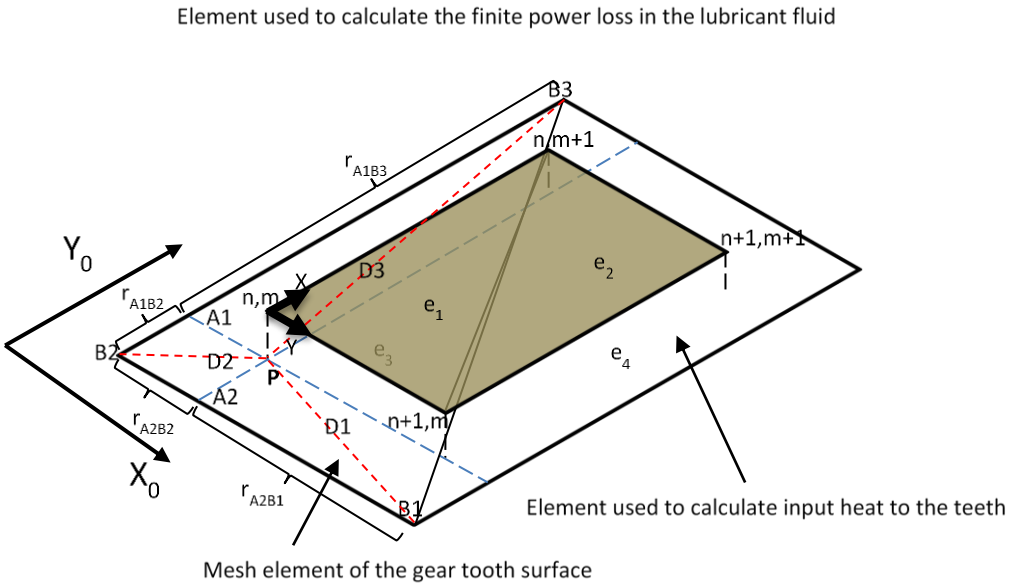

Figure 3-12 3D mesh interpolation

3.2.5. Thermal deformation

The change in the temperature of the gear material from the initial temperature will lead to thermal stress and deformation in the gear body. The thermal stress and deformation can be evaluated using Eq. 3-69 [98].

$$\epsilon^{th} = \int_{T_{ref}}^{T} \alpha(T) dT \qquad \textbf{Eq. 3-69}$$

3.2.6. Thermal stress

Eq. 3-70 is the formula for calculating the thermal stress in the gear body [98]. The reference temperature for the simulation is assigned to be 25°C for both thermal deformation and thermal stress.

$$\sigma_{th} = \epsilon^{th} E \qquad \textbf{Eq. 3-70}$$

The value of the thermal expansion factor is $\alpha = 12 \times 10^{-6} \frac{m}{m \cdot K}$ (Kan).

3.2.7. Contact ratio analysis

The analysis of the contact ratio is important for calculating the normal force and analyzing the sliding power loss in gears.

3.2.7.1. Energy calculation

The potential energy in the gear body can be transformed into three shapes. The shapes are bending, compression, and shear as shown in Eq. 3-71.

$$U_p = U_b + U_c + U_s \qquad \textbf{Eq. 3-71}$$

Where U_b, U_c and U_s are bending, compression, and shear terms, respectively.

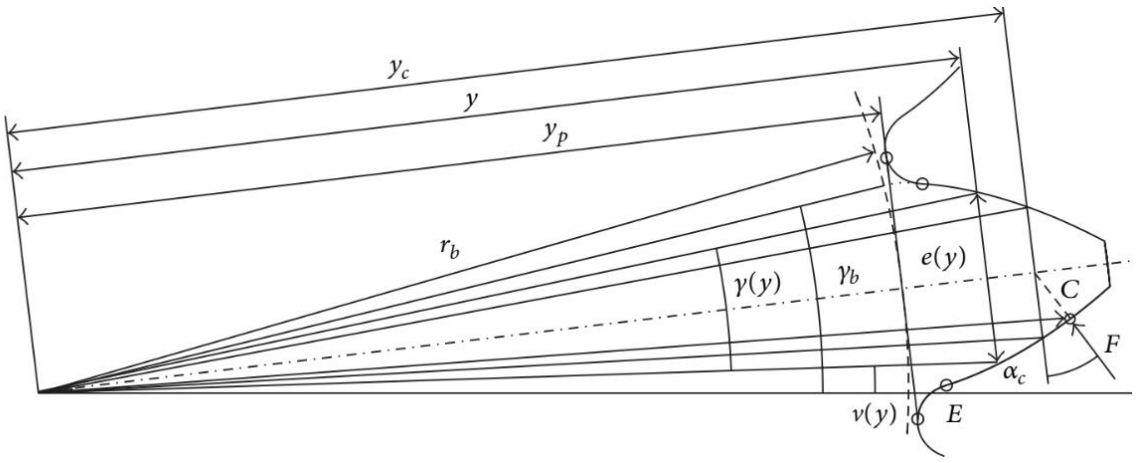

Figure 3-13 Parameters of gear geometry [99]

Based on the theory of elasticity the geometrical parameters in Figure 3-13 the bending, compression, and shear terms can be calculated by Eq. 3-72, Eq. 3-73, and Eq. 3-74 respectively [99].

$$U_b = 6\frac{w^2\cos^2\alpha_c}{Eb}\int_{y_p}^{y_c}\frac{(y_c-y)^2}{e^3(y)}dy \qquad \textbf{Eq. 3-72}$$

$$U_c = 0.5\frac{w^2\sin^2\alpha_c}{Eb}\int_{y_p}^{y_c}\frac{1}{e(y)}dy \qquad \textbf{Eq. 3-73}$$

$$U_s = 0.5\frac{w^2\cos^2\alpha_c}{Gb}\int_{y_p}^{y_c}\frac{1}{e(y)}dy \qquad \textbf{Eq. 3-74}$$

3.2.7.2. Contact point location

The profile of the contact point could be described as a function of the rotating angle, the number of teeth of the gear, the radius of the contact point, and the radius of the base circle as shown in Eq. 3-75.

$$\zeta = \theta \frac{n_p}{2\pi} = \frac{n_p}{2\pi} \sqrt{\frac{r_\zeta^2}{r_b^2} - 1} \quad \textbf{Eq. 3-75}$$

The total potential energy at the contact point equal to the sum of potential energy from the pinion and potential energy from the gear as viewed in Eq. 3-76.

$$U_{point} = U_1 + U_2 = U_{point}(\zeta) \quad \textbf{Eq. 3-76}$$

The unity of potential energy at the contact point can be described as shown in Eq. 3-77. Where b is the width of the gear and ν is the inverse of the unity of potential energy Eq. 3-78.

$$u(\zeta) = \frac{b}{w^2} U_{point}(\zeta) \quad \textbf{Eq. 3-77}$$

$$\nu(\zeta) = \frac{1}{u(\zeta)} \quad \textbf{Eq. 3-78}$$

The previous equations and relations used to conclude the load sharing formula regardless of the gear system is a standard or high contact system as in Eq. 3-79.

$$R_i(\zeta_i) = \frac{w_i(\zeta_i)}{w} = \frac{\nu_i(\zeta_i)}{\sum_{j=0}^{z_1-1} \nu_j(\zeta_j)} = \frac{\nu(\zeta_i)}{\sum_{j=0}^{z_1-1} \nu_j(\zeta_{j+(j-i)})} \quad \textbf{Eq. 3-79}$$

3.2.7.3. Standard contact ratio

For standard contact ratio, the contact ratio ε_α should be between 1 and 2. The final form for the load sharing formula for standard contact is given by Eq. 3-80, Eq. 3-81, and Eq. 3-82.

$$R(\zeta) = \frac{\cos\left[b_o\left(\zeta - \frac{\varepsilon_\alpha}{2}\right)\right]}{\cos\left[b_o\left(\zeta - \frac{\varepsilon_\alpha}{2}\right)\right] + \cos\left[b_o\left(\zeta + 1 - \frac{\varepsilon_\alpha}{2}\right)\right]} \quad for\ 0 \le \zeta \le \varepsilon_\alpha - 1 \qquad \textbf{Eq. 3-80}$$

$$R(\zeta) = 1 \quad for\ \varepsilon_\alpha - 1 \le \zeta \le 1 \qquad \textbf{Eq. 3-81}$$

$$R(\zeta) = \frac{\cos\left[b_o\left(\zeta - \frac{\varepsilon_\alpha}{2}\right)\right]}{\cos\left[b_o\left(\zeta - 1 - \frac{\varepsilon_\alpha}{2}\right)\right] + \cos\left[b_o\left(\zeta - \frac{\varepsilon_\alpha}{2}\right)\right]} \quad for\ 1 \le \zeta \le \varepsilon_\alpha \qquad \textbf{Eq. 3-82}$$

The load sharing formula has a formula if the contact ratio is less than 1, and another formula if the contact ratio is between 1 and 2.

3.2.7.4. High contact ratio equations

Analyzing the high contact ratio will be more complicated than the standard contact. The high contact system has 5 formulas to present load sharing in the gears. The Eq. 3-83 to Eq. 3-87 below have several intervals. Each interval is for specific contact time.

$$R(\zeta) = \left(\cos\left[b_0\left(\zeta - \frac{\varepsilon_\alpha}{2}\right)\right]\right) \times \left(\cos\left[b_0\left(\zeta - \frac{\varepsilon_\alpha}{2}\right)\right] + \cos\left[b_0\left(\zeta + 1 - \frac{\varepsilon_\alpha}{2}\right)\right] + \cos\left[b_0\left(\zeta + 2 - \frac{\varepsilon_\alpha}{2}\right)\right]\right)^{-1} \quad \textbf{Eq. 3-83}$$

$$for\ 0 \le \zeta \le \varepsilon_\alpha - 2$$

$$R(\zeta) = \left(\cos\left[b_0\left(\zeta - \frac{\varepsilon_\alpha}{2}\right)\right]\right) \times \left(\cos\left[b_0\left(\zeta - \frac{\varepsilon_\alpha}{2}\right)\right] + \cos\left[b_0\left(\zeta + 1 - \frac{\varepsilon_\alpha}{2}\right)\right]\right)^{-1} \quad \textbf{Eq. 3-84}$$

$$for\ \varepsilon_\alpha - 2 \le \zeta \le 1$$

$$(\zeta) = \left(\cos\left[b_0\left(\zeta - \frac{\varepsilon_\alpha}{2}\right)\right]\right) \times \left(\cos\left[b_0\left(\zeta - 1 - \frac{\varepsilon_\alpha}{2}\right)\right] + \cos\left[b_0\left(\zeta - \frac{\varepsilon_\alpha}{2}\right)\right] + \cos\left[b_0\left(\zeta + 1 - \frac{\varepsilon_\alpha}{2}\right)\right]\right)^{-1} \quad \textbf{Eq. 3-85}$$

$$for\ 1 \le \zeta \le \varepsilon_\alpha - 1$$

$$R(\zeta) = \left(\cos\left[b_0\left(\zeta - \frac{\varepsilon_\alpha}{2}\right)\right]\right) \times \left(\cos\left[b_0\left(\zeta - 1 - \frac{\varepsilon_\alpha}{2}\right)\right] + \cos\left[b_0\left(\zeta - \frac{\varepsilon_\alpha}{2}\right)\right]\right)^{-1} \quad \textbf{Eq. 3-86}$$

$$for\ \varepsilon_\alpha - 1 \le \zeta \le 2$$

$$R(\zeta) = \left(\cos\left[b_0\left(\zeta - \frac{\varepsilon_\alpha}{2}\right)\right]\right) \times \left(\cos\left[b_0\left(\zeta - 2 - \frac{\varepsilon_\alpha}{2}\right)\right] + \cos\left[b_0\left(\zeta - 1 - \frac{\varepsilon_\alpha}{2}\right)\right] + \cos\left[b_0\left(\zeta - \frac{\varepsilon_\alpha}{2}\right)\right]\right)^{-1} \quad \textbf{Eq. 3-87}$$

$$for\ 2 \le \zeta \le \varepsilon_\alpha$$

A comparison between three solution methods has been used to solve the total problem of the heating in the gear. The solution methods are 1- Analytical solution 2- Finite element

solution 3- Finite difference solution. The flow diagram and the full descriptions of the solution are listed in Figure 3-14.

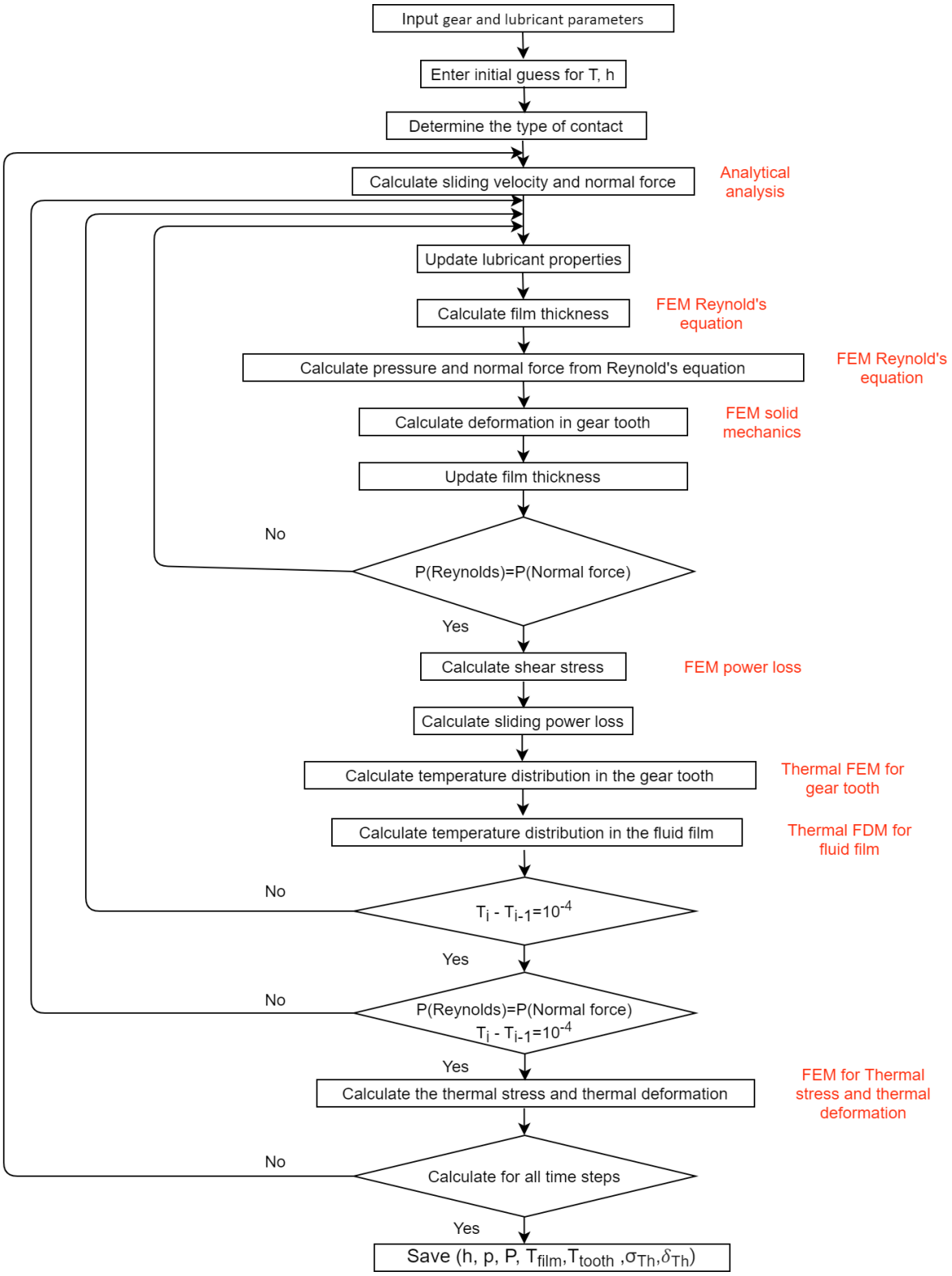

Figure 3-14 Flow diagram of the simulation

3.2.8. Flow diagram models

3.2.8.1. Analytical model

The analytical model has been used to calculate the normal force and sliding velocity along the line of action [100]. The model also used to determine the contact type between the gears (standard contact or high contact).

Bisection method used to solve Reynolds and energy equations. The error was assigned to be 1×10^{-5} for the Reynolds and energy equations. For the Reynolds equation, about 28 iterations were enough to reach the convergence.

3.2.8.2. Finite element models.

1- FEM of Reynolds equation

2D finite element model has been used to calculate the film thickness along the line of action. Figure 3-4 shows an explanation for the gear geometry and the mesh of the simulation. Three nodes triangular mesh has been used to make the simulation. Reynolds equation applied at each node.

2- FEM of solid mechanics

The FEM of solid mechanics used the same mesh used in the Reynolds model. The results of the Reynolds for pressure used to calculate the deflection. The results of the FEM solid mechanics model depend on the material properties of the gear and the magnitude of the pressure at the gear tooth.

3- FEM of the power loss

The FEM of sliding power loss applied to calculate the sliding power loss along the line of action. The profile of the sliding power loss changes along the line of action. The magnitude of power loss calculated based on the shear between the fluid layers of the lubricating fluid and the relative sliding velocity between pinion and gear teeth.

4- Thermal FEM

Thermal analysis for the gear system is very important to calculate the new properties of the fluid with pressure and pressure-dependent viscosity fluid. The temperature has a significant effect on the viscosity of the fluid. Figure 3-8 shows the mesh has been used for this analysis. The boundary conditions for the thermal model used the results of the power model as the input heat. The conviction heat transfer coefficient depends on the rotating speed and the properties of the surrounded fluid.

3.2.8.3. Finite difference model

5- Thermal FDM for the fluid

The finite difference method with the upwind scheme has been used to solve the energy equation for the fluid film at the contact point as described in sections 3.2.2.12. and 3.2.2.13. The solution has been used to update the properties of the lubricant.

The summary of the solution steps for the simulation is shown in the diagram in Figure 3-15.

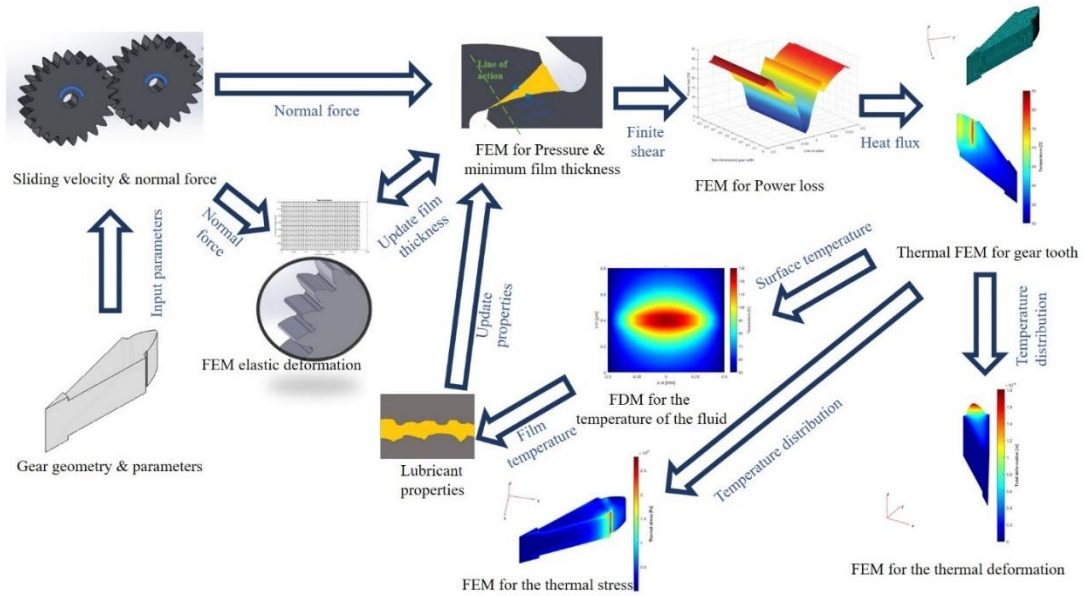

Figure 3-15 Simulation steps and methodology

3.2.9. The input parameters for the case study

For the case study, the properties of the lubricating fluid, the properties of the gear material, the geometry of the gear, and the operating condition should be specified. The properties of the lubricating fluid are listed in Table 3-3.

Table 3-3 Properties of the fluid lubricant

Property	Value
Viscosity	0.04 Pa.s (@30ºC)
Density	920 kg/m3
Thermal conductivity	0.137 W/m.K
Specific heat	2100 J/kg.K

Table 3-4 shows the properties of the material of the gear. These properties are important to simulate the temperature distribution, thermal deformation, thermal stress, and elastic deformation in the gear.

Table 3-4 properties of the material of the gear

Property	**Value**
Modulus of elasticity	200 GPa
Specific heat	530 J/kg.K
Poisson ratio	0.3
Thermal conductivity	37 W/m.K
Density	7800 kg/m3
Coefficient of thermal expansion	12.2×10^{-6} m/(m. K)

The operating parameters like rotating speed and input torque in addition to the properties of the geometry of the gear like the number of teeth and pressure angle are arranged in Table 3-5.

Table 3-5 Parameters of the geometry and the operating conditions of the simulation

Parameter	Value
Number of teeth for gear	24
Number of teeth for pinion	32
Pressure angle	20^o
Module	4 mm
Tooth width	40 mm
Rotating speed	800 rpm
Input torque	250 N.m
Material	I 9310 Steel
Gear reference temperature	25^oC
Lubricate initial temperature	50^oC

3.3. Results

3.3.1. Sliding velocity

The variation of sliding velocity along the line of action presented in Figure 3-16. The figure shows that the maximum sliding velocity occurs at the beginning of contact and the end of the contact. The sliding velocity at the pitch point is zero. As the rotating speed increases the sliding velocity will increase. Also, some gear geometry parameters affecting the sliding velocity along the line of action.

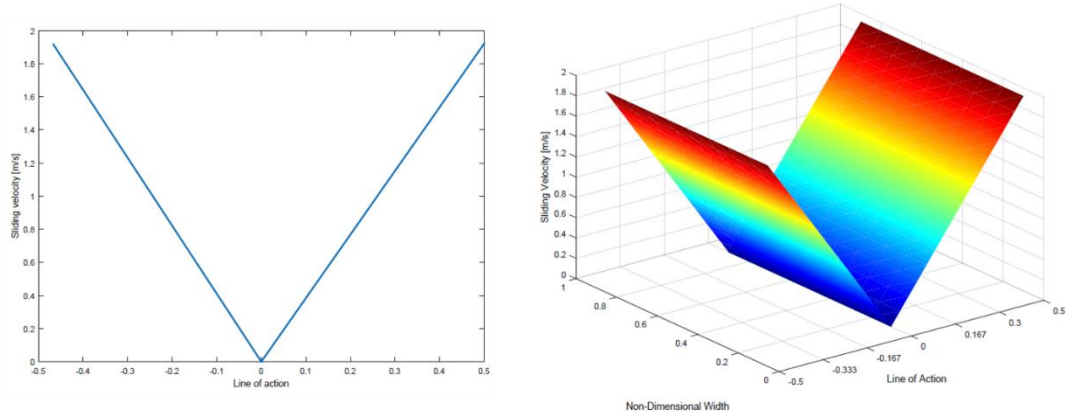

Figure 3-16 2D and 3D sliding velocity along the line of action

3.3.2. Normal force

The change of the normal force along the line of action for the standard contact ratio is shown in Figure 3-17. The figure shows a 2D and 3D plot for the normal force. The variation in the normal force is due to the change of sharing the load by the teeth during the rotation of the gear. The region of single contact has the maximum normal force on the tooth. In single contact, the tooth of the gear will take all the pressure from the input torque. During the first period of the line of action, the normal force starts increasing because the tooth stars sharing the load with the previous tooth. But in the last region, the normal force decreases because the pressure releases from the tooth to the next tooth in the gear.

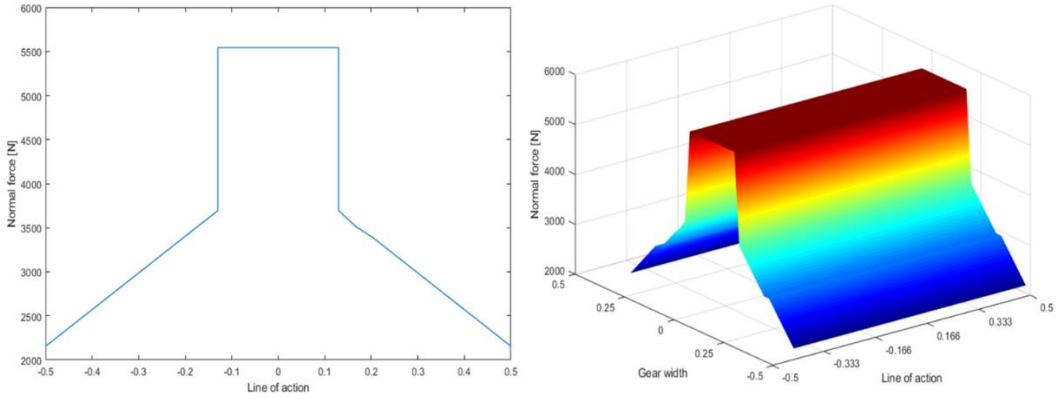

Figure 3-17 2D and 3D Normal force along the line of action

3.3.3. Film thickness

Solving the Reynolds equation will give the value of the rigid film thickness at (h_o) each time step. The film thickness will be updated by including the elastic deformation term. After updating the solution of the film thickness the condition of load balance should be still satisfied as shown in the flow diagram. The code will make double-check on the satisfaction of the load balance condition before and after updating the solution. Figure 3-18 views the solution for the film thickness. The behavior of the film thickness graph is a response to the change in the normal load on the tooth. When the normal force increases on the tooth the film thickness decreases and vice versa. This is the reason for the minimum constant film thickness between the range (-0.13 to 0.19) in the line of action.

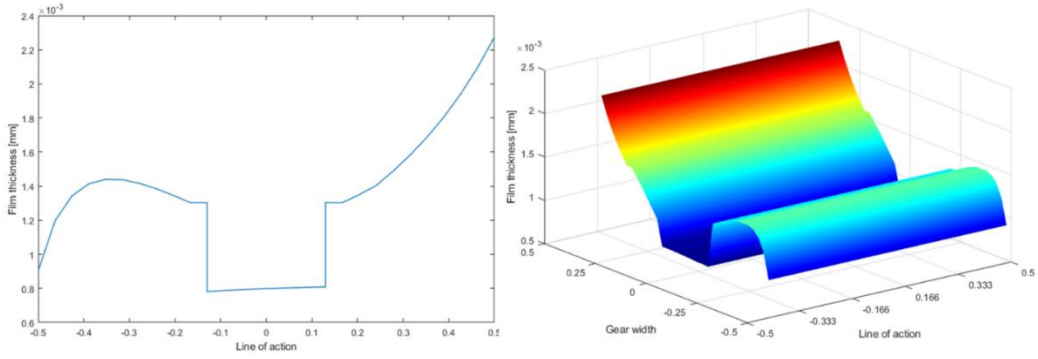

Figure 3-18 2D and 3D film thickness along the line of action

This solution for the film thickness is based on a very smooth surface finish because the minimum film thickness is very small.

3.3.4. Sliding power loss

The results of the integration for the shears tress and sliding velocity over the element area is presented in Figure 3-19. The figure shows the fluctuation of the sliding power loss along the line of contact. The value of the sliding power loss has been calculated at each time step. The fluctuation in the sliding velocity happens due to the change of sliding velocity, normal force, and shear stress along the line of action.

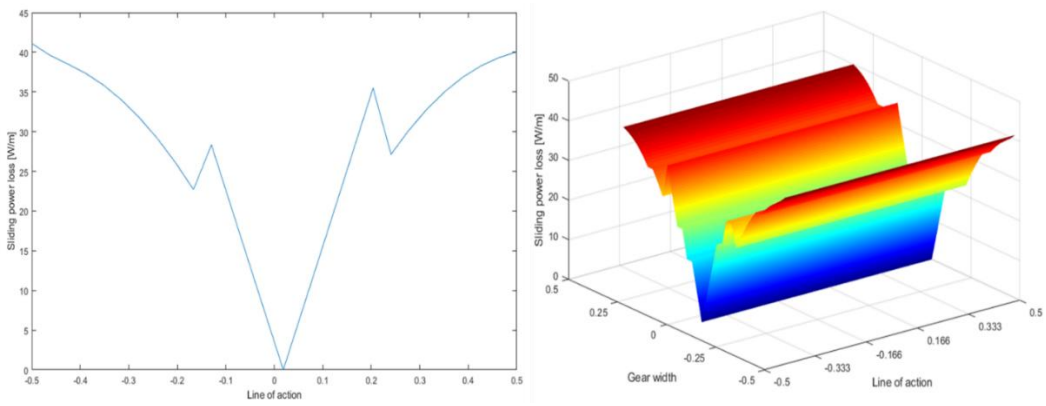

Figure 3-19 2D and 3D sliding power loss along the line of action

3.3.5. Energy equation solution

The energy equation for the fluid film at the point of contact has been described previously. The solution for the FDM for the energy equation is presented in Figure 3-20. The solution includes the propagation of heat in the fluid film each time step. The solution also includes the steady-state solution for the energy equation. The solution done by assuming the contact point length is 1 mm. The transient simulation time step was 1×10^{-5} second. The solution below is at the hottest point on the gear tooth. At first steps, some heat transferred from the tooth to the fluid film. The initial temperature of the fluid is assumed to be $50℃$. This assumption for temperature based on jet oil lubrication. The temperature of the source of the oil is the initial condition for temperature. The jet is assumed to wash all the oil after contact between the teeth. So, the oil will have the same initial temperature at each gear rotation.

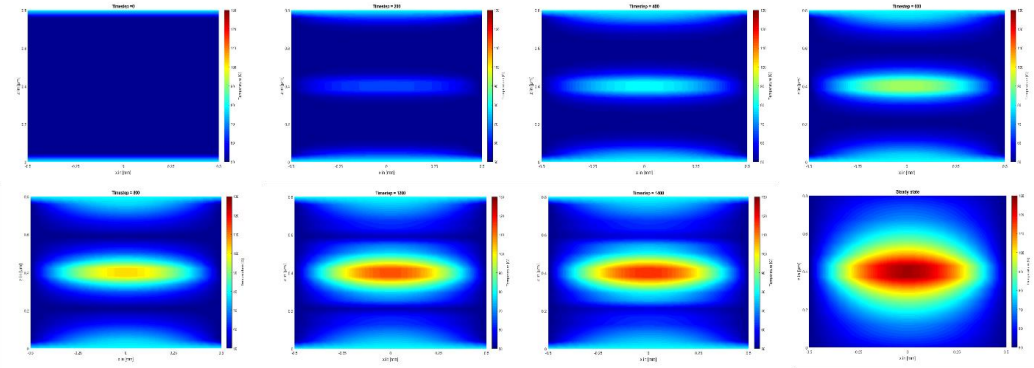

Figure 3-20 Temperature propagation in the fluid film with time at the hottest spot

3.3.6. Validation of FEM

The code has been validated with experimental results done by Chang et al [101] as shown in Figure 3-21 and Figure 3-22. This source has been chosen for validation because the research proposed an experiment at different speeds and different input torques. The experiment has been validated with three models. The first model is 3D EHL without considering the thermal effect. In this model the temperature model of the tooth is 3D, but the effect of temperature of the oil on viscosity was neglected. The second model is 2D TEHL. In this model, a 2D finite element model has been used to simulate the temperature distribution, and the effect of temperature on the viscosity of the oil was considered. The last validation is done with 3D TEHL validation. The 3D TEHL shows the most accurate performance comparing with the experimental results. The accuracy of the 3D TEHL model comes from considering most of the parameters that affect the solution of the simulation that not considered in the previous two methods. The results show that increasing the rotating speed and the input torque will increase the peak temperature of the tooth. This behavior is also compatible with the parametric study that will be shown later.

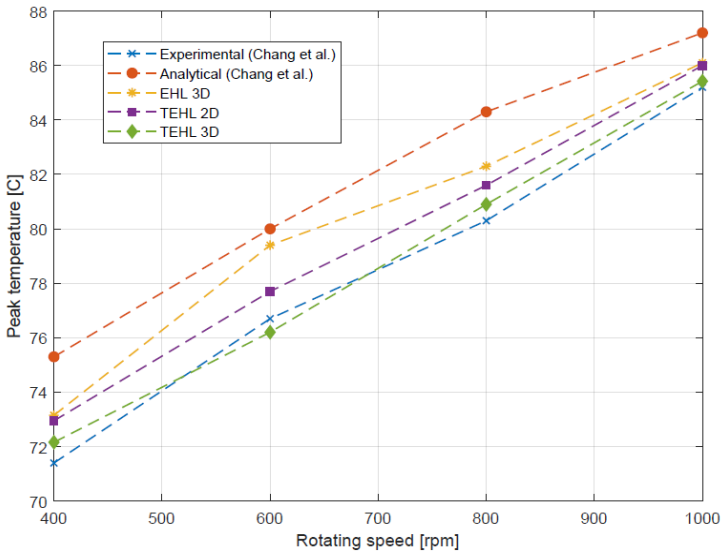

Figure 3-21 Comparison between the simulation and experiment with different rotating speed

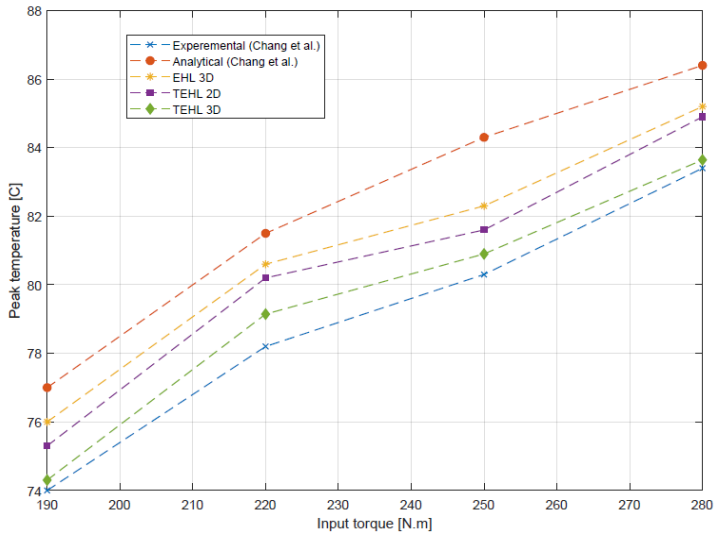

Figure 3-22: Comparison between the simulation and experiment with different input torque

3.3.7. Parametric study for standard contact gears model

A parametric study has been simulated to determine the effect of different parameters. This study will help in selecting the parameters for the prediction models.

Figure 3-23 and Figure 3-24 show the results of the parametric study. The parametric study has been done to determine the effect of input torque and rotating speed on the sliding power loss along the line of action. The study shows that the sliding power loss is proportional to the input torque and sliding velocity. The reason behind the increase of sliding power loss with the input torque is the increase of the normal force on the gear tooth and the reduction of the film thickness along the line of action. The sliding power loss increases with the rotating speed because of the sliding velocity between gears teeth increases. And the shear stress in fluid layers is directly affected by the sliding velocity.

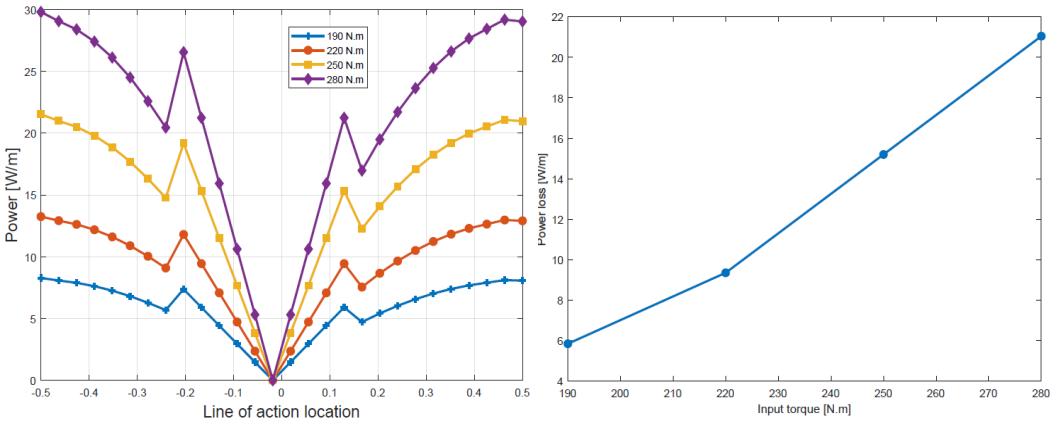

Figure 3-23: The effect of input torque on sliding power loss

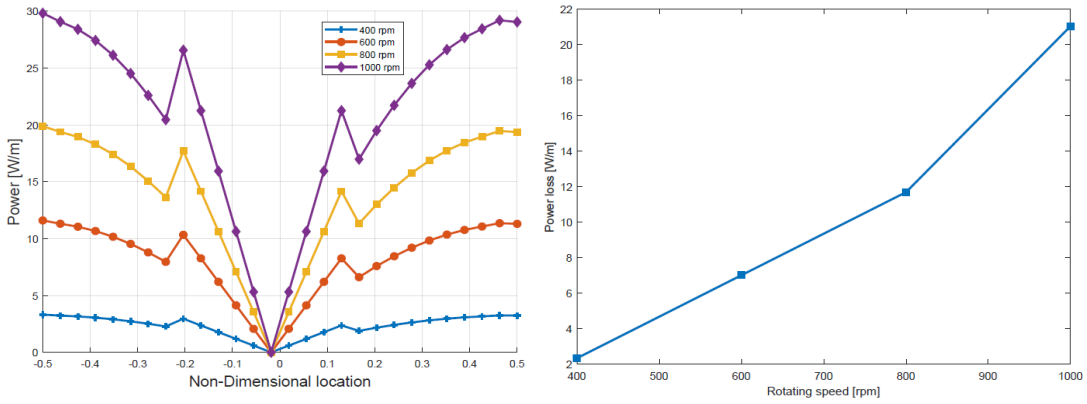

Figure 3-24: The effect of rotating speed on sliding power loss

The viscosity of the fluid changes with its temperature and pressure. Non-constant viscosity approach has been used in the simulation. The viscosity is a strong function with temperature and weak function with pressure. The effect of the lubricant temperature shown in Figure 3-25 and Figure 3-26. Figure 3-25shows the variation of the sliding power loss with lubricant temperature. Also, Figure 3-26shows the influence of lubricant temperature on the minimum film thickness along the line of action. The study shows that the minimum film thickness decreases with the increase of lubricant temperature. This decrease happed due to the decrease of the lubricant viscosity with temperature.

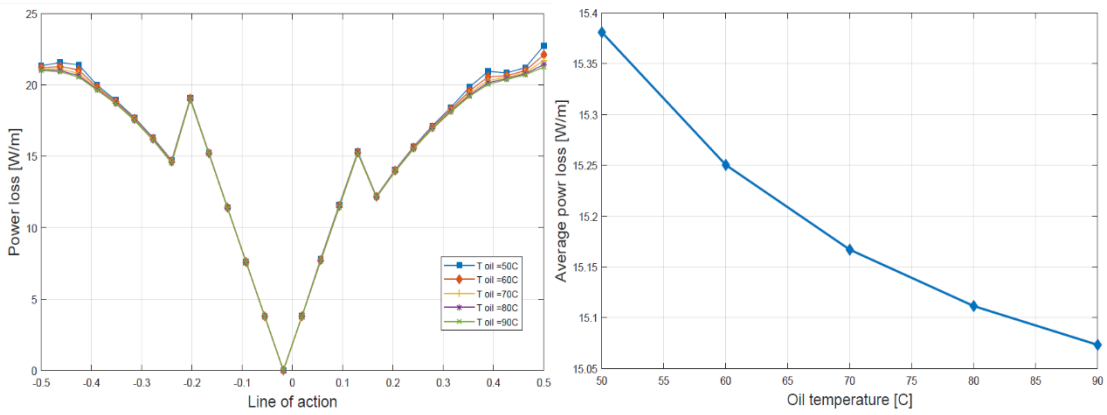

Figure 3-25: The effect of lubricant temperature on sliding power loss along the line of action

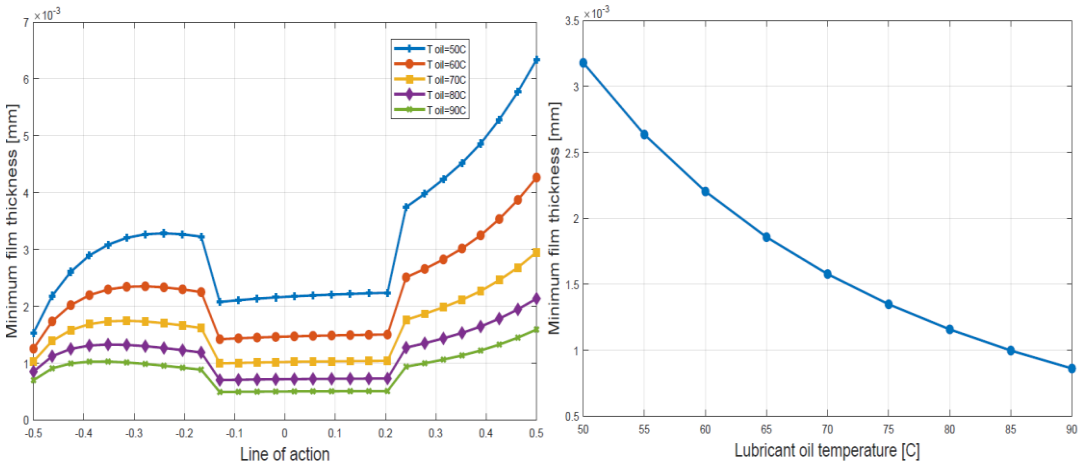

Figure 3-26: The effect of lubricant temperature on minimum film thickness along the line of action

3.3.8. Standard contact ratio vs High contact ratio

The analysis for high contact ratio gears is different from the standard contact as shown before. The values of normal force, film thickness, Hertzian pressure, and sliding power loss will be different between the standard contact and high contact.

Figure 3-27, Figure 3-29, Figure 3-31, and Figure 3-33 show The comparison between standard contact and high contact gear in terms of normal force, Hertzian pressure, film thickness, and sliding power loss for single tooth respectively.

3.3.8.1. Normal force

The value of the normal force in the high contact system is less than the standard contact system for the same input torque. The reason for the less normal force in high contact is because there are more teeth are sharing the load in high contact (2 or 3 teeth), on the other hand in standard contact (1 or 2 teeth) are sharing the load.

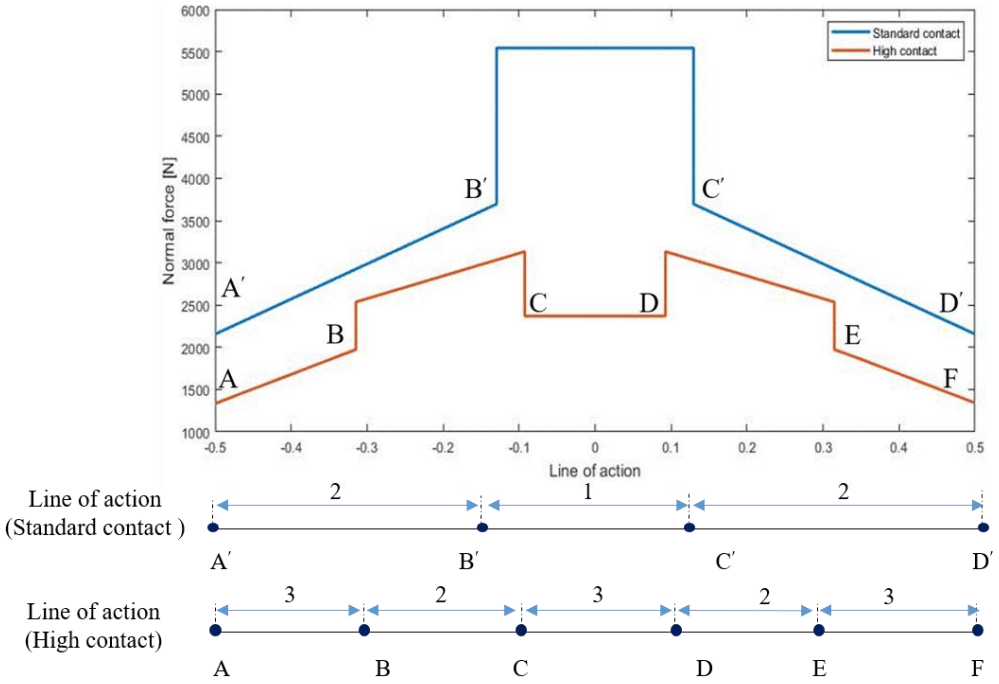

Figure 3-27: Normal force distribution for single tooth along the line of action for standard contact and high contact gears

The comparison between 3D normal force in standard contact and high contact viewed in Figure 3-28. All the axes of the line of action and gear width in the 3D plots have been nondimensionalized for simplicity in presenting.

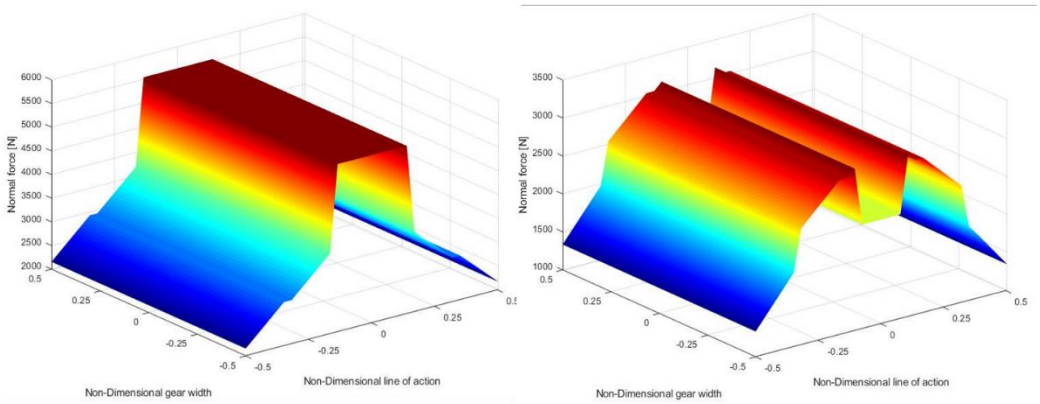

Figure 3-28 3D normal force for standard contact and high contact systems along the line of action

3.3.8.2. Hertzian pressure

The magnitude of the Hertzian pressure on the gear tooth surface depends on the value of the normal force. Since the normal force on the tooth surface in the Standard Contact Ratio (SCR) gears is higher than the normal force in the High Contact Ratio (HCR) gears, the Hertzian pressure in the SCR gears will be higher than the Hertzian pressure in the HCR.

The 2D and 3D plots of the Hertzian pressure are shown in Figure 3-29 and Figure 3-30 respectively.

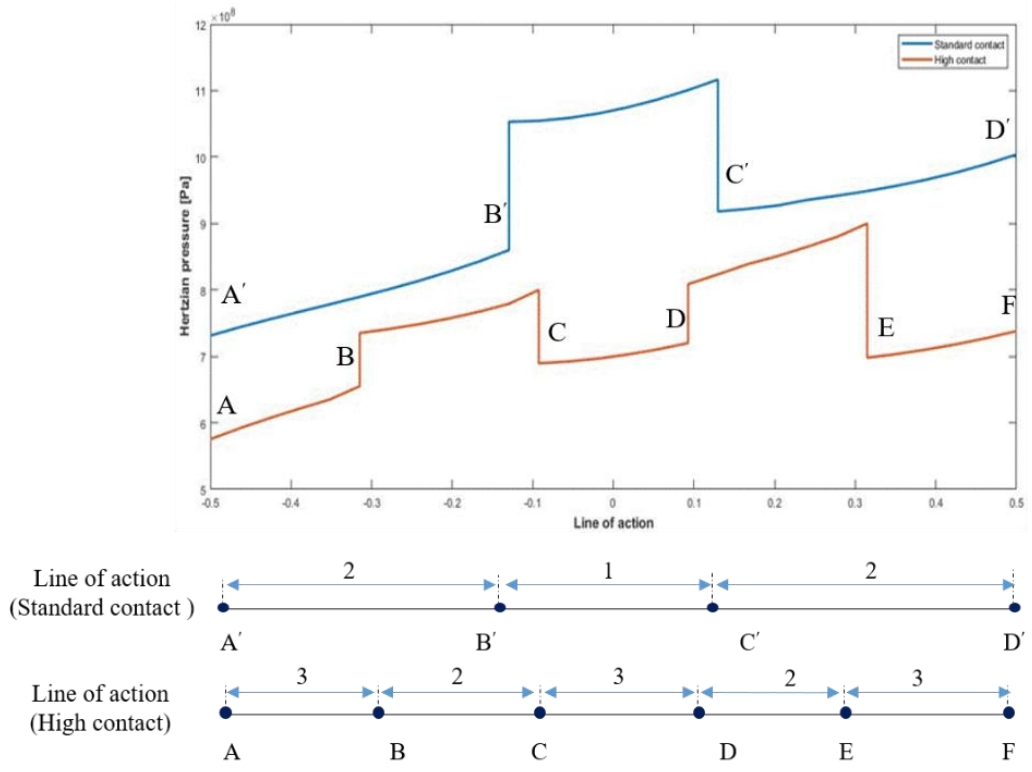

Figure 3-29: Hertzian pressure distribution for a single tooth along the line of action for standard contact and high contact gears

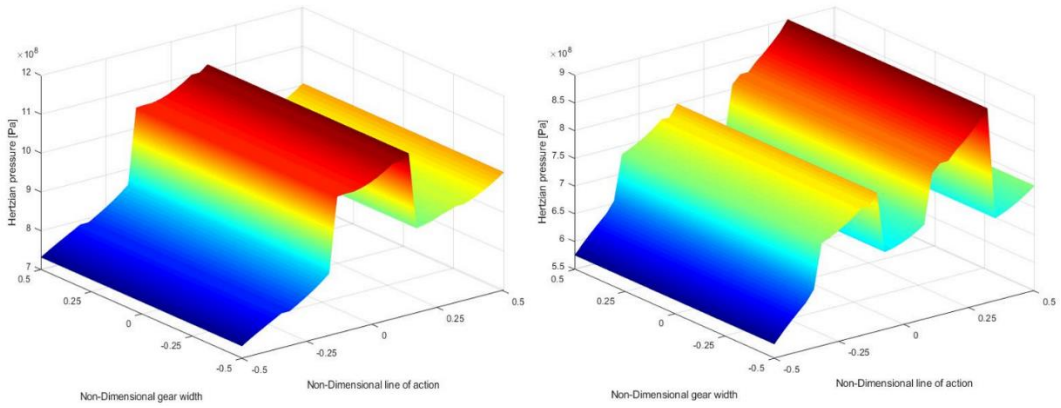

Figure 3-30 3D Hertzian pressure for standard contact and high contact systems along the line of action

The type of loading in gears (Heavily loaded, normally loaded, or lightly loaded) depends on the ratio between the designed shared load and the actual load. The system could be considered as heavily loaded if the tooth carries 1.5-2 times of the designed shared load, normally loaded if it carries 1-1.5 of the designed shared load and lightly loaded if it carries less than 1 of the designed shared load [19]. The Hertzian pressure in the case study was changing from $0.72\ GPa - 1.29\ GPa$ for the Standard Contact Ratio (SCR) and from $0.58\ GPa - 0.89\ GPa$ for the High Contact Ratio (HCR). For example, if the designed shared load for the gear is $0.85\ GPa$, the case study of the SCR system will be considered as a heavily loaded system but it will be normally loaded for the HCR case. **Table 3-6 The ranges of the designed shared pressure for the gear system types**. Table 3-3 the ranges of the designed shared load for each loading type for SCR and HCR systems.

Table 3-6 The ranges of the designed shared pressure for the gear system types

Contact type	Actual load [GPa]	Designed pressure for heavily loaded gears [GPa]	Designed pressure for normally loaded gears [GPa]	Designed pressure for lightly loaded gears [GPa]
Standard contact ratio gear (SCR)	0.72-1.29	P <0.86	0.86-1.29	P >1.29
High contact ratio gear (HCR)	0.58-0.89	P <0.594	0.594-0.89	P >0.89

3.3.8.3. Film thickness

The variation of the normal force along the line of action is affected by the film thickness. The film thickness in the standard contact system is less than the high contact

system is because the normal force is higher in the standard contact gears. The results of the comparison between the standard contact ratio gears and high contact ratio gears in terms of the film thickness are shown in Figure 3-31 and Figure 3-32.

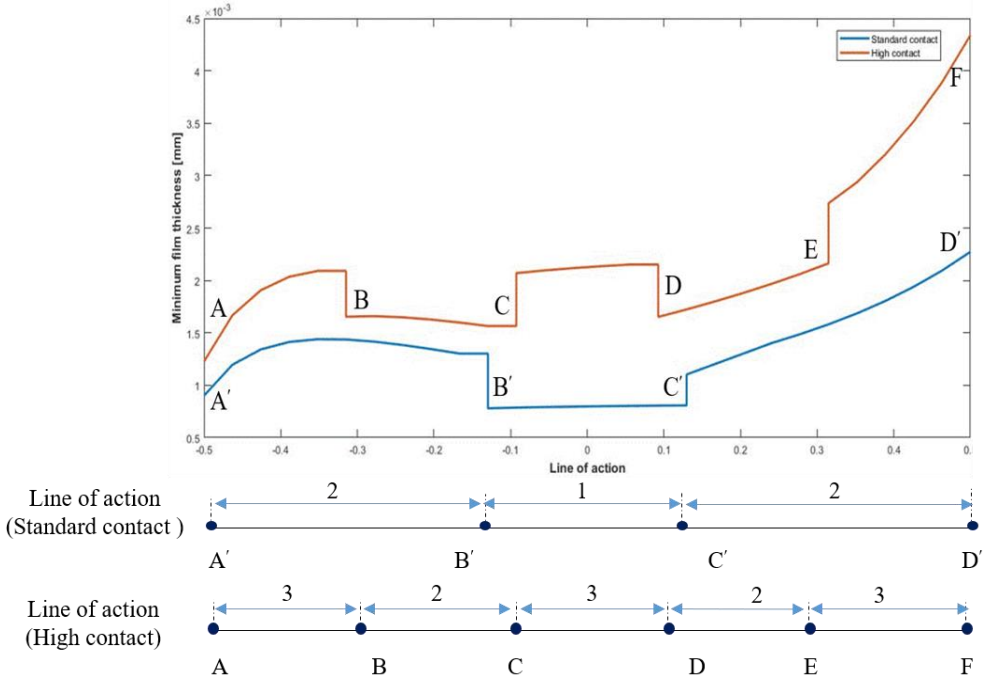

Figure 3-31: Film thickness distribution for a single tooth along the line of action for standard contact and high contact gears

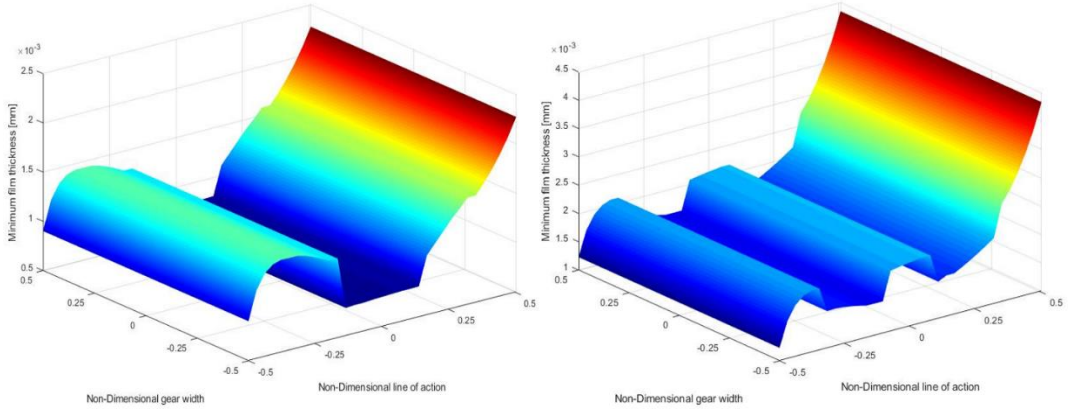

Figure 3-32 3D minimum film thickness for standard contact and high contact systems along the line of action

3.3.8.4. Sliding power loss

Figure 3-33 comparing the sliding power loss for a single tooth for standard contact and high contact system. The results show that for the same operating conditions the power loss for a single tooth for standard contact is higher than the high contact.

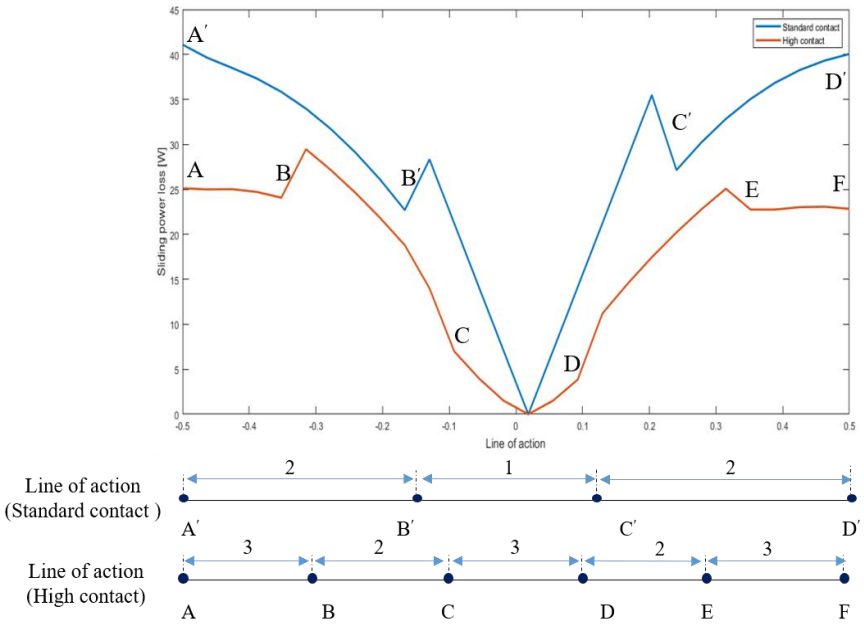

Figure 3-33: Sliding power distribution for a single tooth along the line of action for standard contact and high contact gears

3D plot for the sliding power loss per tooth for standard contact and high contact system viewed in Figure 3-34.

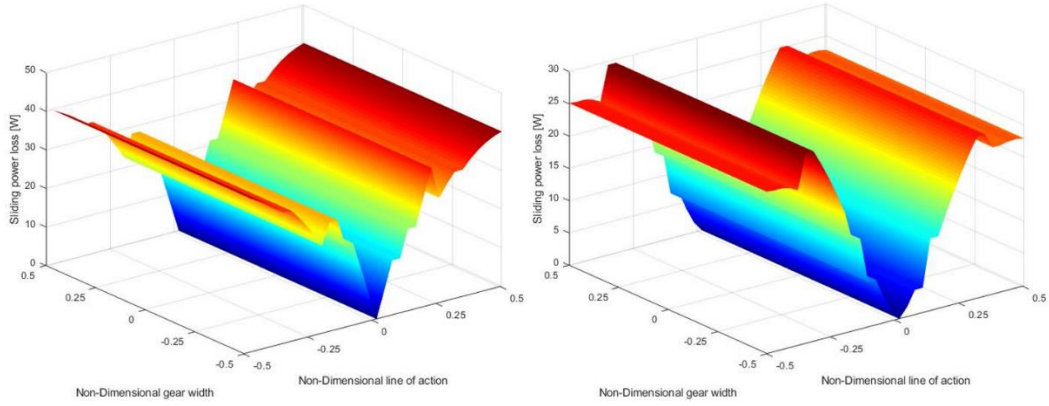

Figure 3-34 3D sliding power loss for standard contact and high contact systems along the line of action

If the sliding power loss for a single tooth in single contact gears is higher than the high contact, does not mean the total sliding power loss in standard contact is higher than high contact. To compare the total power loss between the standard contact and high contact gears, the sum has been taken for the sliding power loss for all the teeth in contact. Figure 3-35 shows the results for total sliding power loss with average and RMS. The results show that the fluctuation in the standard contact graph is more than the high contact graph. In standard contact at the pitch point, the gear will have one tooth in contact with zero sliding velocity. That leads to a zero value for the sliding power loss and high fluctuation in the power loss in the standard contact system.

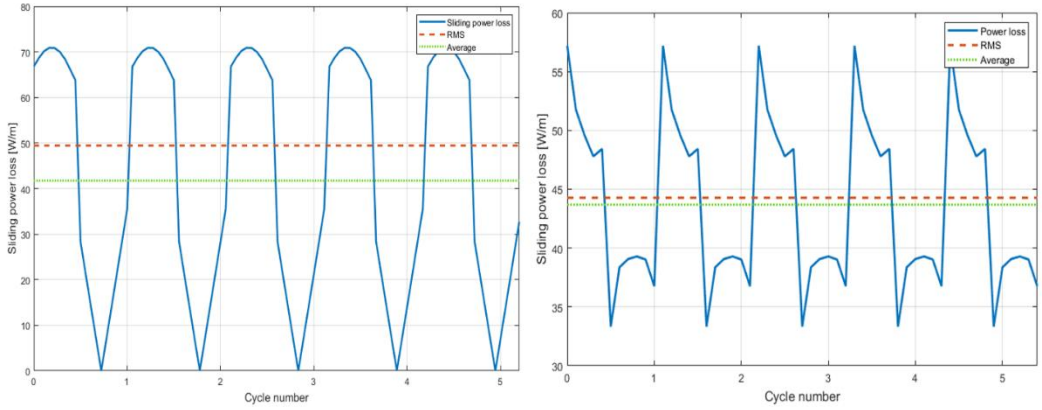

Figure 3-35 2D Total sliding power loss for standard contact and high contact systems.

The 3D plot for the total sliding power loss for standard and high contact are shown in Figure 3-36.

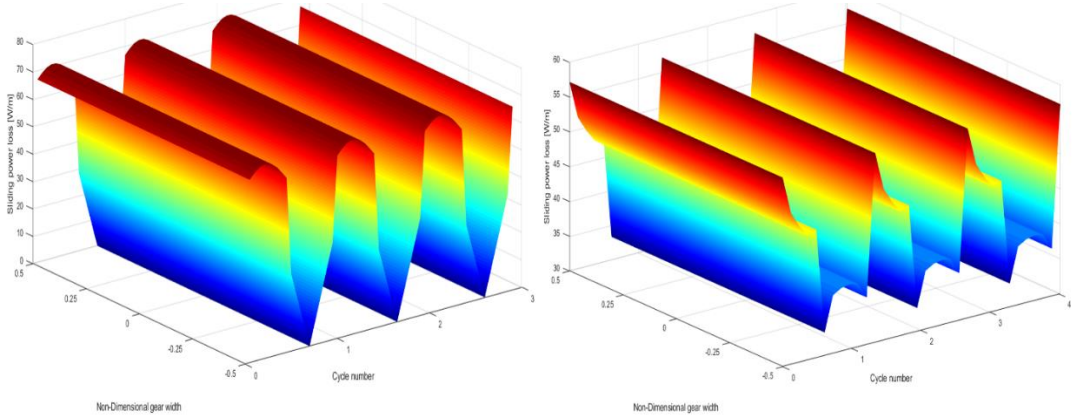

Figure 3-36 Total sliding power loss for standard contact and high contact systems.

3.3.9. Parametric study for high contact ratio gears model

Changing the operating conditions and gear parameters leads to a change in the sliding power loss in the standard contact system. The same parametric study has been done to evaluate the effect of different parameters on the sliding power loss in high contact system.

Figure 3-37 (a)views the results for the parametric study for sliding power loss at different rotating speeds for high contact system. Figure 3-37 (b) shows the average and RMS for the sliding power loss for different speeds.

The results show that the sliding power loss is directly proportional to the sliding velocity. Increasing the rotating speed will increase the sliding velocity between gears' teeth. From the above analysis for sliding power loss, the sliding velocity is an important term in calculating the sliding power loss.

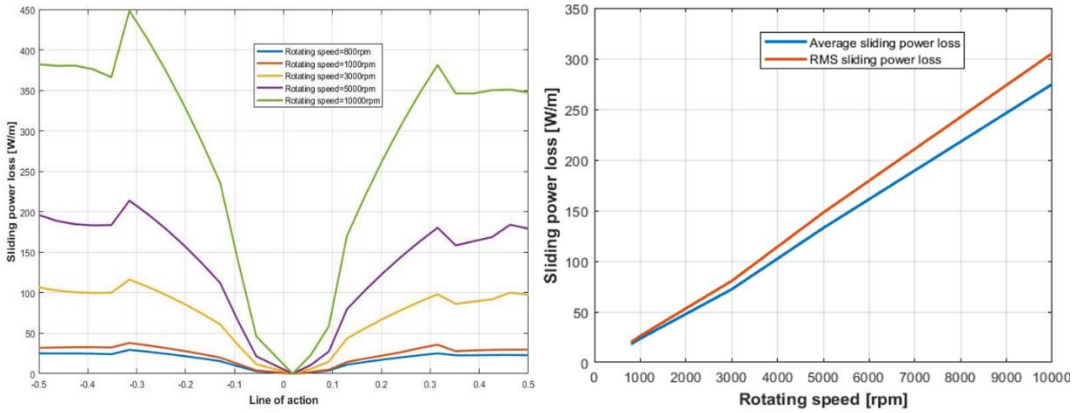

Figure 3-37 The effect of rotating speed on the sliding power loss along the line of action for high contact gears

The effect of the input torque on the sliding power loss presented in Figure 3-38. Increasing the input torque will increase the normal force at the contact point between the gears. This increase in the normal force will raise the value of sliding power loss between the teeth. The results also show the increase of average and RMS of sliding power loss with the input torque.

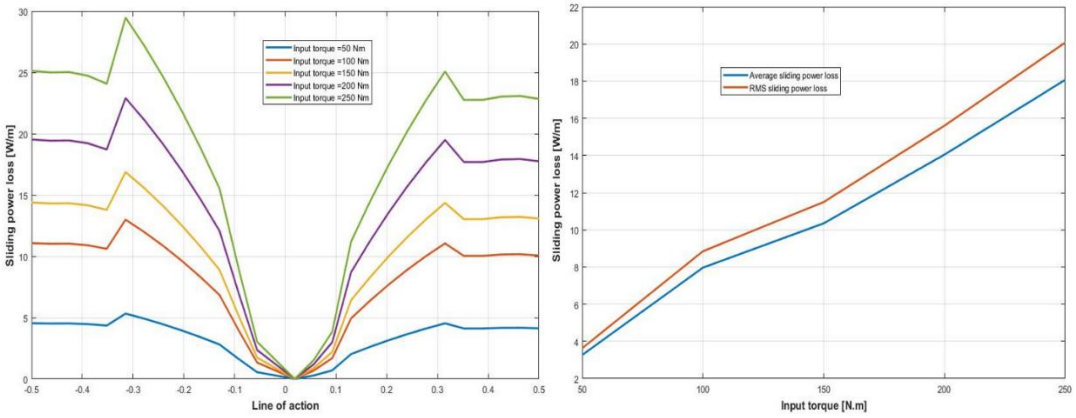

Figure 3-38 The effect of input torque on the sliding power loss along the line of action for high contact gears

The results of the parametric study for the standard contact and high contact are compatible. Where in both systems the results show an increase in the sliding power loss with the rotating speed of the gears and the load torque of the gears.

An additional parametric study has been done for the effect of the diameter of gear's base circle, gear's module, and the viscosity of the fluid on the average sliding power loss. The results of the parametric study are shown in Figure 3-39, Figure 3-40, and Figure 3-41 respectively.

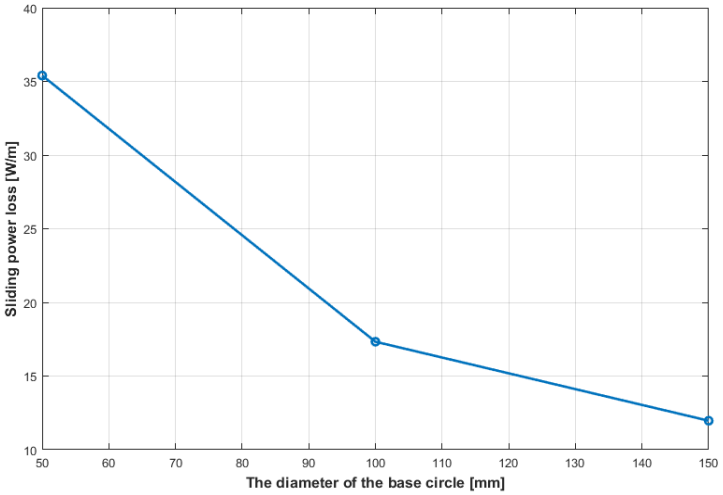

Figure 3-39 The effect of the base diameter of the gear on the average sliding power loss for high contact gear

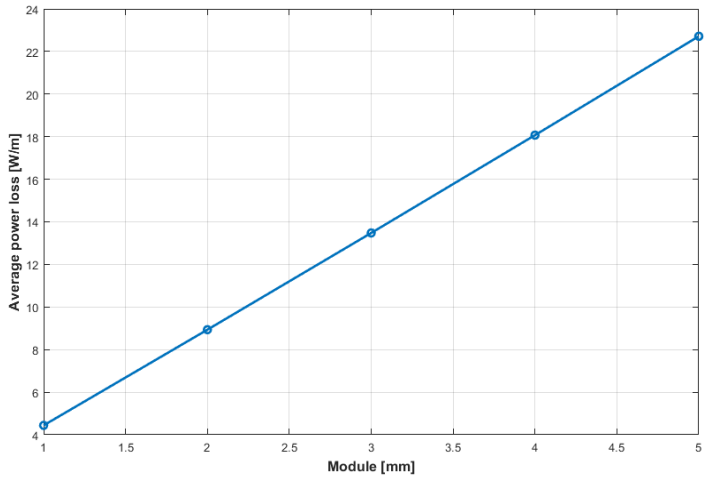

Figure 3-40 The effect of the module of the gear on the average sliding power loss for high contact gear

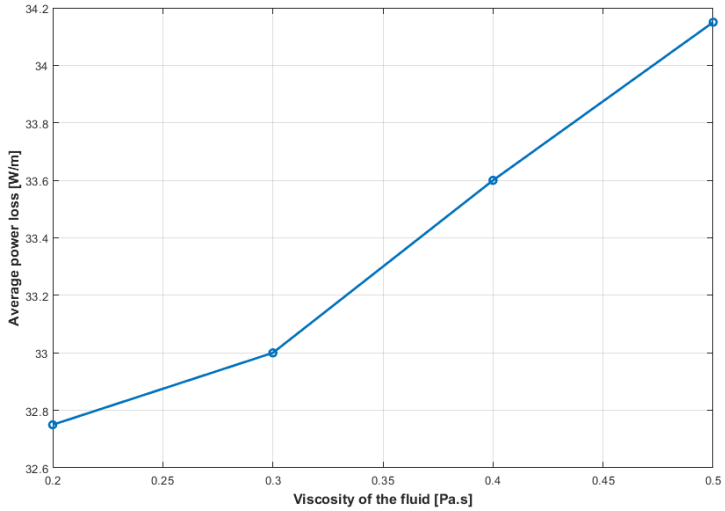

Figure 3-41 The effect of the viscosity of lubricating fluid of the gear on the average sliding power loss for high contact gear

The results of the parametric study concluded that the average sliding power loss is proportional to the module of the gears and the viscosity of the lubricant. On the other

hand, the average sliding power loss is inversely proportional to the diameter of the base circle of the gear.

3.3.10. Thermal distribution

The sliding power loss represents the source of the heat that propagates in the gear material. Based on the sliding power loss analysis, the sliding power loss in standard contact is different from the sliding power loss in high contact. That means the heat source in for the standard contact is different than the heat source in high contact. This difference will lead to a different temperature distribution in tooth material. MATLAB PDE solver has been used to simulate the temperature distribution in the gear tooth.

3.3.10.1. Thermal distribution 2D vs 3D

MATLAB PDE solver used to analyze the distribution in the tooth in two ways. The solver simulated a 2D and 3D temperature in the tooth. Figure 3-42shows the results for 2D and 3D temperature distribution in the tooth for standard contact gear.

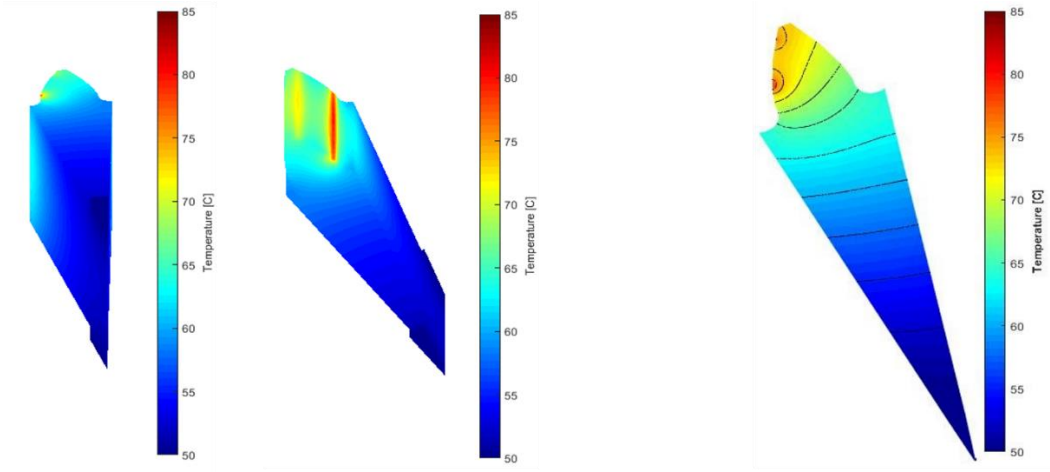

Figure 3-42 3D and 2D temperature distribution in the tooth of the gear

The validation shows that the accuracy of the 3D model is more than the 2D model. The explanation for that is considering the heat convection term in all surfaces in the 3D model but in the 2D model, the convection term did not consider on some surfaces.

3.3.10.2. Thermal distribution standard contact vs high contact

Figure 3-43 shows the difference in temperature distribution in standard contact and high contact. This change in temperature comes from the difference in the amount of sliding power loss per tooth. Reducing the sliding power loss between the teeth will reduce the peak temperature of the tooth because it is the main source of heat. The location of hot spots on the tooth also different between the standard contact and high contact gear because the profile of sliding power loss is different between the two systems.

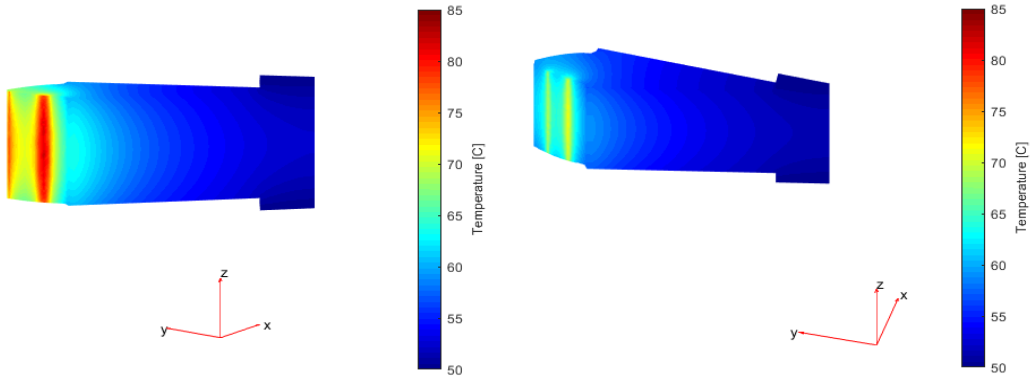

Figure 3-43: a) Temperature distribution for standard contact gear b) Temperature distribution for high contact gear

3.3.11. Parametric study for peak temperature

Many factors may influence the peak temperature of the tooth in addition to the input heat flux from sliding power loss. A parametric study for the effect of boundary conditions (ambient temperature and the temperature of the shaft) has been proposed. The results of the effect of ambient temperature and the temperature of the shaft are shown in Figure 3-44 and Figure 3-45 respectively.

The study of the effect of ambient temperature on the peak temperature of the tooth shows that as the ambient temperature increases the peak temperature of the gear increases. The explanation for that is the change in convection heat loss. Increasing the ambient temperature reduces the amount of heat loss by convection so most of the heat stays in the gear material.

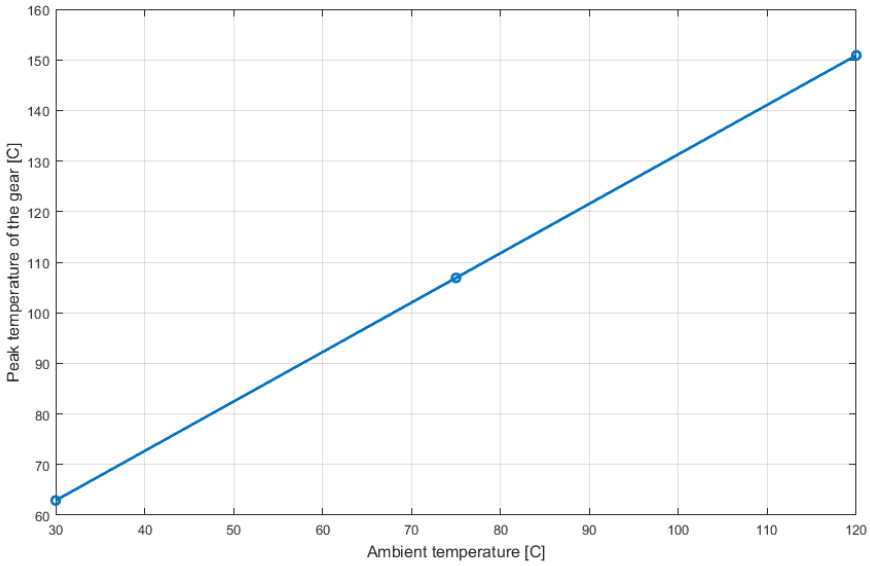

Figure 3-44 The effect of ambient temperature on the peak temperature of the high contact gear tooth

The study for the effect of shaft temperature on the peak temperature of the tooth reveals that increasing the temperature of the shat will lead to a slit increase in the peak temperature of the tooth.

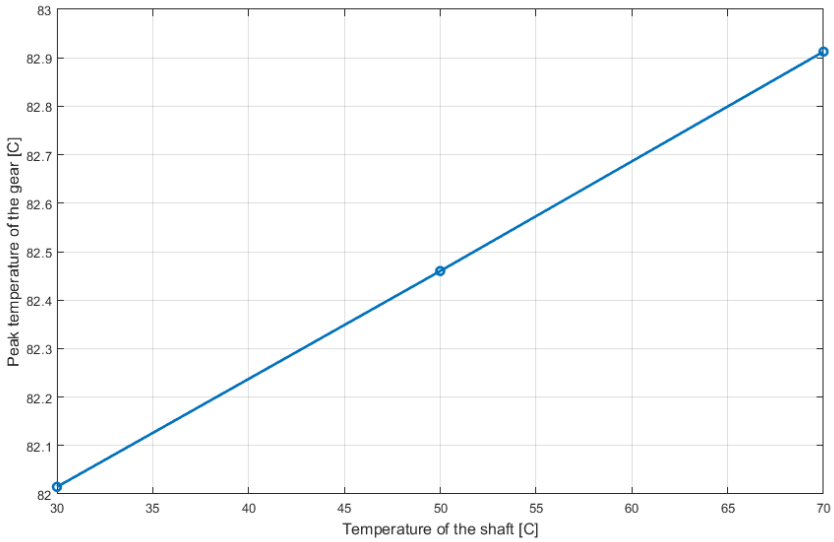

Figure 3-45 The effect of shaft temperature on the peak temperature of the high contact gear tooth

3.3.12. Thermal stress and thermal deformation

As explained in the equation of thermal stress. The uneven heating for the gear tooth material will lead to a thermal deformation in the gear tooth. Since the temperature distribution in the standard contact tooth is different from the high contact teeth. The thermal stress and thermal deformation results will be different. The results of the thermal stress and total thermal deformation are presented in Figure 3-46 and Figure 3-47 respectively.

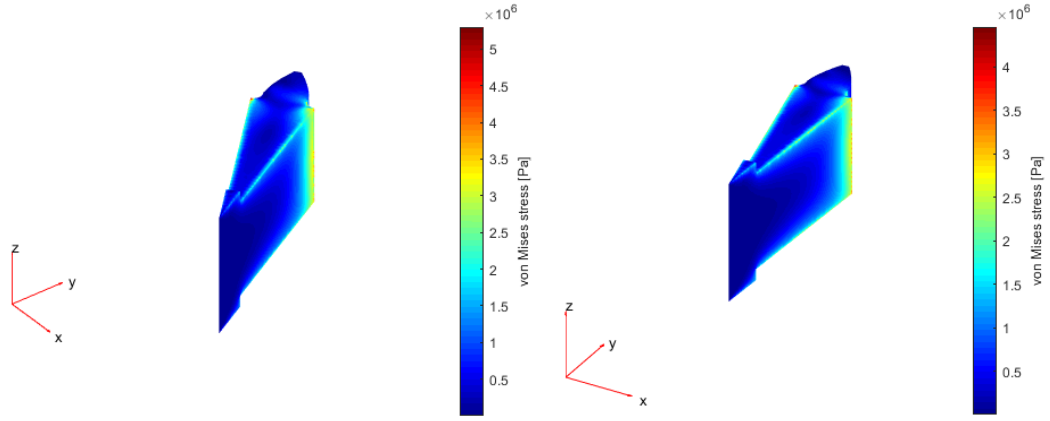

Figure 3-46: a) Thermal stress in standard contact gear b) Thermal stress in high contact gear

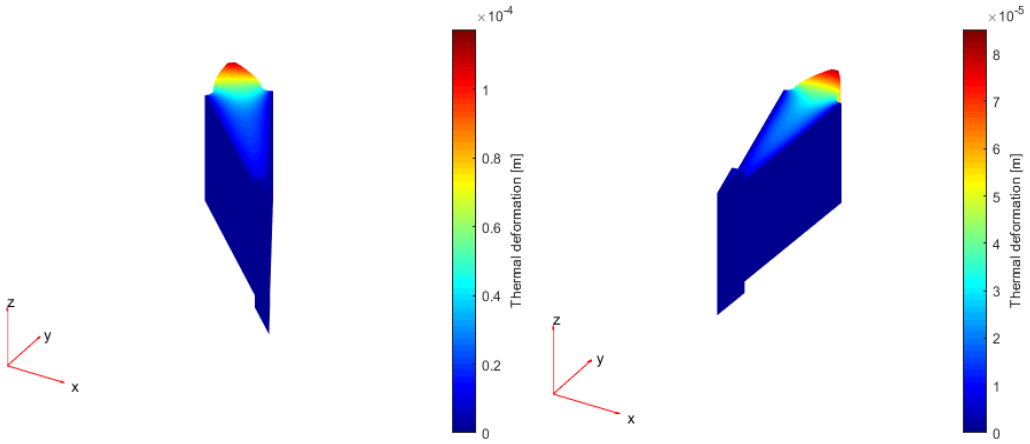

Figure 3-47: a) Thermal deformation in standard contact gear b) Thermal deformation in high contact gear

The results of thermal stress and thermal deformation confirm that the thermal stress and thermal deformation is larger in standard contact than the high contact. The previous results for temperature distribution indicate that the temperature in the standard

contact is high than the temperature in the high contact. This higher temperature in standard contact reflected on the thermal stress and thermal deformation in the gears tooth. The justification for that is the temperature is the main source for the thermal stress and thermal deformation.

3.3.13. Thermal deformation standard vs high.

The simulation results also include a comparison in thermal deformation in X, Y, and Z axes for standard and high contact system.

The results of thermal deformation in X, Y, and Z axes are shown in Figure 3-48, Figure 3-49, and Figure 3-50 respectively.

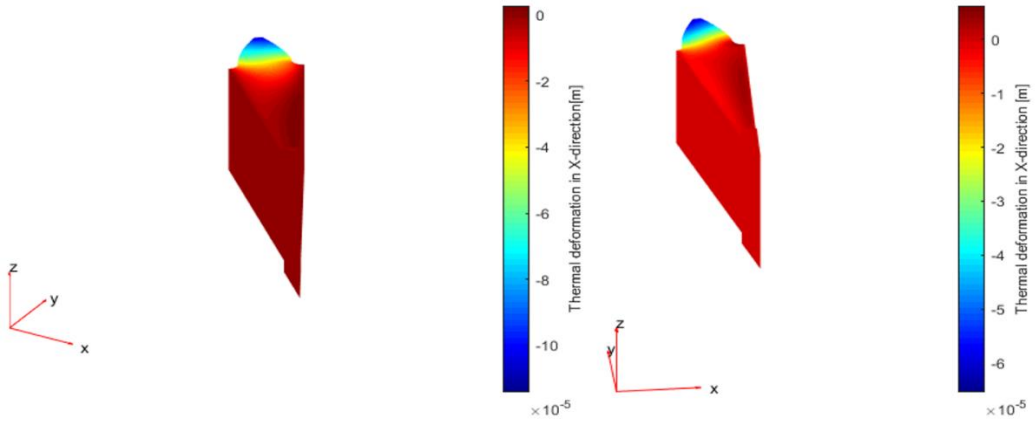

Figure 3-48 Thermal deformations for standard contact and high contact gears teeth in the X direction

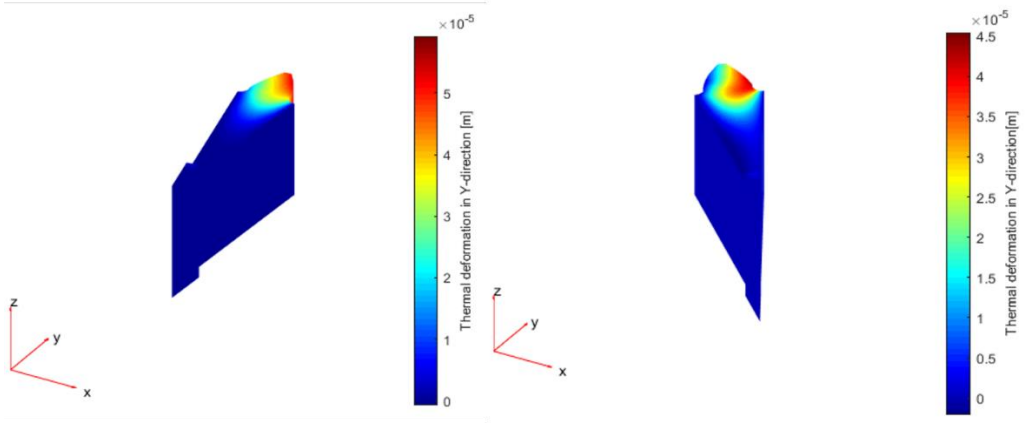

Figure 3-49 Thermal deformation for standard contact and high contact gears teeth in the Y direction

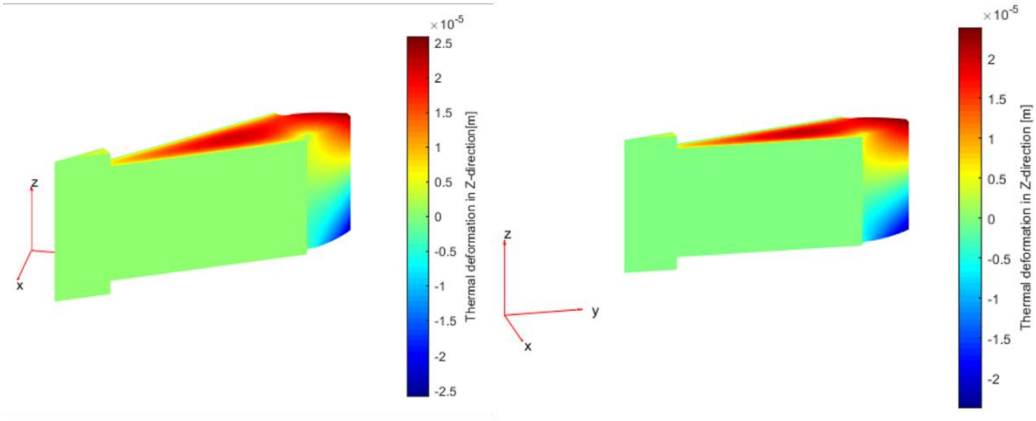

Figure 3-50 Thermal deformation for standard contact and high contact gears teeth in the Z direction

The results of the thermal deformation in the X, Y, and Z coordinate is compatible with the results of the total deformation. This compatibility occurs because these stresses are the components for the total thermal deformation.

3.3.14. Prediction models

Prediction models have been built for the gear model. The prediction models will use the machine learning method and the empirical formula. The prediction models will be used to forecast the average and total sliding power loss in gears.

3.3.14.1. Design of experiment.

To building a prediction model a sequence of steps should be followed before. The first step is selecting the parameters for your forecast model. The parameters for gear power loss and temperature prediction has been done in the parametric study. The second step is specifying the range for each parameter based on the real cases. The third step is building a Design of Experiment (DOE) using forecast parameters. The DOE has two types. The first type is fractional factorial and the other one is Full Factorial (FF). The fractional factorial has a smaller number of tests needed but it has less accuracy. The full factorial tests all possible cases and realize a more accurate model than fractional factorial.

When the test data are available the prediction model will be ready to be trained using the available data. For the gear system, 10 parameters have been selected to build the prediction model and prediction formula. These parameters are the number of teeth in pinion, the number of teeth in gear, module, base circle diameter for pinion, base circle diameter for gear, fluid lubricant viscosity, the temperature of the surrounding, the temperature of the shaft, rotating speed, and input torque. The range of each parameter is shown in Table 3-7.

Table 3-7 Design of experiment parameters

Parameter	Range	Levels	Unit
Number of teeth in pinion	12-96	3	-----
Number of teeth in the gear	12-96	3	-----
Module	1-5	3	mm
Base circle diameter for pinion	50-500	3	mm
Base circle diameter for the gear	50-500	3	mm
Fluid lubricant viscosity	0.01-0.6	3	Pa.s
Temperature of the surrounding	30-120	3	^{o}C
Temperature of the shaft	50-150	3	^{o}C
Rotating speed	500-5000	3	rpm
Input torque (Torque of operation)	10-400	3	N.m

First, the fractional factorial method has been tried because it needs a fewer number of tests. Box–Behnken DOE (Response Surface Analysis) has been utilized for making the DOE for the gear project. For 10 parameters and 3 levels for each parameter, the RSM DOE results in 161 tests to be done. For these parameters, the range of the transmitted power is (523.7 Watt– 209439 Watt) which is equal to (0.702 hp - 280.86 hp). Also, the rotating speed of driven gear will be (62.5 rpm- 40000 rpm).

All the cases have been simulated using the validated code. The produced database has been used to build the machine learning model and the empirical formula. The results of the prediction model will be the average and RMS for the power loss for a single tooth.

3.3.14.2. Machine learning prediction model.

In the GP method, the data are assumed to have a distribution function f, where this function is used to estimate the value of the next points. The function value can be described as $f(\cdot) \sim GP\big(m(\cdot), \kappa(\cdot,\cdot)\big)$, where $m(\cdot)$ is the mean function. The mean function is usually assigned to be zero. The zero value for mean function gives the flexibility for conditional mean to be determined by covariance function. $\kappa(\cdot,\cdot)$ is the covariance function. Each method has an assumption for the covariance function.

For the machine learning prediction model, 6 accurate prediction methods have been tested to make the prediction model. Gaussian Process (GP) with different covariance functions have been tested. These models are Gaussian squared exponential, Gaussian Matern 5/2, Gaussian rational quadratic, and Gaussian exponential. The difference between these models is the covariance functions. The formulas of the covariance function for each model are listed in the table below.

The meaning of the parameters in the covariance functions was described in section 2.2.8.4.

Table 3-8 Gaussian process covariance functions

Gaussian model	Covariance function formula
Gaussian squared exponential	$\kappa(s) = \exp\left(-\frac{s^2}{2l^2}\right)$
Gaussian Matern 5/2	$\kappa(s) = \frac{2^{1-\nu}}{\Gamma(S)}\left(\frac{\sqrt{2\nu}s}{l}\right)^{\nu} K_{\nu}\left(\frac{\sqrt{2\nu}s}{l}\right)$
Gaussian rational quadratic	$\kappa(s) = \exp\left(1 + \frac{s^2}{2\alpha l^2}\right)^{-\alpha}$
Gaussian exponential	$\kappa(s) = \exp\left(-\frac{s}{l}\right)$

3.3.14.3. Data Log transformation

The performance of the prediction models could be improved by making some data transformation. The goal of transforming the data is to reduce the range of the target parameter (dependent variable). This reduction in the range may improve the prediction significantly. Log transformation is a very common data transformation method. The Log transformation is chosen for the system because the standard deviation is proportional to the mean of the data. The log transformation applied by taking the Log for the target parameter value. Use the transferred data to train the machine learning model. The trained model predicting the Log of the target parameter, so take the exponential for the predicted number to get the correct value of the parameter. This method has been applied to improve the prediction of the RSM machine learning model. This method will also reduce the training time for the machine learning model and will increase the speed of prediction.

Figure 3-51 shows a flow diagram for the steps of making the Log transformation for the data and return the data to its original.

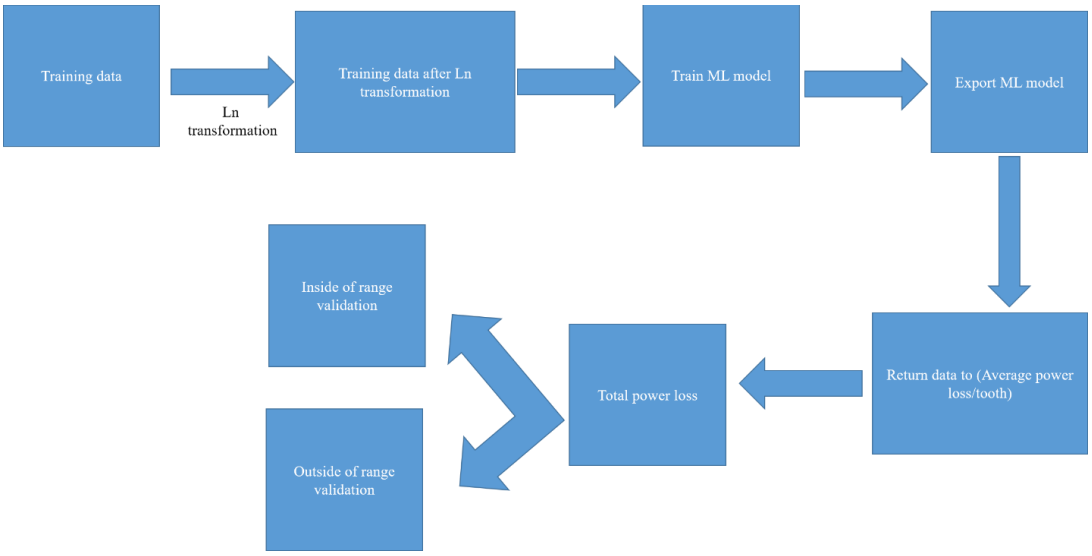

Figure 3-51 Flow diagram for data transformation

The flow diagram for building and use the ML prediction model for the sliding power loss in gears is shown in Figure 3-52. The diagram shows how to select the parameters, make DOE, simulate the cases, choose the ML model, and train the model. After exporting the trained The ML model the diagram shows the needed parameters and the methodology of using the ML model for prediction.

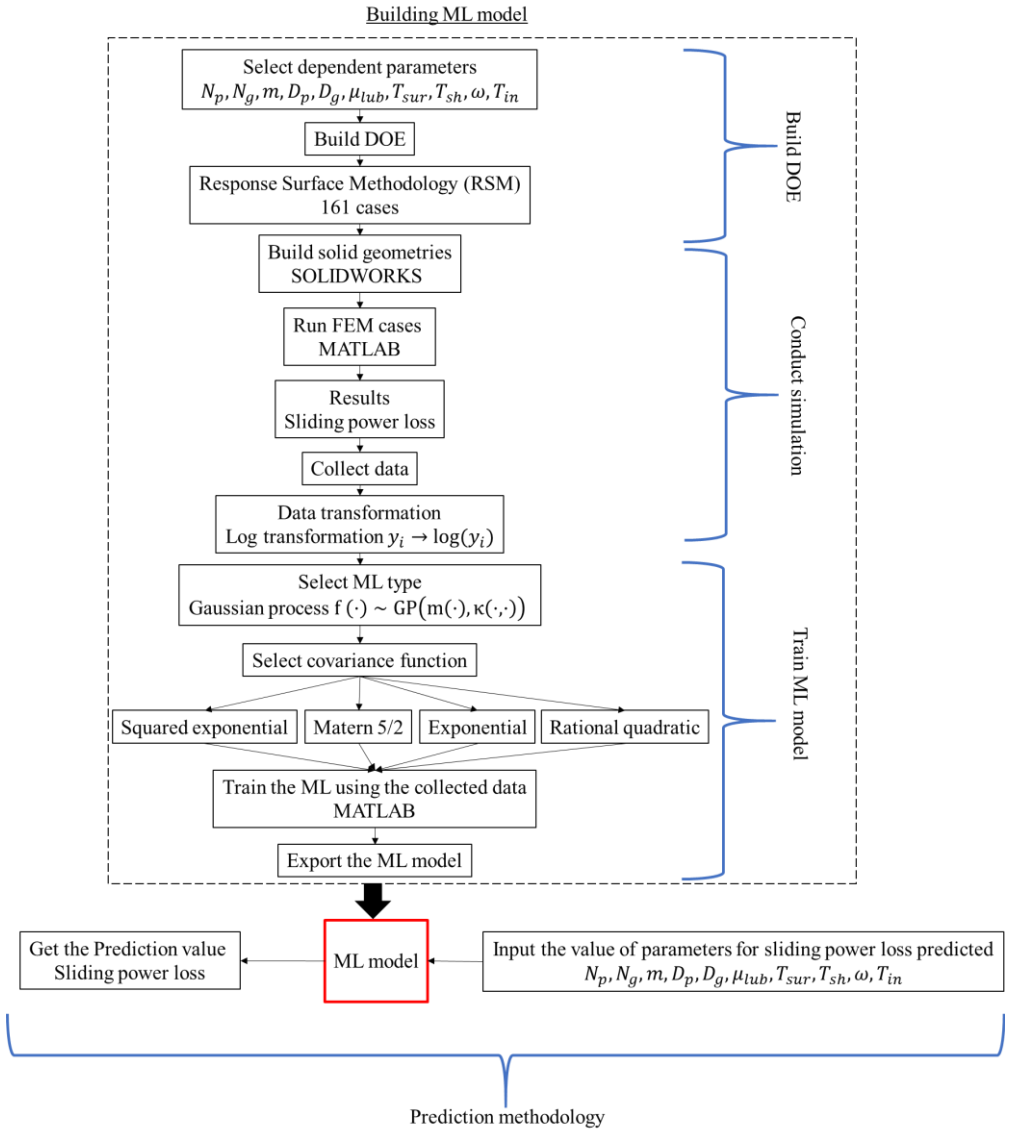

Figure 3-52 Flow diagram for build, train and used ML model for sliding power loss prediction in gears

The accuracy of prediction for the machine learning prediction model after Log transformation for the data is shown in Figure 3-53. The figure shows good accuracy for the prediction model after transforming the data.

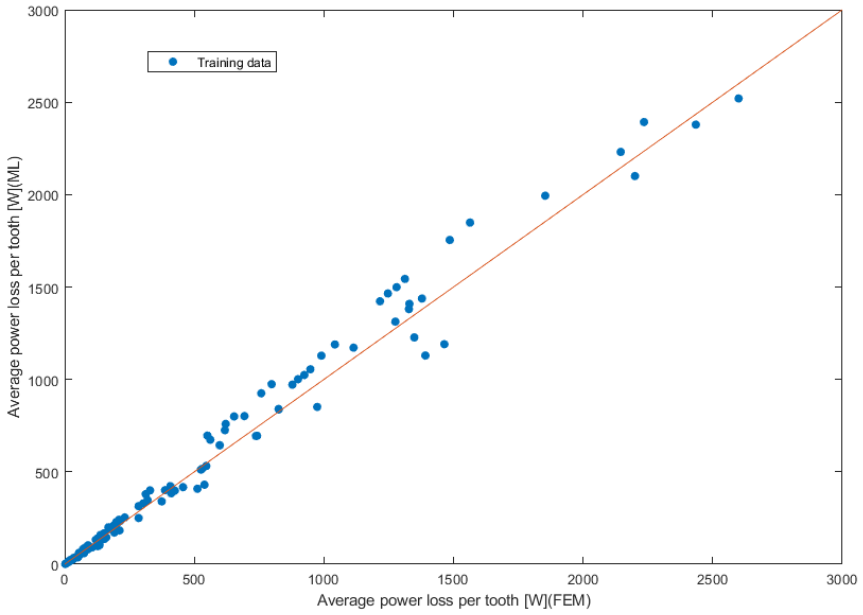

Figure 3-53 Machine learning model prediction for the average sliding power loss in gears

3.3.14.4. Empirical formula

Many correlation methods are accessible for use. One of the most famous methods is Rayleigh's method. For the mathematical model, Rayleigh's method has been chosen for this correlation. Rayleigh's method is a widely used method to generate correlations for different applications in physics and engineering applications. The general formula of this method is shown in Eq. 3-88.

$$R_o = CR_1^a R_2^b R_3^c \dots R_n^m \qquad \textbf{Eq. 3-88}$$

Where R_o is the output value; C is the correlation constant and was found based on the DOE results; $R_1, R_2 \dots R_n$ are DOE parameters; and $a, b \dots m$ are the powers of the DOE parameters.

For the average power loss per tooth general form of Eq. 3-89 has been chosen based on the prediction parameters.

$$P_{avg} = CN_p^a N_g^b m^c D_p^d D_g^e \mu_{lub}^f T_{sur}^g T_{sh}^h \omega^i T_{in}^j \quad \textbf{Eq. 3-89}$$

Where

C: constant

N_p: Number of teeth for pinion

N_g: Number of teeth for gear

m: Module [mm]

D_p: Base diameter for the pinion [mm]

D_g: Base diameter for the gear [mm]

μ_{lub}: The viscosity of the lubricant [Pa. s]

T_{sur}: The temperature of the surrounding [°C]

T_{sh}: The temperature of the shaft [°C]

ω: Rotating speed [rpm]

T_{in}: Input torque [N. m]

a, b, c, d, e, f, g, h, i, h, i, and j : are the power of the parameters

A MATLAB code has been used to evaluate the values for each parameter. The final formula for average sliding power prediction is presented in Eq. 3-90.

$$P_{avg} = -1.9791\ N_p^{0.50257} N_g^{-0.52821} m^{1.1209} D_p^{-0.89203} D_g^{0.019193} \mu_{lub}^{0.055542} T_{sur}^{-0.1893} \times T_{sh}^{-0.038728} \omega^{1.0628} T_{in}^{0.77065} \quad \textbf{Eq. 3-90}$$

This formula can forecast the average sliding power loss per tooth. This formula is applicable for standard contact and high contact gears. Eq. 3-91 could be used to calculate the total sliding power loss in the gear system.

$$\text{Total}_{\text{sliding power loss}} = \text{Average}_{\text{sliding power loss single tooth}} \times \text{Contact ratio} \quad \textbf{Eq. 3-91}$$

The accuracy of the formula has been tested to predict the training data. The accuracy of prediction for the formula is shown in Figure 3-54.

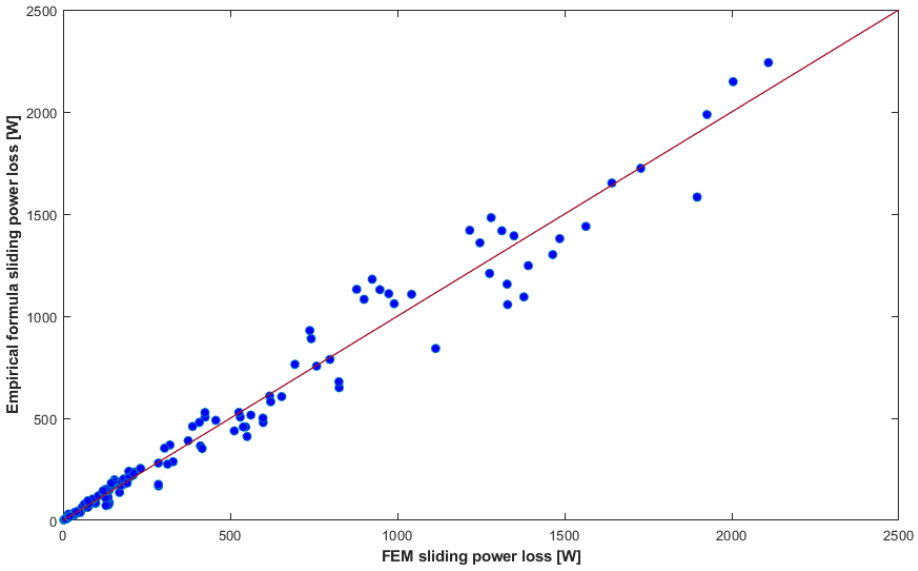

Figure 3-54 The accuracy of the prediction for the empirical formula

The figure shows a comparison between the average sliding power loss per tooth that has been simulated using FEM and the value for the average sliding power loss by the formula. The formula achieved a high accuracy in prediction where the value of R^2 for the

formula was 0.98. Also, the value of RMSE was 84.68. These values prove the accuracy of the model. The formula also has been validated by validation cases.

Table 3-9 The accuracy of prediction for the ML models and the empirical formula

Prediction method	**Data transformation**	**RMSE**	**R^2**	**Prediction speed [observation /s]**	**Training time [s]**
Gaussian squared exponential	No	194.96	0.85	910	46.26
	Yes	76.24	0.99	1800	9.27
Gaussian Matern 5/2	No	202.46	0.84	980	52.18
	Yes	75.96	0.99	7300	10.3
Gaussian rational quadratic	No	194.96	0.85	940	71.41
	Yes	76.01	0.99	1700	10.11
Gaussian exponential	No	267.58	0.72	900	56.63
	Yes	82.84	0.98	8600	10.2
Cubic SVM	No	292.05	0.67	930	13.8
	Yes	83.36	0.98	4800	8.57
Ensemble boosted tree	No	290.51	0.67	280	28.82
	Yes	200.74	0.84	1700	11.72
Empirical formula	----------	84.68	0.98	----------	--------

3.3.14.5. Machine learning vs empirical formula

Table 3-9 shows the performance of the best ML prediction models and the empirical formula. The summary includes the performance of ML models before and after (Ln transformation) for the data in addition to the empirical formula. The comparison includes the accuracy by the value of R^2, prediction speed for each model, and the training time for each model.

3.3.14.6. Validation for prediction models

Any prediction model should be validated to prove the accuracy of the model. For the gear project, two types of validation have been proposed. The first type of validation is inside of range validation. In this validation method, random cases inside of the range of parameters in the DOE should be tested. This method confirms the accuracy of the prediction model for cases inside of range and different from the training data. The second type of validation is outside of range validation. This validation uses to ensure the precision of the prediction model if it is applied to cases outside of the range of the parameters of the DOE. These two validation methodologies have been applied to the machine learning prediction model and the empirical formula.

The results of the validation for the machine learning model and empirical formula to predict the average power loss per tooth are shown in Figure 3-55 and Figure 3-56 respectively. The blue points in the graphs are the training data for the machine learning model and empirical formula. The red points are the validation points have been tested

inside of the range of the parameters of DOE. The outside of range validation cases is presented in the orange points.

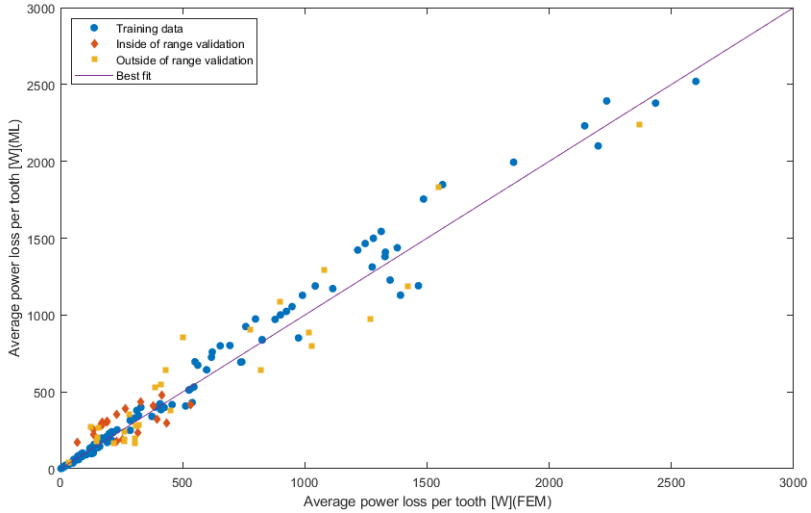

Figure 3-55 Machine learning prediction accuracy for validation cases for the average power loss

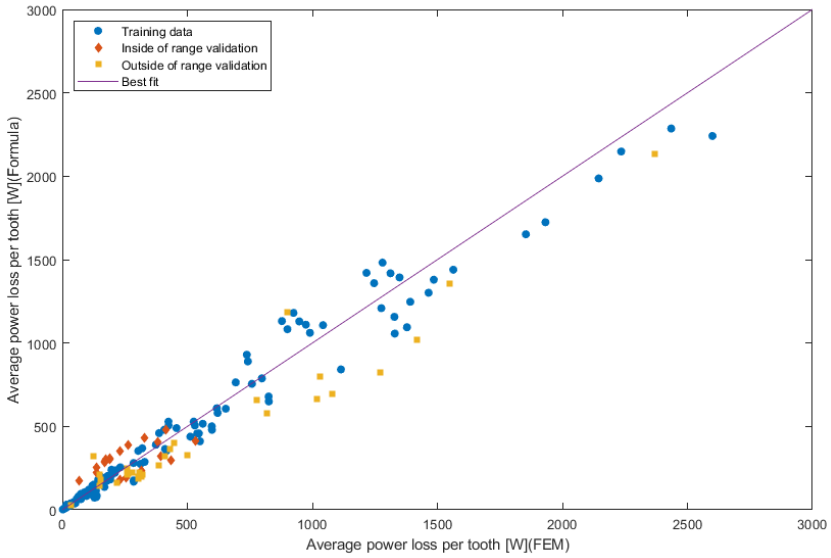

Figure 3-56 Empirical formula prediction accuracy for validation cases for the average power loss

The results of validation for the average power loss machine learning model and formula show that the prediction for the machine learning model is better than the formula for outside of range validation cases. The performance in forecasting the inside of range validation cases is very close with some preference for the machine learning model

The validation for the total power loss prediction for both the machine learning model and the empirical formula is viewed in Figure 3-57 and Figure 3-58 respectively. This study has been done to ensure the accuracy of prediction models after converting the average sliding power loss to the total sliding power loss.

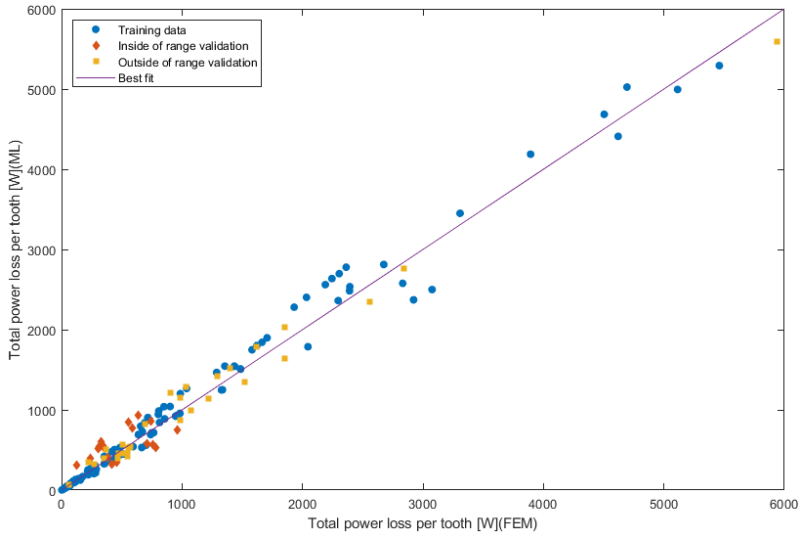

Figure 3-57 Machine learning prediction accuracy for validation cases for the total power loss

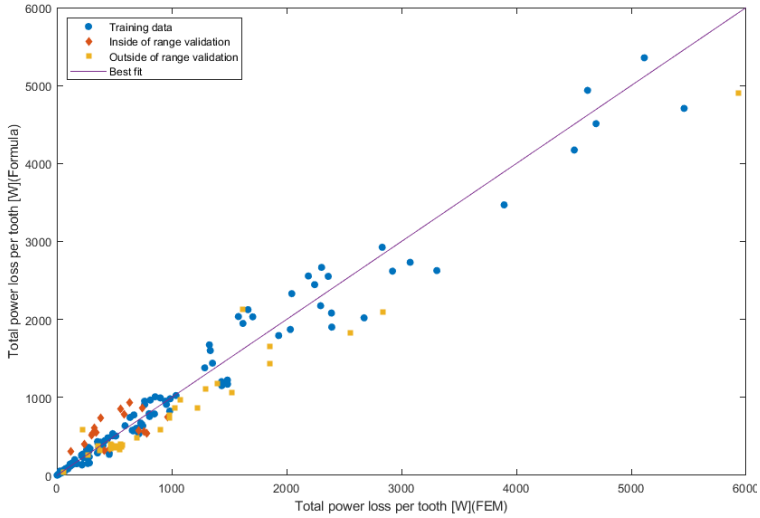

Figure 3-58 Empirical formula prediction accuracy for validation cases for the total power loss

The results of predicting the total sliding power loss are matching with the results of the average sliding power loss. This compatibility proves the accuracy of this model in predicting the total sliding power loss in gears.

3.3.15. Mixed lubrication

Mixed lubrication is a famous case when the lubrication film thickness is close to the surface roughness. In this type of lubrication, the asperities of the surface share a prat from the load on the surface. The other part of the load is held by the lubrication fluid. Mixed lubrication will increase the friction between the contacted surface because the friction coefficient between asperities is high relative to the hydrodynamic friction. The load held by the asperities and the lubricating fluid should be determined to make the simulation. Goodman and Williamson's model is a famous model used to analyze the mixed lubrication case [102]. Goodman's model will be used to make this simulation.

The pressure on the asperities and the lubricating fluid is described by Eq. 3-92 and Eq. 3-93 respectively [86].

$$p_{hyd} = \frac{p_{total}}{\gamma_1} \quad \textbf{Eq. 3-92}$$

$$p_{asp} = \frac{p_{total}}{\gamma_2} \quad \textbf{Eq. 3-93}$$

where the condition in Eq. 3-94 should be satisfied

$$\frac{1}{\gamma_1} + \frac{1}{\gamma_2} = 1 \quad \textbf{Eq. 3-94}$$

3.3.15.1. Greenwood and Williamson model

Based on Greenwood and Williamson's model the area of each asperity is calculated by Eq. 3-95.

$$A_i = \pi\beta(z_i - d) \quad \textbf{Eq. 3-95}$$

where

z_i : Asperity height

β: Asperity diameter

d: The distance between surfaces

The total area of asperities is equal to the sum of the areas of each asperity Eq. 3-96

$$A_{total} = A_i \times n \quad \textbf{Eq. 3-96}$$

Where the value of n can be calculated by Eq. 3-97

$$n = N_{as} e^{-d/\sigma} \quad \textbf{Eq. 3-97}$$

N_{as}: Number of asperities, σ: Standard deviation of asperities

Force held by each asperity is calculated by Eq. 3-98.

$$F_i = \frac{2}{3}\beta^{0.5}E'(z_i - d) \quad \textbf{Eq. 3-98}$$

The total force on the asperities is the sum of the forces held by each asperity in the contact region as shown in Eq. 3-99.

$$F_{total} = F_i \times n \quad \textbf{Eq. 3-99}$$

The pressure that has been shared by the asperities is evaluated by Greenwood and Williamson model as shown in Eq. 3-100.

$$p_{asp} = \frac{2}{3}n\sigma_s E' \int_d^{\infty}(z - d)^{\frac{3}{2}}\varphi_s(z)dz \quad \textbf{Eq. 3-100}$$

where σ_s is the standard deviation of the high of asperities. $F_{\frac{3}{2}}$ is a statistical function used by Greenwood and Williamson model. d is the distance between the average high of asperities as shown in Figure 3-59.

The Eq. 3-100 is simplified to the shape in Eq. 3-101.

$$p_{asp} = \frac{2}{3}n\sigma_s\sqrt{\frac{\sigma_s}{\beta}}E'F_{\frac{3}{2}}\left(\frac{d}{\sigma_s}\right) \quad \textbf{Eq. 3-101}$$

The total sliding power loss for the mixed lubrication model is the sum of the sliding power loss by asperities and the sliding power loss by the hydrodynamic model as shown in Eq. 3-102.

$$P_{total} = P_{asp} + P_{hyd} \quad \textbf{Eq. 3-102}$$

The methodology of evaluating hydrodynamic sliding power loss (P_{hyd})was described before in the chapter of the methodology of simulating hydrodynamic power loss. The value of the sliding power loss from asperities can be calculated by Eq. 3-103

$$P_{asp} = U_s \times w \times \mu_{friction}$$ **Eq. 3-103**

The methodology for solving for the total sliding power loss in the mixed lubrication condition is shown below. In the mixed lubrication after evaluating the pressure on the asperities and the hydraulic pressure, the sliding power loss for the asperities and the lubricating fluid will be calculated separately.

The value of the total friction coefficient depends on the amount of pressure on the contact point. Increasing the pressure will increase the load shared by asperities. As the load shared by asperities increases the friction coefficient between the surface increases. This is compatible with the Stribeck curve.

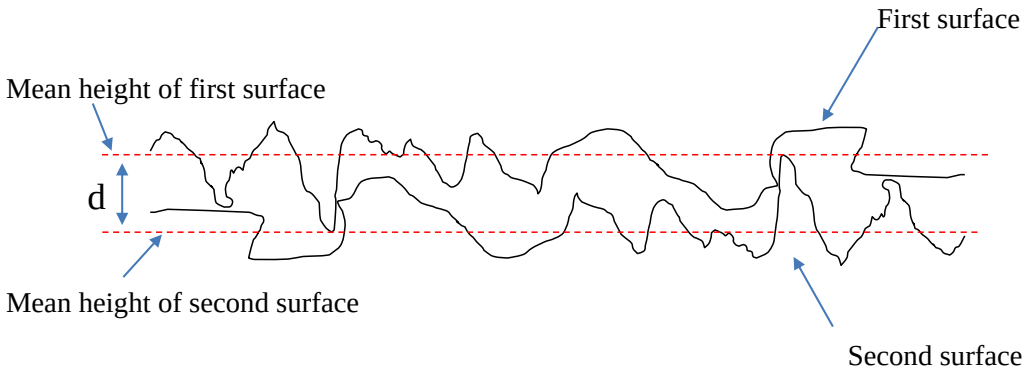

Figure 3-59 Mean high of the asperities for two rough surfaces

The amount of pressure shared by the asperities is significantly affected by the roughness of the surface. Increasing the surface roughness will increase the load shared by asperities and this will increase the sliding power loss between the surfaces.

The type of lubrication depends on the minimum film thickness and surface roughness. Eq. 3-104 shows the methodology to determine the type of lubrication.

$$\lambda = \frac{h_{min}}{R_a}$$ **Eq. 3-104**

where h_{min} is the minimum film thickness and R_a is the average roughness of the surface.

The boundary lubrication will occur if the value of λ is less or equal to 1. The mixed lubrication happened when λ in the range of $1 < \lambda < 3$. If the value of λ is equal or more than 3 the lubrication will be hydrodynamic lubrication [103]. The value of average surface roughness R_a may vary from $50\ \mu m$ for N12 ISO grad number to $0.025\ \mu m$ for N1 ISO grad number.

3.3.15.2. Case study

For the case study, the test will be done for standard contact ratio (SCR) and high contact ratio (HCR) gears. Figure **3-60** shows the variation of minimum film thickness along the line of action for standard contact and high contact gears. The figure shows that the minimum film thickness in the standard contact is changing from $0.9\ \mu m$ to $2.5\ \mu m$ along the line of action. For high contact gears, the minimum film thickness value fluctuating from $1.25\ \mu m$ to $4.5\ \mu m$. Based on this data, the type of lubrication for both systems may be different for the same roughness.

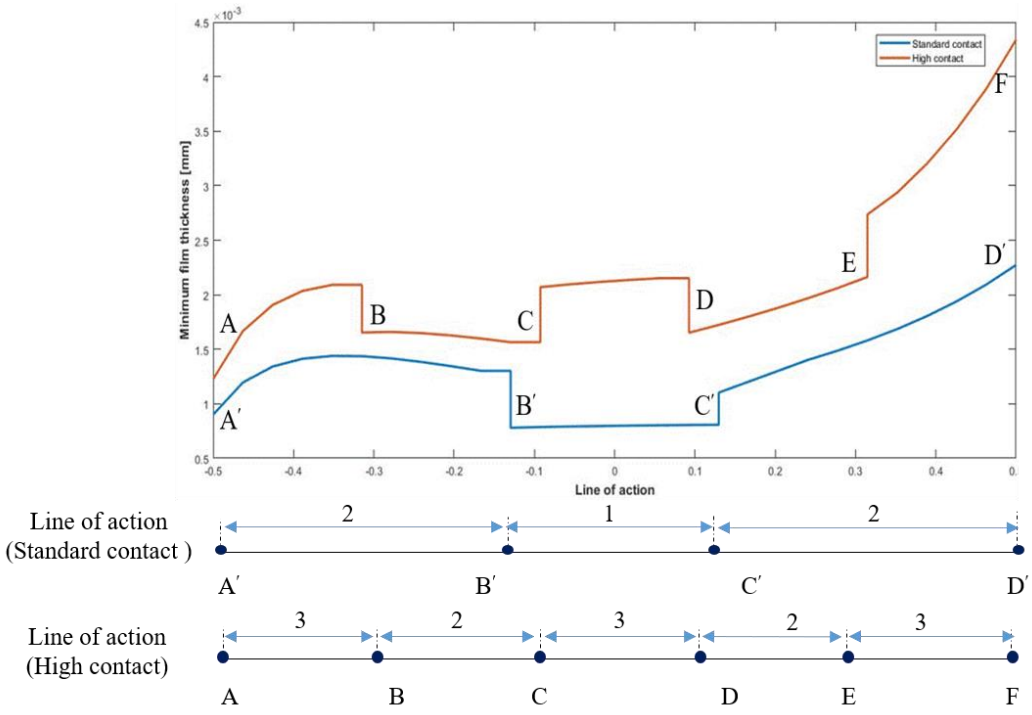

Figure 3-60 Variation of minimum film thickness along the line of action

In the case study for the standard contact and high contact and based on. The classification of the lubricating type is shown in Table 3-10. This classification was built based on the film thickness along the line of action. Based on this assumption the type of lubrication could be changed along the line of action for the same surface roughness due to the variation of the film thickness.

Different values for the average roughness R_a will be tested. The values of the cases are listed in Table 3-11. The table also shows the type of lubrication for each case based on the minimum film thickness in the line of action. This means that the type of lubrication could be changed along the line of action for the same parameters. The friction coefficient

for the asperities was assumed to be 0.2. During the simulation, all the input parameters stay the same as the beginning of the simulation.

Table 3-10 Ranges of the types of lubrication

Type of contact	R_a for boundary lubrication	R_a for mixed lubrication	R_a for hydraulic lubrication
Standard contact	$R_a \geq 0.8$ μm	0.27 μm $< R_a < 0.8$ μm	$R_a \leq 0.27$ μm
High contact	$R_a \geq 1.25$ μm	0.42 μm $< R_a < 1.25$ μm	$R_a \leq 0.42$ μm

Table 3-11 Types of lubrication for the case study

Value of R_a (μm)	Type of lubrication in Standard Contact Ratio gears	Type of lubrication in High Contact Ratio gears
5	Boundary lubrication	Boundary lubrication
1	Boundary lubrication	Mixed lubrication
0.6	Mixed lubrication	Mixed lubrication
0.1	Hydrodynamic lubrication	Hydrodynamic lubrication

The type of lubrication will be determined at each time step to avoid the problem of changing the type of lubrication during the simulation.

The results of the simulation for the single tooth are presented in Figure 3-61 and Figure 3-62 and for both standard contact and high contact ratio respectively. The results for four different values for average surface roughness. The values of surface roughness are $Ra = 5\ \mu m$, $Ra = 1\ \mu m$, $Ra = 0.6\ \mu m$, and $Ra = 0.1\ \mu m$. The results show that at $Ra = 5\ \mu m$ the power loss is maximum for standard contact and high contact ratio. The reason for that is the boundary lubrication type for this surface roughness. The figures also show that as the average surface roughness increases the amount of sliding power loss increases. At $Ra = 0.1\ \mu m$ both the standard contact and high contact have hydrodynamic lubrication. The mixed lubrication occurs at $Ra = 1\ \mu m$ and $Ra = 0.6\ \mu m$ for both contact types.

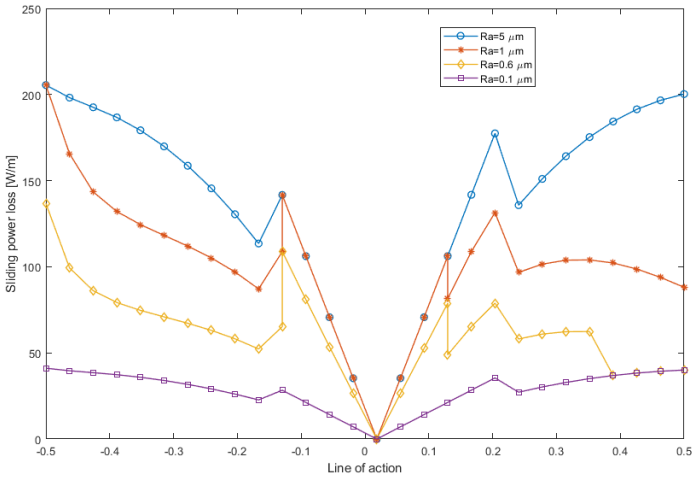

Figure 3-61 Sliding power loss for standard contact ratio along the line of action for different surface roughness

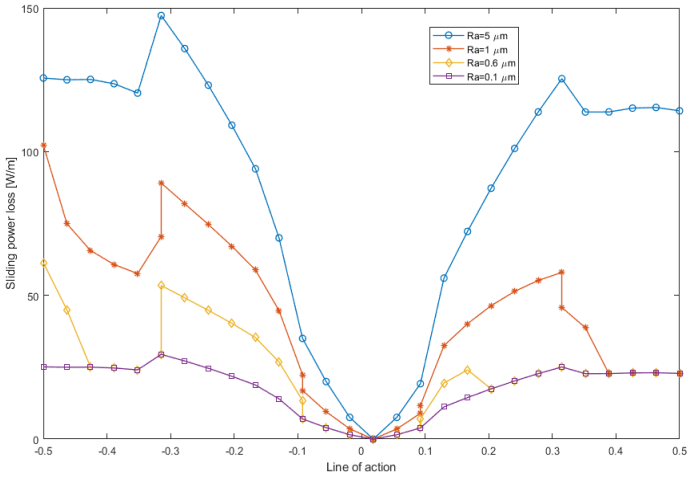

Figure 3-62 Sliding power loss for high contact ratio along the line of action for different surface roughness

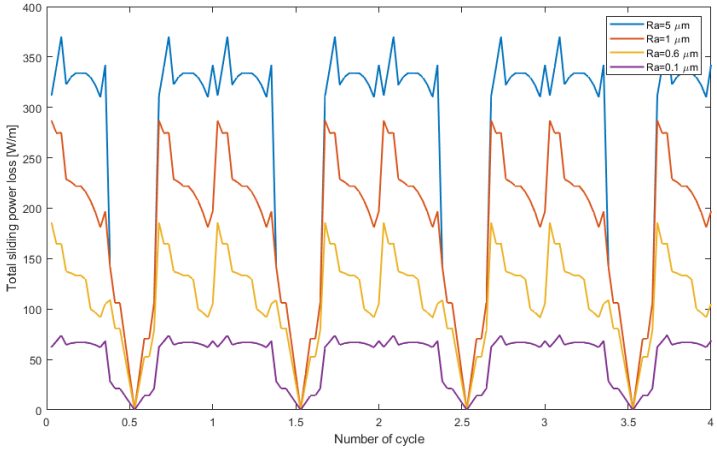

Figure 3-63 Total sliding power loss for standard contact ratio for different surface roughness

Figure 3-63 and Figure 3-64 are the results for total sliding power loss for standard contact and high contact ratio respectively for four cycles. The results viewed that the maximum total power loss in standard contact is larger than standard contact ration. The

results also show that the fluctuation in the standard contact ratio is larger than high contact ratio gears.

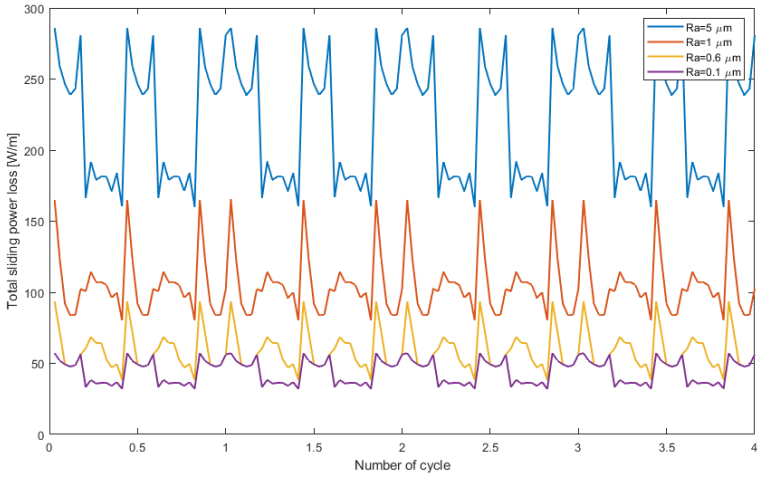

Figure 3-64 Total sliding power loss for high contact ratio for different surface roughness

3.3.16. Fatigue life

This section includes an analysis and case study for the fatigue life for the tooth of the gear. Goodman's method has been used in this analysis.

3.3.16.1. Introduction

Fatigue life is a method to predict the life and the failure of the equipment. The life of the equipment depends on several factors like the load on the equipment, the surface finish, type of the material, and the dimensions of the specimen [19].

The failure of the specimen occurs by levels. The first level is the initiation of the crack in the equipment. The second step is the growth of the crack. The final step is the failure of the specimen.

There are several methods used to predict the fatigue life. The methods depend on the assumptions of the method. The correlations and the formulas of the prediction methods built on actual experimental results.

The general behavior of the equipment's life can be described by the S-N curve. Figure 3-65 shows an example of the S-N curve [104]. The curve shows that the lifetime of the equipment can be classified into three categories. The first one is low cycle fatigue. The low cycle fatigue occurs if the fatigue life is less than 1000 cycles. The second type is high cycle fatigue. The high cycle fatigue is the region between the low cycle fatigue and the endurance limit. The third region is the endurance limit or infinite life.

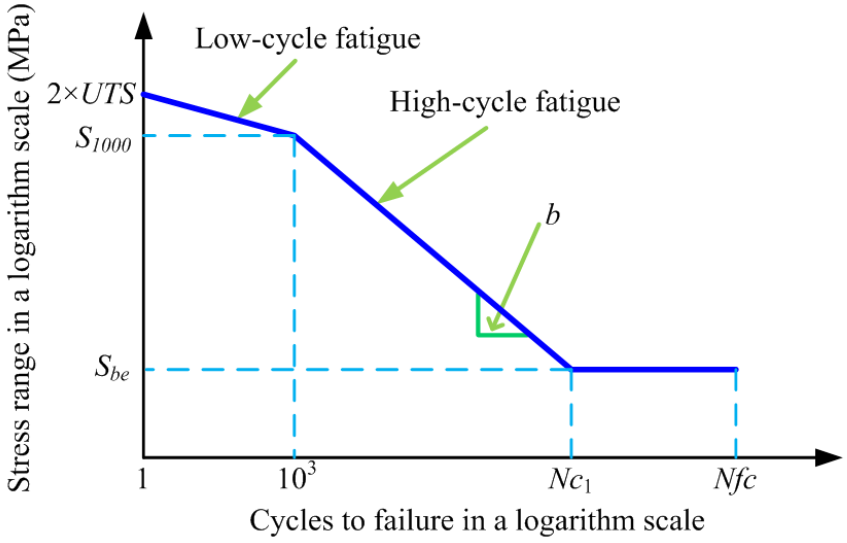

Figure 3-65 S-N curve [104]

3.3.16.2. Fatigue life analysis

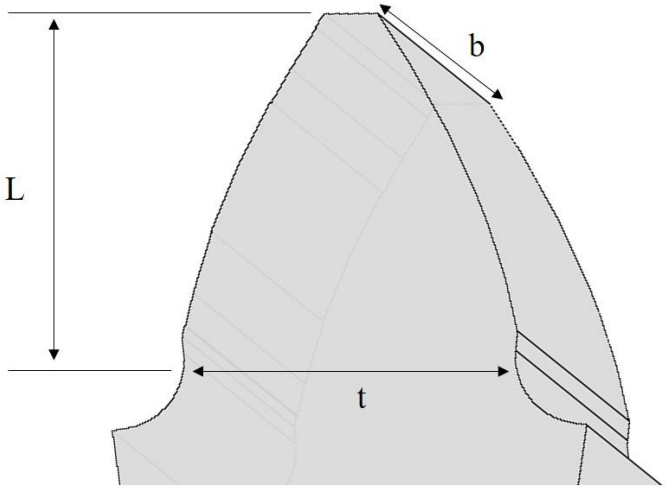

Figure 3-66 Gear tooth geometry

The bending stress in the gear tooth can be calculated as shown in Eq. 3-105 [105].

$$\sigma_b = \frac{6L}{bt} w \qquad \textbf{Eq. 3-105}$$

Where $L, b,$ and t are the dimensions in the gear tooth as shown in. F_n is the normal force in acting on the gear tooth.

The normal force is deferent between the standard contact and high contact for the same input torque based on the FEM analysis.

The fatigue life of the gear tooth can be evaluated by Eq. 3-106 [105].

$$N_{failure} = \left(\frac{\sigma_b}{a}\right)^{\frac{1}{b0}} \qquad \textbf{Eq. 3-106}$$

N is the number of cycles before failure. a and b are constants. The constant (a) can be calculated by Eq. 3-107 [105].

$$a = \frac{(f \times S_{ut})^2}{S_e} \quad \textbf{Eq. 3-107}$$

S_{ut} and S_e are the ultimate strength and the corrected endurance limit for the material [105].

$$b_0 = -\frac{1}{3}\mathrm{Log}\left(\frac{f \times S_{ut}}{S_e}\right) \quad \textbf{Eq. 3-108}$$

The correction factor f can be estimated by Eq. 3-109 [106].

$$f = \frac{\sigma'_f}{S_{ut}}(2N_{failure})^{b0} \quad \textbf{Eq. 3-109}$$

Where $\sigma'_f = S_{ut} + 345$.

The equation of constant $b0$ is Eq. 3-110 [106].

$$b0 = -\frac{\mathrm{Log}(\sigma'_f + S'_e)}{\mathrm{Log}(2N_e)} \quad \textbf{Eq. 3-110}$$

The corrected endurance limit described in Eq. 3-111 [106].

$$S_e = k_a k_b k_c k_d k_e k_f S'_e \quad \textbf{Eq. 3-111}$$

To determine the value of surface factor Eq. 3-112 should be solved. The values of $a1$ and $b1$ factors are 4.51 and -0.265 respectively [106].

$$k_a = a1(S_{ut})^{b1} \quad \textbf{Eq. 3-112}$$

The size factor can be calculated using Eq. 3-113 [106].

$$k_b = 1.24b^{-0.107} \quad \textbf{Eq. 3-113}$$

The value of $k_c = 1$ for the bending load. The value of k_d should be evaluated if the operating temperature is higher than the room temperature [106]. The factor can be calculated by Eq. 3-114.

k_d=0.975+0.432×10−3TF−0.115×10−5TF2+0.104×10−8TF

Eq. 3-114

3−0.595×10−12TF4

For 99% reliability the reliability factor $k_e = 0.814$. and $k_f = 1$ [106].

3.3.16.3. Fatigue life case study

The input parameters for the case study are shown in Table 3-12.

Based on Eq. 3-93 the fatigue life depends on the normal force acting on the gear tooth. Figure 3-67, Figure 3-68, and Figure 3-69 show a comparison in fatigue life between standard contact and high contact ratio for three gear sizes.

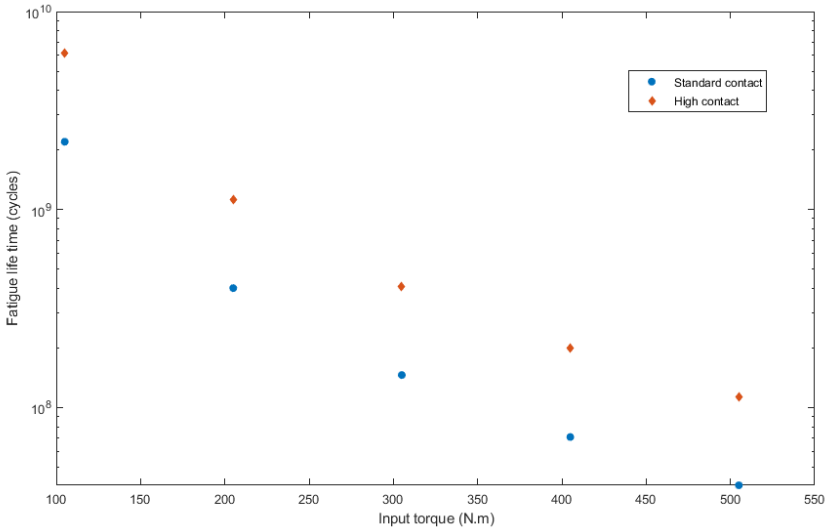

Figure 3-67 Comparison in fatigue life between standard contact and high contact ratio for the base diameter of 0.35 m.

Table 3-12 Input parameters for the case study

Parameter	Value	Meaning of the symbol	Unit
b	0.012	Width of the gear	m
t	0.012	The thickness of the tooth	m
L	0.025	Height of the tooth	m
S_{ut}	690	Ultimate strength	MPa
S'_e	280	Endurance limit	MPa
f	0.837	Correction factor	------
k_a	0.82	Surface factor	------
k_b	0.95	Size factor	------
k_c	1 for bending load	Load factor	------
k_d	1	Temperature factor	------
k_e	0.814 for 99% Reliability	Reliability factor	------
k_f	1	miscellaneous factor	------

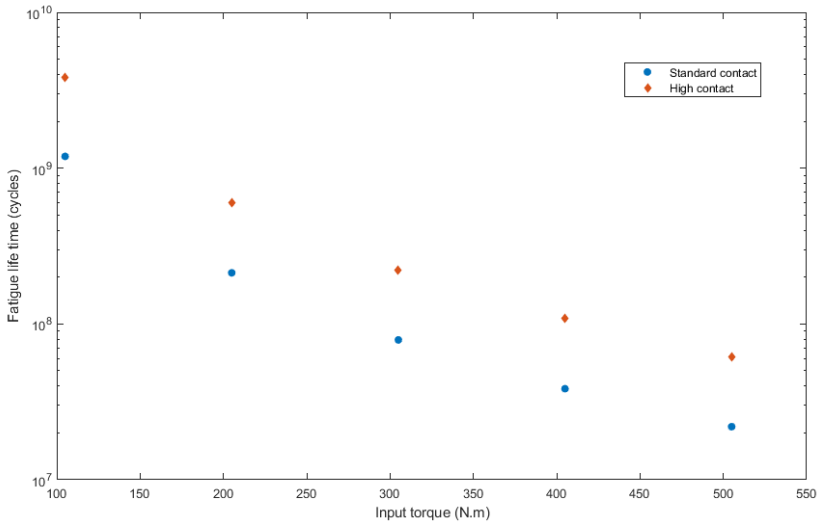

Figure 3-68 Comparison in fatigue life between standard contact and high contact ratio for the base diameter of 0.275 m.

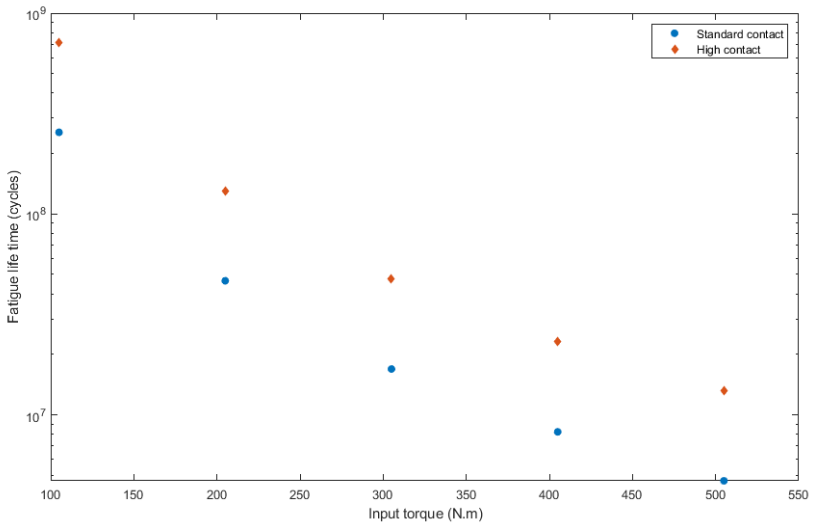

Figure 3-69 Comparison in fatigue life between standard contact and high contact ratio for base diameter 0.15 m.

The results show that the fatigue life for high contact ratio is longer than the fatigue life for standard contact for similar input torque and gear design. The reason for that is the high contact gears are sharing the load between two or three teeth but in standard contact, the load is shared between one and two teeth.

For the same input torque and same contact ratio, the gear with smaller base diameter has longer fatigue life. The normal force on the gear tooth is proportional to the gear diameter, so larger gears have shorter fatigue life.

4. CONCLUSION

4.1. Coupling

Windage in couplings plays a major role in a power loss of coupling and heating of guards. Utilizing CFD models can save money and time in addition to the reduction of human errors for the turbomachinery experiments. Many parameters can affect the power loss and heating of the guard. The proposed CFD model has been built to evaluate the effecting parameters on the windage power loss and guard heating. The results of the simulation show that rotating speed, clearance gap between the coupling and the guard, shaft temperature, ambient temperature, distance between flanges (DBFF), coupling diameter, number of bolts and oil to air ratio in the trapped air have an effect on the guard temperature and coupling power loss with different levels of effect.

The CFD model has been used to find solutions for guard heating. The first suggested solution was changing the shape of the guard like using mailbox guards instead of cylindrical guards. The second solution is adding some ventilation ports that allow for air circulation. Using a mailbox guard reduces the peak temperature of about 8%. The ventilation pipes design lowers the peak temperature of the guard by about 38%.

The effect of the emissivity of the guard material has been simulated by including the radiation heat transfer. Including the radiation heat transfer in the CFD simulation shows a minor effect on the peak temperature of the guard. The radiation has a small effect because the difference in temperature is small between the coupling and the guard and between the guard and the surrounding.

For the DOE, the selected parameters have been used to generate a prediction model for the diaphragm coupling power loss and guard peak temperature. Two prediction methods have been chosen.

The first one is the machine learning method. Gaussian Process (GP) with Matérn 5/2 covariance function has been used to generate the prediction model. The accuracy of this method depends on the DOE for the training dataset. For GP ML trained by the RSM training dataset, the accuracy was low where R^2 was 0.786 and 0.757 for the peak temperature and power loss prediction, respectively. Log transformation has been used to improve the accuracy of the GP ML trained by the RSM model. After using the transformed data to train the machine learning model, the values of R^2 were 0.887 and 0.903 for the peak temperature and power loss prediction, respectively.

Train the GP ML model by the FF DOE dataset achieved the best accuracy, where $R^2 = 0.96, R^2 = 0.98$ for power loss and peak temperature prediction respectively.

The second method of prediction was an empirical formula. Rayleigh's method has been used to generate the formula. The accuracy of the empirical formula was $R^2 = 0.907, R^2 = 0.843$ for power loss and peak temperature prediction, respectively.

4.2. Gears

A FEM was built to simulate the sliding power loss between the teeth of the gears. The model used the TEHL assumption to simulate the sliding power loss. Three types of simulations have been tested 1- 2D gear tooth model with TEHL solution 2- 3D gear tooth model with EHL solution 3- 3D gear tooth model with TEHL solution. These tests have

been done for standard contact ratio and high contact ratio gears. The results show that the 3D gear tooth model with the TEHL solution has the best accuracy comparing the experiments done by published work. The value of sliding power loss per tooth is higher in the standard contact than the high contact gears. On the other hand, the total power loss per cycle in the standard contact is very close to the total power loss in high contact gears for similar operating conditions.

The results of the sliding power loss used to simulate the thermal stress and thermal deformation in the tooth of the gear. PDE solver in MATLAB has been used to simulate the temperature distribution, thermal stress, and thermal deformation in the gear tooth. The thermal stress and thermal deformation is larger in the standard contact gears than the high contact gears

The results of the parametric study show that the standard contact and high contact system have similar behavior with the rotating speed of the gears and the load torque. For both systems, the sliding power loss is increasing with the increase in the rotating speed and the load torque.

A prediction model has been generated using a database simulated by the validated FEM. The prediction models were a machine learning model and an empirical formula. The accuracy of the machine learning model is better than the accuracy of the empirical formula. For machine learning model, a Log transformation has been used to improve the accuracy The value of R^2 was $R^2 = 0.98$ and $R^2 = 0.99$ for the empirical formula and machine leaning model respectively. The prediction models were validated with test cases inside of range and outside of the range. The accuracy of validation was similar for the

inside of range cases. For outside of range cases, the accuracy of the machine learning model was better than the empirical formula.

The type of lubrication was tested for different surface roughness. The case study has boundary lubrication with maximum power loss at average surface roughness $Ra = 5\ \mu m$. The mixed lubrication occurs at the cases that have $Ra = 1\ \mu m$ and $Ra = 0.6\ \mu m$. The last case has a value of $Ra = 0.1\ \ \mu m$. In this case, the lubrication was hydrodynamic for all the steps along the line of action. At the hydrodynamic lubrication, the sliding power loss was the minimum.

REFERENCES

[1] Mancuso, J. R., 1999, “Couplings and Joints: design, selection & application.” CRC Press, Florida, U.S.A, ISBN 9780824799502.

[2] Calistrat, M.M., 1976, “Metal Diaphragm Coupling Performance”, Proceedings of the 5th Turbomachinery Symposium, Texas A&M Univ., pp. 117-123.

[3] Farhadi, D., Tolou, N., and Herder, L., 2015, "A Review on Compliant Joints and Rigid-Body Constant Velocity Universal Joints toward the Design of Compliant Homokinetic Couplings.", ASME. J. Mech. Des., 137(3), pp. 032301.

[4] Sekhar, A.A. and Prabhu, B.S., 1995. Effects of coupling misalignment on vibrations of rotating machinery. Journal of Sound and vibration, 185(4), pp.655-671..

[5] Calistrat, M.M., 1985, “Design of Coupling Enclosures”, Proceedings of the 14th Turbomachinery Symposium, Texas A&M Univ., pp. 51-58.

[6] Thompson, A., Zhai, T., Palazzolo, A., and Keshmiri, A., 2016, “Coupling Guard Temperature and Windage Power Loss: CFD Analysis and Experiments”, Proceedings of the 14th Turbomachinery Symposium, Texas A&M Univ.

[7] API standard 671, 2007, “Special Purpose Coupling for Petroleum, Chemical, and Gas Industry Services” Fourth Edition, American Petroleum Institute, Washington D.C.

[8] Mills, A. F., 1999, “Basic Heat and Mass Transfer”, Pearson College Div., Upper Saddle River, NJ.

[9] Aydin, O., 2005, “Effects of viscous dissipation on the heat transfer in a forced pipe flow. Part 2: Thermally developing flow”, Energy Conversion and management, 46(18-19), pp. 3091-3102.

[10] Diab, Y., Ville, F., Changenet, C., and Velex, P. 2003, "Windage Losses in High Speed Gears: Preliminary Experimental and Theoretical Results." Proceedings of the ASME 2003 International Design Engineering Technical Conferences and Computers and Informati.

[11] Johnson, G., Simmons, K., and Foord, C., 2007, "Experimental Investigation Into Windage Power Loss From a Shrouded Spiral Bevel Gear.", Proceedings of the ASME Turbo Expo, Power for Land, Sea, and Air, Turbo Expo 2007, Parts A and B. Montreal, Canada, 6, .

[12] Calistrat, M.M., 1990, “Recent Case Histories with Coupling Enclosures”, Proceedings of the 19th Turbomachinery Symposium, Texas A&M Univ., pp. 37-42.

[13] Calistrat, M.M., 1990, “Recent Case Histories with Coupling Enclosures”, Proceedings of the 19th Turbomachinery Symposium, Texas A&M Univ., pp. 37-42.

[14] Carter, D., Martin, G., and Joseph, P., 1994, “The Baffling and Temperature Prediction of Coupling Enclosures”, Proceedings of the 23rd Turbomachinery Symposium, Texas A&M Univ., pp. 115-124.

[15] Calistrat, M.M., 1990, “Recent Case Histories with Coupling Enclosures”, Proceedings of the 19th Turbomachinery Symposium, Texas A&M Univ., pp. 37-42.

[16] Munson, R., Theodore, O., Wade, H., and Alric, R., 2013 “Fluid mechanics”. Singapore: Wiley, ISBN 1119080703.

[17] Seetharaman, S. and Kahraman, A., 2009. Load-independent spin power losses of a spur gear pair: model formulation. Journal of Tribology, 131(2), p.022201.

[18] Al-Shibl, K., Simmons, K. and Eastwick, C.N., 2007. Modelling windage power loss from an enclosed spur gear. Proceedings of the Institution of Mechanical Engineers, Part A: Journal of Power and Energy, 221(3), pp.331-341.

[19] Stone, R., 2012. Fatigue life estimates using goodman diagrams. Retrieved August, 17, p.2012.

[20] Marchesse, Y., Changenet, C., Ville, F. and Velex, P., 2011. Investigations on CFD simulations for predicting windage power losses in spur gears. Journal of Mechanical Design, 133(2)..

[21] Polly, J., Talbot, D., Kahraman, A., Singh, A. and Xu, H., 2018. An experimental investigation of churning power losses of a gearbox. Journal of Tribology, 140(3)..

[22] Ferreira, C., Bruns, E., Ferreira, S., Matos, D., David, M., Brandao, C., Da Silva, P., Portugal, L.A., Dos Reis, S., Souza, S. and Dos Santos, L., 2007. “Box-Behnken design: an alternative for the optimization of analytical methods”, Analytica chimica ac.

[23] Diab, Y., Ville, F. and Velex, P., 2006. Prediction of power losses due to tooth friction in gears. Tribology transactions, 49(2), pp.260-270.

[24] Wu, S. and Cheng, H.S., 1991. A friction model of partial-EHL contacts and its application to power loss in spur gears. Tribology Transactions, 34(3), pp.398-407.

[25] Anuradha, P. and Kumar, P., 2012. Effect of lubricant selection on EHL performance of involute spur gears. Tribology International, 50, pp.82-90.

[26] Jinzhan, G.J.F.Z.S. and Yunbo, S., 2010. Calculation of Meshing Efficiency for Spiral Bevel Gears under the Condition of Mixed Elastohydrodynamic Lubrication [J]. Transactions of the Chinese Society for Agricultural Machinery, 5.

[27] Heingartner, P. and Mba, D., 2008, June. Determining power losses in helical gear mesh: case study. In ASME 2003 international design engineering technical conferences and computers and information in engineering conference (pp. 965-970). American Society.

[28] Masjedi, M. and Khonsari, M.M., 2012. Film thickness and asperity load formulas for line-contact elastohydrodynamic lubrication with provision for surface roughness. Journal of Tribology, 134(1)..

[29] Masjedi, M. and Khonsari, M.M., 2012. Film thickness and asperity load formulas for line-contact elastohydrodynamic lubrication with provision for surface roughness. Journal of Tribology, 134(1)..

[30] Gan, L., Xiao, K., Wang, J., Pu, W. and Cao, W., 2019. A numerical method to investigate the temperature behavior of spiral bevel gears under mixed lubrication condition. Applied Thermal Engineering, 147, pp.866-875..

[31] Ziegltrum, A., Lohner, T. and Stahl, K., 2017. TEHL simulation on the influence of lubricants on load-dependent gear losses. Tribology International, 113, pp.252-261..

[32] Lu, H., Berzins, M., Goodyer, C.E. and Jimack, P.K., 2005. High-order discontinuous Galerkin method for elastohydrodynamic lubrication line contact problems. Communications in numerical methods in engineering, 21(11), pp.643-650..

[33] Heingartner, P. and Mba, D., 2003, January. Determining power losses in helical gear mesh: case study. In International Design Engineering Technical Conferences and Computers and Information in Engineering Conference (Vol. 37025, pp. 965-970)..

[34] Magyar, Balázs, and Bernd Sauer. "Calculation of the efficiency of worm gear drives." (2015).

[35] Wang, J. and Howard, I., 2005. Finite element analysis of high contact ratio spur gears in mesh. J. Trib., 127(3), pp.469-483.

[36] Chang, J., Liu, S., Hu, X. and Dai, Y., 2019. Evolution of surface spur gear tooth temperature based on three-dimensional finite element model. Journal of the Brazilian Society of Mechanical Sciences and Engineering, 41(9), p.370.

[37] Fernandes, C.M., Rocha, D.M., Martins, R.C., Magalhães, L. and Seabra, J.H., 2018. Finite element method model to predict bulk and flash temperatures on polymer gears. Tribology International, 120, pp.255-268.

[38] Shi, Y., Yao, Y.P. and Fei, J.Y., 2016. Analysis of bulk temperature field and flash temperature for locomotive traction gear. Applied Thermal Engineering, 99, pp.528-536.

[39] Liu, Y., Liu, Q. and Dong, P., 2017, November. Effect of Design Parameters on Lubrication Behavior of Spur Gear Pairs. In ASME 2017 International Mechanical Engineering Congress and Exposition (pp. V009T12A020-V009T12A020). American Society of Mechanical .

[40] Liu, H., Zhu, C., Sun, Z., Zhang, Y. and Song, C., 2016. Coefficient of friction of a starved lubricated spur gear pair. Journal of Mechanical Science and Technology, 30(5), pp.2171-2177.

[41] Prabhu Sekar, R., Geo, V.E. and Jesu Martin, L., 2017. A mixed finite element and analytical method to predict load, mechanical power loss and improved efficiency in non-standard spur gear drives. Proceedings of the Institution of Mechanical Engineers, Pa.

[42] Lohner, T., Ziegltrum, A., Stemplinger, J.P. and Stahl, K., 2016. Engineering software solution for thermal elastohydrodynamic lubrication using multiphysics software. Advances in Tribology, 2016.

[43] Akbarzadeh, S. and Khonsari, M.M., 2008. Thermoelastohydrodynamic analysis of spur gears with consideration of surface roughness. Tribology Letters, 32(2), pp.129-141.

[44] Wang, Y., Li, H., Tong, J. and Yang, P., 2004. Transient thermoelastohydrodynamic lubrication analysis of an involute spur gear. Tribology International, 37(10), pp.773-782.

[45] Bobach, L., Beilicke, R., Bartel, D. and Deters, L., 2012. Thermal elastohydrodynamic simulation of involute spur gears incorporating mixed friction. Tribology International, 48, pp.191-206.

[46] Liu, H., Zhu, C., Sun, Z. and Song, C., 2016. Starved lubrication of a spur gear pair. Tribology International, 94, pp.52-60.

[47] Li, S. and Kahraman, A., 2010. A transient mixed elastohydrodynamic lubrication model for spur gear pairs. Journal of Tribology, 132(1), p.011501.

[48] Li, S. and Kahraman, A., 2010. Prediction of spur gear mechanical power losses using a transient elastohydrodynamic lubrication model. Tribology Transactions, 53(4), pp.554-563.

[49] Jie, L., Lei, Z. and Qi, Z., 2010, January. Comparison and analysis on different finite element models of gear interfacial contact temperature. In 2010 Second international conference on computer modeling and simulation (Vol. 3, pp. 132-136). IEEE.

[50] Jie, P., Shaojun, L. and Xiaozhou, H., 2013, January. The bulk temperature analysis of the involute spur gear based on parameterized modeling of APDL. In 2013 Fifth International Conference on Measuring Technology and Mechatronics Automation (pp. 1146-114.

[51] Xing, C. and Shaojun, L., 2013, June. Analysis of bulk temperature in high-speed gears based on finite element method. In 2013 Fourth international conference on digital manufacturing & automation (pp. 202-206). IEEE.

[52] Li, W. and Tian, J., 2017. Unsteady-state temperature field and sensitivity analysis of gear transmission. Tribology International, 116, pp.229-243.

[53] Anuradha, P. and Kumar, P., 2012. Effect of lubricant selection on EHL performance of involute spur gears. Tribology International, 50, pp.82-90.

[54] Li, S., 2015. A thermal tribo-dynamic mechanical power loss model for spur gear pairs. Tribology International, 88, pp.170-178.

[55] Zhang, J.G., Liu, S.J. and Fang, T., 2017. On the prediction of friction coefficient and wear in spiral bevel gears with mixed TEHL. Tribology International, 115, pp.535-545.

[56] Mongkol, M. and Jesda, P., 2012. TEHL Analysis of Rough Surface Spur Gears with Non-Newtonian Lubricants under Sudden Overloads. Journal of Advanced Mechanical Design, Systems, and Manufacturing, 6(7), pp.1031-1045.

[57] Luo, B. and Li, W., 2017. Influence factors on bulk temperature field of gear. Proceedings of the Institution of Mechanical Engineers, Part J: Journal of Engineering Tribology, 231(8), pp.953-964.

[58] Patil, S.S., Karuppanan, S., Atanasovska, I. and Wahab, A.A., 2014. Contact stress analysis of helical gear pairs, including frictional coefficients. International Journal of Mechanical Sciences, 85, pp.205-211.

[59] Budzik, G., Kozik, B. and Pacana, J., 2013. Defining influence of load conditions on distribution and value of stresses in dual-power-path gear wheels applying FEM. Aircraft Engineering and Aerospace Technology, 85(6), pp.453-459.

[60] Wang, P.Y., Fan, S.C. and Huang, Z.G., 2011. Spiral bevel gear dynamic contact and tooth impact analysis. Journal of Mechanical Design, 133(8), p.084501.

[61] Gupta, B., Choubey, M.A. and Varde, M.G.V., 2012. Contact stress analysis of spur gear. International Journal of Engineering Research and Technology, 1(4), pp.1-7.

[62] Ooi, J., Wang, X., Tan, C., Ho, J.H. and Lim, Y.P., 2012. Modal and stress analysis of gear train design in portal axle using finite element modeling and simulation. Journal of Mechanical Science and Technology, 26(2), pp.575-589.

[63] Karaveer, V., Mogrekar, A. and Joseph, T.P.R., 2013. Modeling and finite element analysis of spur gear. International Journal of Current Engineering and Technology, 3(5), pp.2104-2107.

[64] Thirumurugan, R. and Muthuveerappan, G., 2013, December. Study on mesh power losses in high contact ratio (HCR) gear drives. In Proceedings of the 1st international conference on machines and mechanisms (iNaCoMM2013) (pp. 169-176).

[65] Karpat, F. and Ekwaro-Osire, S., 2010, January. Efficiency of the High Contact Ratio Involute Spur Gears With Asymmetric Teeth. In ASME 2010 International Mechanical Engineering Congress and Exposition (pp. 319-327). American Society of Mechanical Enginee.

[66] Mortazavi, F., and Palazzolo, A., 2018,"Prediction of Rotordynamic Performance of Smooth Stator-Grooved Rotor Liquid Annular Seals Utilizing Computational Fluid Dynamics." ASME. J. Vib. Acoust., 140(3), pp. 031002-031002-031009.

[67] Hill, J., Kunz, F., Medvitz, B., Handschuh, F., Long, N., Noack, W., and Morris, J., 2011 "CFD Analysis of Gear Windage Losses: Validation and Parametric Aerodynamic Studies." ASME. J. Fluids Eng. 133(3), pp.031103.

[68] Lawson, J., Li, Y., and Sale, C. ", 2011, “Development and Verification of a Computational Fluid Dynamics Model of a Horizontal-Axis Tidal Current Turbine." Proceedings of the ASME 2011 30th International Conference on Ocean, Offshore and Arctic Engineeri.

[69] Calistrat, M.M., 1993, “Hydraulic Removal of Coupling Hubs-Keyed and Keyless”, Proceedings of the 22nd Turbomachinery Symposium, Texas A&M Univ., pp. 153-160.

[70] Choy, C., 2015, “Effective medium theory: principles and applications”, Oxford University Press, UK, ISBN 0198518927.

[71] Rapley, S., Eastwick, C., and Simmons, K., 2007, "The Application of CFD to Model Windage Power Loss From a Spiral Bevel Gear.", Proceedings of the ASME Turbo Expo, Power for Land, Sea, and Air, Parts A and B. Montreal, Canada, 6, pp. 47-56.

[72] Ferreira, C., Bruns, E., Ferreira, S., Matos, D., David, M., Brandao, C., Da Silva, P., Portugal, L.A., Dos Reis, S., Souza, S. and Dos Santos, L., 2007. “Box-Behnken design: an alternative for the optimization of analytical methods”, Analytica chimica ac.

[73] Veronica C., 1999, “One-Factor-at-a-Time versus Designed Experiments”, The American Statistician, 53(2), pp. 126-131.

[74] Mendoza, C., 1994, "A theorem for Rayleigh's method of dimensional analysis and its proof." Mechanics research communications 21(2), pp. 103-107.

[75] Rasmussen, E., 2003, "Gaussian processes in machine learning." In Summer School on Machine Learning, Springer, Berlin, Heidelberg, pp. 63-71.

[76] Guttorp, P. and Gneiting, T., 2006. “Studies in the history of probability and statistics XLIX on the Matern correlation family”. Biometrika, 93(4), pp.989-995.

[77] Pacheco, E., Amon, H., and Finger, S., 2004, "Bayesian Surrogates Applied to Conceptual Stages of the Engineering Design Process" ASME. J. Mech. Des., 125(4), pp. 664–672.

[78] Manikandan, S., 2010. Preparing to analyse data. Journal of pharmacology & pharmacotherapeutics, 1(1), p.64.

[79] Bland, J.M. and Altman, D.G., 1996. Transformations, means, and confidence intervals. BMJ: British Medical Journal, 312(7038), p.1079.

[80] Manikandan, S., 2010. Data transformation. Journal of Pharmacology and Pharmacotherapeutics, 1(2), p.126.

[81] Bland, J.M. and Altman, D.G., 1996. Statistics notes: Transforming data. Bmj, 312(7033), p.770.

[82] Maier, E., Ziegltrum, A., Lohner, T. and Stahl, K., 2017. Characterization of TEHL contacts of thermoplastic gears. Forschung im Ingenieurwesen, 81(2-3), pp.317-324..

[83] Sánchez, M.B., Pleguezuelos, M. and Pedrero, J.I., 2017. Approximate equations for the meshing stiffness and the load sharing ratio of spur gears including hertzian effects. Mechanism and Machine Theory, 109, pp.231-249..

[84] Wang, J. and Howard, I., 2005. Finite element analysis of high contact ratio spur gears in mesh. J. Trib., 127(3), pp.469-483..

[85] He, Song, Rajendra Gunda, and Rajendra Singh. "Inclusion of sliding friction in contact dynamics model for helical gears." (2007): 48-57..

[86] L. I. U. Qiang, "Friction in mixed and elastohydrodynamic lubricated contacts including thermal.

[87] Heinrich, J., et al., 1977, "An 'Upwind' Finite Element Scheme for Two-dimensional Convective Transport Equation," International Journal for Numerical Methods in Engineering, 11(1): p. 131-143.

[88] Simon, V. (January 1, 1981). "Elastohydrodynamic Lubrication of Hypoid Gears." ASME. J. Mech. Des. January 1981; 103(1): 195–203.

[89] Atkin, R.J. and Fox, N., 2005. An introduction to the theory of elasticity. Courier Corporation.

[90] Nollert, M.U., Diamond, S.L. and McIntire, L.V., 1991. Hydrodynamic shear stress and mass transport modulation of endothelial cell metabolism. Biotechnology and bioengineering, 38(6), pp.588-602..

[91] Forsman, H., Andersson, P. and Bäckström, G., 1982. Thermal conductivity and heat capacity of n-heptane, n-and iso-propyl-alcohol at high pressure. Physica B+ C, 114(3), pp.287-294.

[92] Tuomas, R. and Isaksson, O., 2006. Compressibility of oil/refrigerant lubricants in elasto-hydrodynamic contacts. Journal of tribology, 128(1), pp.218-220.

[93] Bair, S. and Casalini, R., 2008. A scaling parameter and function for the accurate correlation of viscosity with temperature and pressure across eight orders of magnitude of viscosity. Journal of Tribology, 130(4), p.041802.

[94] Colynuck, A.J. and Medley, J.B., 1989. Comparison of two finite difference methods for the numerical analysis of thermohydrodynamic lubrication. Tribology Transactions, 32(3), pp.346-356..

[95] Fernandes, C.M., Rocha, D.M., Martins, R.C., Magalhães, L. and Seabra, J.H., 2018. Finite element method model to predict bulk and flash temperatures on polymer gears. Tribology International, 120, pp.255-268..

[96] Roda-Casanova, V. and Sanchez-Marin, F., 2019. A 2D finite element based approach to predict the temperature field in polymer spur gear transmissions. Mechanism and Machine Theory, 133, pp.195-210.

[97] Ju, T., Schaefer, S. and Warren, J., 2005. Mean value coordinates for closed triangular meshes. ACM Transactions on Graphics (TOG), 24(3), pp.561-566.

[98] Kang, S.S. and Cho, S.K., 2012. Thermal deformation and stress analysis of disk brakes by finite element method. Journal of Mechanical Science and Technology, 26(7), pp.2133-2137..

[99] Pleguezuelos, M., Pedrero, J.I. and Sánchez, M.B., 2013. Analytical expressions of the efficiency of standard and high contact ratio involute spur gears. Mathematical Problems in Engineering, 2013..

[100] Pennestri`, E., and Freudenstein, F. (September 1, 1993). "A Systematic Approach to Power-Flow and Static-Force Analysis in Epicyclic Spur-Gear Trains." ASME. J. Mech. Des. September 1993; 115(3): 639–644.

[101] Chang, J., Liu, S., Hu, X. and Dai, Y., 2019. Evolution of surface spur gear tooth temperature based on three-dimensional finite element model. Journal of the Brazilian Society of Mechanical Sciences and Engineering, 41(9), p.370.

[102] Nakahara, T. and Tanaka, T., 2013. A Stochastic Analysis of Plastic Area on Rough Surface Contact in Relation with Transition from Mild to Severe Wear. Tribology Online, 8(1), pp.128-134..

[103] Jin, Z. and Fisher, J., 2014. Tribology in joint replacement. In Joint replacement technology (pp. 31-61). Woodhead Publishing.

[104] Fu, Y.F., Gong, J., Li, P.W. and Yang, Z.M., 2017. Fatigue life assessment of screw blades in screw sand washing machine under extreme load. American Journal of Mechanical Engineering, 5(1), pp.1-7..

[105] Gouda, E., Mezani, S., Baghli, L. and Rezzoug, A., 2010. Comparative study between mechanical and magnetic planetary gears. IEEE Transactions on Magnetics, 47(2), pp.439-450.

[106] Budynas, R.G. and Nisbett, J.K., 2020. Shigley's mechanical engineering design. McGraw-Hill Education..

APPENDIX A

SOLVING REYNOLDS EQUATION USING FINITE ELEMENT METHOD

The purpose of this section is to support the reader with more details about the solution of the Reynolds equation using the finite element technique.

The general form of the Reynolds equation for lubricant is Eq. A-1.

$$\nabla \cdot (D_1 \nabla P) + \nabla D_2 \cdot (U_2 - U_1) + (\nabla h) \cdot U_1 + \partial h / \partial t = 0 \qquad \textbf{Eq. A-1}$$

This domain has boundary conditions. The boundary condition is the prescribed pressure at the boundary as shown in Figure A-1. The figure shows that each node in the boundary has a specific value of pressure. The value of the prescribed pressure is shown in Eq. A-2.

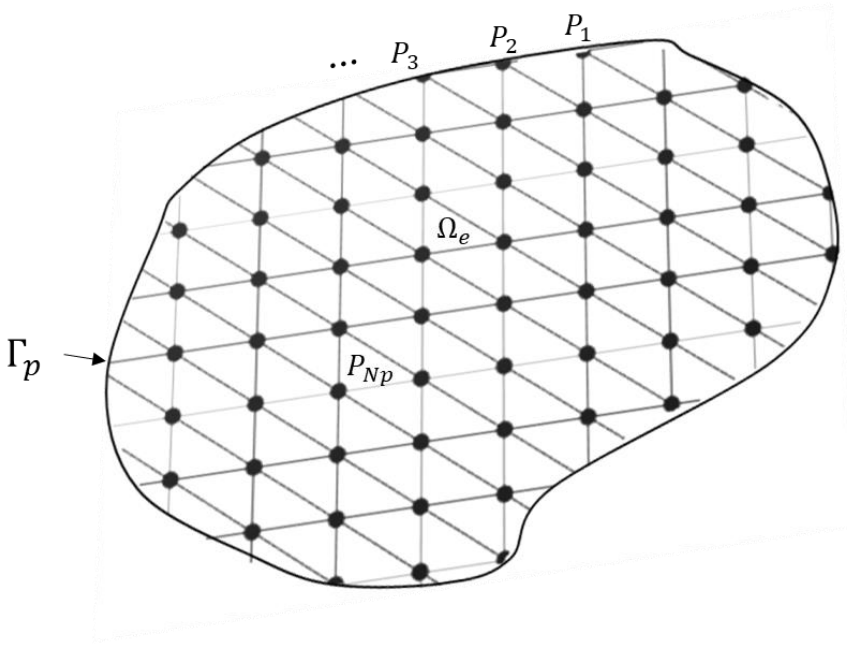

Figure A-1 FEM for the lubricating domain

$$P = P^{*} on \Gamma_p$$ **Eq. A-2**

The variational principle has been used to solve the Reynolds equation with variable viscosity. The solution will be found by making the function Eq. A-3 stationary. The stationary point could be found by finding the value of function P that achieves the minimum value of the Eq. A-3.

$$I_e = \int_\Omega \left[-\frac{1}{2} D_1 \nabla P \cdot \nabla P + D_2 U \cdot \nabla P + P \frac{\partial h}{\partial t} \right] d\Omega + \int_{\Gamma_q} Pq \cdot n d\Gamma$$ **Eq. A-3**

The stationary point will be found by taking the first derivative of the equation with respect to the pressure and make it equal zero as described in Eq. A-4.

$$\frac{\partial I_e}{\partial P_{ie}} = 0$$ **Eq. A-4**

Galerkin method has been used to evaluate the approximate function of pressure. Figure xx shows the element with the pressure at each node. The methodology of calculating the average pressure on the element is explained in Figure A-2 and Eq. A-5.

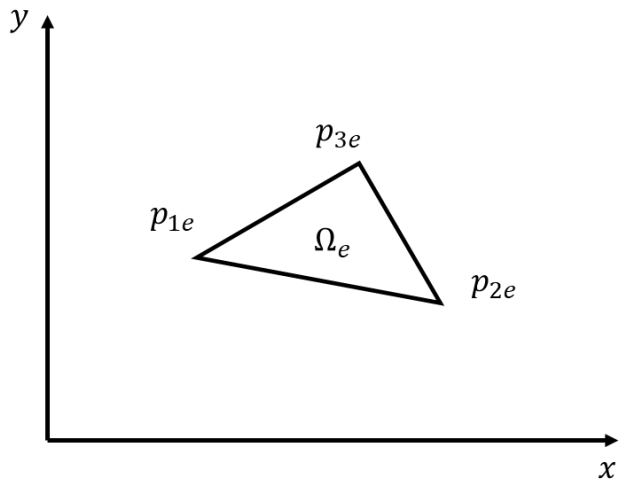

Figure A-2 Simplex element with three nodes for pressure interpolation

$$P_{ap} = N \cdot P$$ **Eq. A-5**

Where the vector P is the pressure at each node. The vector N is the shape function. The final form of this finite element matrix can be written as shown in Eq. A-6. Where K_f is the stiffness matrix, F_f is the force vector.

$$[K_f]\{P\} = \{F_f\}$$ **Eq. A-6**

The force vector has three effects. These effects are wedge effect, squeeze effect, and impose the boundary flow effect. The wedge effect is presented by vector B. The squeeze effect is given by vector S. the Vector L represents the impose boundary flow. The equations for each term are described in the below equations.

$$[K_f] = -\int_\Omega D_1 \left(\frac{\partial N_i}{\partial x}\frac{\partial N_j}{\partial x} + \frac{\partial N_i}{\partial y}\frac{\partial N_j}{\partial y}\right) d\Omega$$ **Eq. A-7**

$$\{B\} = \int_\Omega D_2 U_x \frac{\partial N_i}{\partial x} d\Omega + \int_\Omega D_2 U_x \frac{\partial N_i}{\partial y} d\Omega$$ **Eq. A-8**

$$\{S\} = -\frac{\partial h}{\partial t}\int_\Omega N_i d\Omega$$ **Eq. A-9**

$$\{L\} = -\int_{\Gamma_q} q N_i d\Gamma$$ **Eq. A-10**

The lubrication domain was divided into elements. To solve the finite element model, the above equations should be applied on each element. The total domain of the lubricant will be $\sum_{i=1}^{n_e} \Omega_e(i)$, where n_e is the total number of elements. The final form for the stiffness matrix and the force vector for the total domain are shown in Eq. A-11 and Eq. A-12 respectively.

$$[K_f] = \sum_{i=1}^{n_e} [K_f^e] \quad \textbf{Eq. A-11}$$

$$\{F_f\} = \sum_{i=1}^{n_e} \{F_f^e\} \quad \textbf{Eq. A-12}$$

Figure A-3 shows a simplex triangular element. The element has linear shape functions between the nodes.

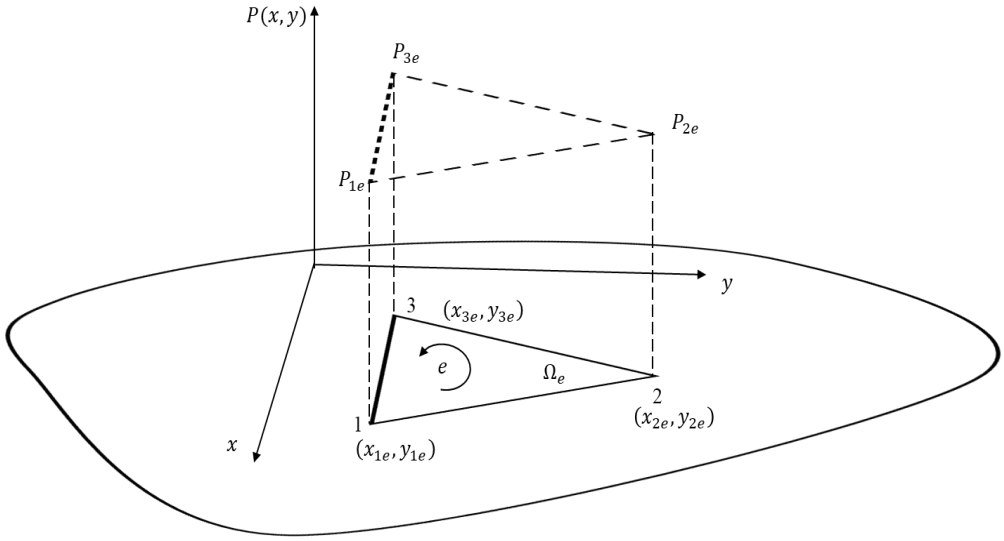

Figure A-3 Linear interpolation for the pressure in a three nodes simplex element

The shape functions for the simplex triangular element could be evaluated using Eq. A-13. A^e represents the area of the element.

$$N_i = \left(\frac{1}{2A^e}\right)(a_i^e + b_i^e + c_i^e), i = 1,2,3 \quad \textbf{Eq. A-13}$$

The area of the element could be evaluated by Eq. A-14.

$$A^e = \frac{1}{2}[(x_2y_3 - x_3y_2) - (x_1y_3 - x_3y_1) + (x_1y_2 - x_2y_1)] \quad \textbf{Eq. A-14}$$

The coefficients of the shape functions are described below.

$$\begin{bmatrix} a_1 & a_2 & a_3 \\ b_1 & b_2 & b_3 \\ c_1 & c_2 & c_3 \end{bmatrix} = \begin{bmatrix} x_2y_3 - x_3y_2 & x_1y_3 - x_3y_1 & x_1y_2 - x_2y_1 \\ y_2 - y_3 & y_3 - y_1 & y_1 - y_2 \\ x_3 - x_2 & x_1 - x_3 & x_2 - x_1 \end{bmatrix} \quad \textbf{Eq. A-15}$$

The line integrals for the shape functions cloud be calculated using the following equations.

$$\int_{A^e} N_1^{\alpha} N_2^{\beta} N_3^{\gamma} dA = 2A^e \frac{\alpha!\beta!\gamma!}{(\alpha+\beta+\gamma+2)!} \quad \textbf{Eq. A-16}$$

$$\int_{side1-2} N_1^{\alpha} N_2^{\beta} dL = L_{1-2} \frac{\alpha!\beta!}{(\alpha+\beta+1)!} \quad \textbf{Eq. A-17}$$

$$\int_{side1-2} N_3^{\gamma} dL = 0 \quad \textbf{Eq. A-18}$$

where L is the distance between any two nodes. The subscript 1-2 means that this distance is between node number 1 and node number 2.

By substituting the values of the shape functions in Eq. A-7-Eq. A-10 will release Eq. A-19 - Eq. A-23. To get the averaged value, the equations were integrated over the domain of the element and then divided by the area of the element.

$$[\mathrm{K_f}] = -\int_{\Omega} \mathrm{D_1} \left(\frac{\partial \mathrm{N_i}}{\partial \mathrm{x}} \frac{\partial \mathrm{N_j}}{\partial \mathrm{x}} + \frac{\partial \mathrm{N_i}}{\partial \mathrm{y}} \frac{\partial \mathrm{N_j}}{\partial \mathrm{y}} \right) \mathrm{d}\Omega = -\left(\mathrm{b_i b_j} + \mathrm{c_i c_j} \right) \frac{\bar{\mathrm{C}}_1}{4\mathrm{A^e}} \quad \textbf{Eq. A-19}$$

$$\{\mathrm{B}\} = \int_{\Omega} \mathrm{D_2 U_x} \frac{\partial \mathrm{N_i}}{\partial \mathrm{x}} \mathrm{d}\Omega + \int_{\Omega} \mathrm{D_2 U_x} \frac{\partial \mathrm{N_i}}{\partial \mathrm{y}} \mathrm{d}\Omega = \left(\mathrm{U_x b_i} + \mathrm{U_y c_i} \right) \frac{\bar{\mathrm{C}}_2}{2} \quad \textbf{Eq. A-20}$$

$$\{\mathrm{S}\} = -\frac{\partial \mathrm{h}}{\partial \mathrm{t}} \int_{\Omega} \mathrm{N_i d}\Omega = -\frac{\rho \mathrm{A^e}}{3} \frac{\partial \mathrm{h}}{\partial \mathrm{t}} \quad \textbf{Eq. A-21}$$

$$\{\mathrm{L}\} = -\int_{\Gamma_q} \mathrm{q N_i d}\Gamma = -\mathrm{q} \frac{\mathrm{L_{i-j}}}{2} \quad \textbf{Eq. A-22}$$

$$\bar{\mathrm{C}}_i = \frac{1}{\mathrm{A^e}} \int_{\Omega} \mathrm{D_1 d}\Omega_e \quad \textbf{Eq. A-23}$$